University of Alabama in Huntsville

LOUIS

2018

Computational investigations of ignition characteristics of live fuels and deposition of firebrands in a turbulent boundary layer

Chandana Anand

COMPUTATIONAL INVESTIGATIONS OF IGNITION CHARACTERISTICS OF LIVE FUELS AND DEPOSITION OF FIREBRANDS IN A TURBULENT BOUNDARY LAYER

by

CHANDANA ANAND

A DISSERTATION

Submitted in partial fulfillment of the requirements
for the degree of Doctor of Philosophy
in
The Department of Mechanical and Aerospace Engineering
to
The School of Graduate Studies
of
The University of Alabama in Huntsville

HUNTSVILLE, ALABAMA

2018

In presenting this dissertation in partial fulfillment of the requirements for a doctoral degree from The University of Alabama in Huntsville, I agree that the Library of this University shall make it freely available for inspection. I further agree that permission for extensive copying for scholarly purposes may be granted by my advisor or, in his/her absence, by the Chair of the Department or the Dean of the School of Graduate Studies. It is also understood that due recognition shall be given to me and to The University of Alabama in Huntsville in any scholarly use which may be made of any material in this dissertation.

_____   11/5/2018
Chandana Anand   (date)

DISSERTATION APPROVAL FORM

Submitted by Chandana Anand in partial fulfillment of the requirements for the degree of Doctor of Philosophy in Mechanical Engineering and accepted on behalf of the Faculty of the School of Graduate Studies by the dissertation committee.

We, the undersigned members of the Graduate Faculty of The University of Alabama in Huntsville, certify that we have advised and/or supervised the candidate of the work described in this dissertation. We further certify that we have reviewed the dissertation manuscript and approve it in partial fulfillment of the requirements for the degree of Doctor of Philosophy in Mechanical Engineering.

Dr. Babak Shotorban	11,6,18 (Date)	Committee Chair
Dr. Shankar Mahalingam	11/06/18 (Date)	
Dr. Kader Frendi	11/06/18 (Date)	
Dr. Sarma Rani	11/6/2018 (Date)	
Dr. Chang-Kuen Kang	11/6/2018 (Date)	
Dr. Keith Hollingsworth	11/6/18 (Date)	Department Chair
Dr. Shankar Mahalingam	11/06/18 (Date)	College Dean
Dr. David Berkowitz	11/8/18 (Date)	Graduate Dean
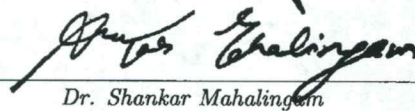
iii

ABSTRACT

School of Graduate Studies
The University of Alabama in Huntsville

Degree   Doctor of Philosophy   College/Dept.   Engineering/Mechanical and

Aerospace Engineering
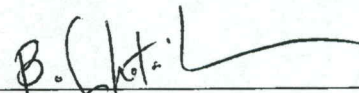
Name of Candidate   Chandana Anand

Title   Computational investigations of ignition characteristics of live fuels

and deposition of firebrands in a turbulent boundary layer

In the current study, computational investigation of live fuels and the propagation of firebrands in a turbulent flow field was investigated as relevant to the spotting mechanism occurring in wildfires. Spotting, which is the creation of a secondary (spot) fire by flying firebrands (also referred to as embers) that originate from a primary fire, is a common mechanism for the spread of wildland and wildland-urban interface (WUI) fires. To improve the understanding of the ignitability condition of recipient fuels as relevant to the landing stage in the spotting mechanism, computational investigation of ignition of live fuels by piloted ignition was performed. The live fuel ignition study was mainly guided by the experiments of McAllister *et al.*, *Fire Safety Journal*, **51**, 133-142 (2012). Live fuels exhibit different rates of moisture evaporation due to the distinct states in which water is stored: free and bound states. Free water in live fuels exists within the cell cavities, whereas bound water exists within the cell walls. In the current work, the conventional moisture evaporation model for live fuels was improved by including the effects of both free and bound water to study the ignition characteristics of live fuels. The simulated and the experimental ignition times compared reasonably well with each other. The time evolution

iv

of simulated and experimental mass loss rates also compared well with each other. For all fuel moisture contents, it was observed that the release of bound moisture starts at temperatures greater than 200°C long after ignition time. This observation was consistent with the release of moisture observed at high temperatures in the experiments of live fuels. Next, the explicit role of turbulence in the propagation and deposition of firebrands for the intermediate spotting range was studied. Here, the dispersion and deposition of cylindrical shaped firebrands in a turbulent boundary layer was investigated by large eddy simulation of air flow, with firebrands individually tracked in a Lagrangian framework. The carried firebrands experienced both translation and rotation as gravity, drag and lift forces acted on them. Simulations were carried out in a turbulent boundary layer with a free stream wind velocity of 18.8 m/s, an initial boundary layer height of 25 m, with firebrand densities of 70, 230, and 570 kg/m^3 and release heights of 20 m and 40 m. Two distinct sets of simulations were performed by considering non-burning and burning firebrands. Identical firebrands were consecutively released under identical initial conditions after the turbulent flow reached a statistically stationary state. The motion and deposition location of firebrands were determined by tracking tens of thousands of firebrands in each simulation and computing statistical quantities such as dispersion and diffusion of flying firebrands, and the joint probability density function of the coordinates of the deposited firebrands. For all the cases, the distribution of deposited firebrands exhibited symmetry in the spanwise direction. The normalized mean position of the deposited firebrands with constant mass in the streamwise direction increased approximately by a factor of two when the density of firebrands decreased from 570 kg/m^3 to 70 kg/m^3. Also, the

ground distribution of firebrands that were released from a higher elevation was found more leptokurtic with the calculated multivariate kurtosis deviating more than 5% of that of a normal distribution. For the cases with burning firebrands, simulations were performed for initial firebrand densities of 230 and 570 kg/m^3. As compared to the non-burning firebrands, since the burning firebrands experience mass reduction, they travelled for a longer distance (approximately 10 m ahead) in the streamwise direction as compared to the non-burning firebrands. The temperature of the firebrands were controlled by convective and radiative modes of cooling with convection being the dominant mechanism. To gain an insight into the areas prone to the occurrence of spot fires, the ground deposition pattern of the landed firebrands was also studied. Here, the mass and energy per unit area of the landed firebrands was quantified and the average temperature of the landed firebrands was predicted. It was found that firebrands with a higher initial density of 570 kg/m^3 retained more energy (with average temperatures of 450 K) at the time of deposition. This behavior indicated a greater chance of occurrence of spot fires with higher density firebrands as they are less likely to cool and reach ambient temperatures at the time of deposition.

Abstract Approval: Committee Chair _____
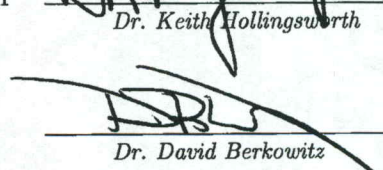   Dr. Babak Shotorban

                    Department Chair _____ 11-6-19
                                     Dr. Keith Hollingsworth

                    Graduate Dean   _____ 11/8/19
                                     Dr. David Berkowitz

ACKNOWLEDGMENTS

Chandana Anand

TABLE OF CONTENTS

xiv

LIST OF TABLES

LIST OF SYMBOLS AND ABBREVIATIONS

x, y, z	co-ordinates in the inertial reference frame
x_r, y_r, z_r	co-ordinates in the rotational reference frame
$\vec{x}_\mathrm{p}$	firebrand position vector
$\vec{V}_\mathrm{p}$	firebrand velocity vector
t	time
m_p	mass of firebrand
$\vec{F}_G$	gravitational force on firebrand
$\vec{F}_D$	drag force on firebrand
$\vec{F}_L$	lift force on firebrand
ρ_p	density of firebrand
ρ_gas	density of air
V_p	volume of firebrand
$\vec{g}$	gravity vector
a	radius of firebrand
b	length of firebrand
Re_b	Reynolds number based on firebrand length

C_D	drag co-efficient of firebrand
V_{rel}	velocity of firebrand relative to background air velocity
α	incidence angle measured between firebrand major axis and relative velocity
$\vec{U}, \vec{V}, \vec{W}$	velocity of the carrying fluid
Re_α	Reynolds number based on firebrand incidence angle
I	moment of inertia of firebrand
$\vec{\omega}$	angular velocity of firebrand
$\vec{T}_{\text{resis}}$	resistive torque on firebrand
$\vec{T}_{\text{hydro}}$	hydrodynamic torque on firebrand
x_{cp}	distance between centre of pressure and centre of mass of firebrand
A	transformation matrix
$\epsilon_1, \epsilon_2, \epsilon_3, \eta$	quaternions
μ	viscosity of air
Δh_{vap}	enthalpy of moisture evaporation
Δh_{pyr}	enthalpy of volatilization
Δh_{char}	enthalpy of char oxidation
$\mathbf{q}_{\text{c}}$	convective heat loss
h_{conv}	convective heat transfer coefficient

$\mathbf{q_r}$ radiative heat loss

σ Stefan-Boltzmann constant

ϵ emissivity

A_p surface area of the firebrand

Nu Nusselt number

Pr Prandtl number

E_i activation energy of species i

A_i pre-exponential factor of species i

R universal gas constant

T temperature

α_k ratio between discrete integration steps

h_k integration step at $\mathrm{k^{th}}$ level

U_i mean velocity component of background air

u_i'' fluctuating velocity component of background air

W weighting function

η normalized outer co-ordinate of the turbulent boundary layer

δ^* normalized inner co-ordinate of the turbulent boundary layer

D^* characteristic flame diameter

u_τ friction velocity

τ_w	wall shear stress
Re_θ	Reynolds number based on momentum thickness of the boundary layer
u^+	velocity normalized by friction velocity
$\langle\,\rangle$	average based on firebrand ensemble
$\langle x'_{\mathrm{p},i}(t)x'_{\mathrm{p},j}(t)\rangle$	dispersion tensor of firebrands
D_{ij}	diffusivity tensor of firebrands
$f(x,y)$	probability density function of the landing coordinates of released firebrands
$K(x,y)$	smoothing kernel
h	bandwidth parameter
R_{char}	charring rate
Y_{O_2}	mass fraction of oxygen
D_{O_2}	diffusion co-efficient of oxygen
$\rho_{\mathrm{p},0}$	initial density of firebrand
D_0	initial diameter of firebrand
$m_{\mathrm{p,ground}}$	mass per unit surface area
$e_{\mathrm{p,ground}}$	energy per unit surface area
$T_{\mathrm{p,ground}}$	average temperature of landed firebrands
WUI	wildland-urban interface

FMC	fuel moisture content
FIST	forced ignition and flame spread test
RANS	Reynolds averaged Navier-Stokes
LES	large-eddy simulation
CFD	computational fluid dynamics
TBL	turbulent boundary layer
WFDS	wildland-urban interface fire dynamics simulator
SGS	subgrid-scale
RK	Runge-Kutta scheme
AB	Adams Bashforth scheme
FSP	fiber saturation point
HRR	heat release rate
PDF	probability distribution function

Dedicated to people who lost their lives fighting fires.

Fire is a good servant but a bad master.

—

CHAPTER 1

INTRODUCTION

1.1 Wildfires

Wildfires are uncontrolled fires occurring in a vast area of combustible vegetation in wildlands or wildland-urban interface (WUI) regions. As reported by the National Interagency Fire Center [14], close to 10 million acres of US land were destroyed in 2017 by wildfires. The number of fires reported was around 70 thousand nationally with an associated suppression cost of 2.8 billion dollars. Most of these fires occurred in the westernmost region of the country where climatic conditions are arid and dry. California for instance, accounted for the highest number of structural damage (close to 8000 residential structures) in 2017. With the prevailing drought conditions in these areas, destruction due to wildfires is only expected to become more severe in the future. Wildfires are in fact a global phenomenon occurring at various geographical locations throughout the world. In certain regions in the southern hemisphere such as Australia, the occurrence of bushfires are common due to heat waves and severe drought conditions [53]. These bush fires are non-structural fires which burn grass, bush or forested areas and occur throughout the year. Some of the infamous conflagrations in Australia such as the Ash Wednesday and Black Saturday

fires [19] caused a lot of damage and claimed several lives. Wildfires are also becoming an increasing concern in the recent years in countries such as Greece and Portugal [75]. In 2017, wildfires in Portugal accounted for more than one-third of the burned forest in the European Union. Although wildfires are known for their destructive behavior they also have many beneficial effects on native vegetation, animals, and ecosystems. While many plant species are known to depend on fire for their growth and reproduction, occurrences of wildfire through the historical times conjectures the evolutionary effects of fire on flora and fauna [12]. While wildfires burn decaying matter and enrich the soil with nutrients, they also act as disinfectants by removing disease-ridden plants and harmful insects from the forest ecosystem. The removal of thick canopies and undergrowth in the event of fires also allows sunlight to reach the forest floor resulting in the growth of a new generation of seedlings.

Understanding the cause and spread of wildfires is essential to predict and aid fire management/suppression activities efficiently. Wildfires are initiated either due to natural causes or man made activities. Some of the natural causes include lightning, spontaneous combustion, volcanic eruption etc. However, the most common cause of wildfire ignition (accounting for more than 90% of wildfires) is due to human activities such as arson, sparks from equipments, discarded cigarettes, arcing of power lines etc. These activities often initiated as small sparks transform into large conflagrations in a short time span due to very high spread rates.

Some of the factors contributing to the high spread rate of wildfires are the climatic conditions, slope of the terrain, combustibility of vegetation, ambient wind conditions and creation of spot fires by firebrands. Climate plays an important role in

controlling the fire activity as it regulates vegetation productivity and fuel moisture content. While rainfall may suppress fire activity during a dry season, the fuel build-up during wet years will only increase the burned area in subsequent years, thereby influencing the spread rate of fires [4]. Furthermore, the combined effect of wind and slope enhances the heat transfer between the flame and unburned fuel ahead of it altering the spread rate of wildfires [30]. The phenomenon of spotting caused by firebrands also plays an important role in influencing the rate of fire spread. A detailed description of this mechanism which is the focus of the present work is discussed in the following section.

1.2 Spotting Mechanism

Spotting mechanism, which is the creation of secondary or spot fires by fire-brands (also referred to as embers) that originate from a primary fire, is a potential mechanism for the spread of wildland and WUI fires [2, 48]. Firebrands are burning or glowing fragments of vegetation such as twigs, barks, leaves and in WUI areas, wood shakes and shingles. Firebrands also take the form of hot metal fragments in the event of power line interactions. Many studies in the past were performed to understand the spotting mechanism and the role of firebrands in the spread of fires (see review articles by Koo et al. [48] and Fernandez-Pello [27]).

Firebrands are generated when burning vegetation disintegrates and breaks off from the parent material resulting in smaller burning fragments. The physical and material properties of the embers largely depend on the species of the parent

3

Lofting Stage   Propagation Stage   Deposition Stage
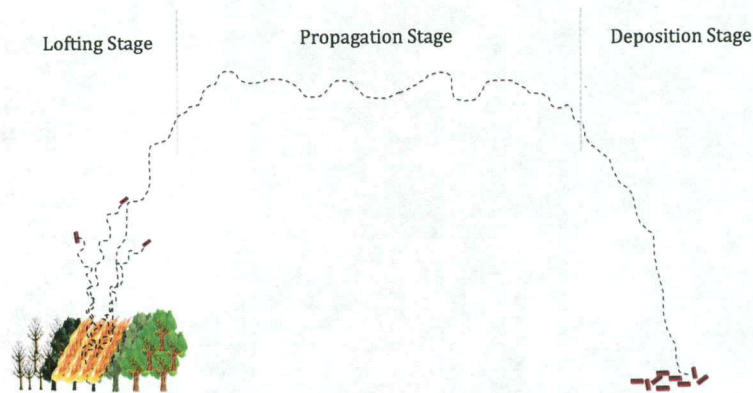
Figure 1.1: Schematic diagram of the three stages of firebrand transport (a) lofting, (b) propagation and (c) deposition.

material and the intensity of the fire. These factors determine the burning properties of firebrands wherein they undergo flaming or glowing combustion.

The motion of a firebrand from generation to landing occurs via three sequential stages, namely, lofting, propagation, and landing, as shown in figure 1.1. These three stages broadly encompass several thermo-chemical and physical mechanisms such as firebrand generation owing to degradation of parent material due to pyrolysis and combustion, aerodynamics during propagation, interaction of firebrand dynamics with air turbulence, heat transfer between firebrands and the recipient fuel and glowing combustion. This work mainly focuses on understanding the stages of propagation and deposition of firebrands.

4

The firebrand conditions such as mass, size and geometrical shape are important to the firebrand motion in all these stages. During the spotting process, the ambient conditions which can change drastically from one stage to another is also an important factor. Depending on the wind conditions, they are carried over a distance ranging from a few meters to tens of kilometers [31]. Based on the distance traversed by the firebrands, spotting can be classified as short-range (few tens of meters), intermediate-range, and long-range (tens of kilometers) [1]. In particular, the intermediate/long range spotting is known to cause destruction of residential structures in WUI regions prior to the arrival of the main fire front [60].

In the lofting stage, it is the convective columns of the primary fire responsible for the predominantly upward motion and lofting of firebrands. The propagation stage may be considered lacking for short-range spotting whereas it can constitute a long section of the overall distance a firebrand travels in long-range spotting. The ambient wind conditions play a significant role in how firebrands are carried in this stage. Firebrands that are sufficiently away from the primary fire are mainly carried by the ambient wind into regions nearly devoid of any direct fire influence. In the landing stage, the firebrands descend and depending on their thermal energy content and ignitability condition of the recipient fuel, they may create spot fires after settling.

1.3 Ignition Characteristics of Vegetation

After landing, the firebrands transfer their thermal energy to the recipient fuel. At the landing stage, firebrands could either be flaming or undergoing glowing combustion. Depending on their thermal content, the firebrands can also act as a

source of pilot ignition. On the other hand, in the long run, a glowing firebrand may also be capable of initiating spontaneous ignition in the recipient fuel. Ignitability of the recipient fuel thereby becomes an important factor in establishing a spot fire. Manzello et al. [57, 58, 59] performed several experiments to asses the vulnerability of vegetative fuel beds and structural materials to ignition on exposure to firebrand showers. From these experiments, Manzello et al. [57] deduced that a single glowing firebrand as opposed to a cluster of them has a potential to ignite paper-based fuel beds. However, multiple glowing firebrands were required to initiate ignition in fuel beds comprising of pine needles and hardwood mulch. Manzello et al. [57] also determined that the glowing surface area of firebrands is an important parameter to initiate ignition in fuel beds.

Some of the properties of the recipient fuel which play important roles in determining ignitability are type of species, density and moisture content. Fuel moisture content (FMC) plays an important role in determining the limiting condition for ignition of recipient fuel [27]. Dead fuels with moisture content greater than 40% do not aid in fire spread, however, crown fuels comprising of live vegetation with moisture content greater than 70% carry extremely vigorous fires [65]. Often the vegetation in places like California, comprising of live fuels are known to exhibit extreme fire behavior including crowning, spotting and potential development of plume dominated fires [77]. Hence, understanding how live fuels undergo ignition is crucial in determining the capability of firebrands to initiate spot fires when the recipient fuel is live.

In the following section, literature based on live fuel ignitions is reviewed. These works provide an insight into the relationship between FMC and ignition time.

Piloted ignition experiments of cellulosic materials were performed and correlations between moisture content and ignition times were deduced [7, 70, 100]. For woody fuels, it was found that moisture increased the energy required for ignition, resulting in a delayed ignition time. Ignition time was then correlated with moisture content and material properties of wood such as emissivity, thermal conductivity and density. FMC in live fuels exhibited diurnal and seasonal variation during which both dry and moist weight of the fuels vary [10, 40, 84, 112]. Experiments conducted by Dimitrakopoulos and Papaioannou [24], McAllister et al. [65], Pellizzaro et al. [82], Pickett et al. [85], Smith [101], Weise et al. [115], Xanthopoulos and Wakimoto [119] used live fuels wherein the fuel moisture content evolved naturally over the course of an annual season. Species specific empirical correlations relating ignition time to moisture content for various live vegetation species were established.

McAllister et al. [65] performed piloted ignition experiments, using the Forced Ignition and Flame Spread Test (FIST) apparatus on live fuels such as Douglas-fir (*Pseudotsuga menziesii*) and lodgepole pine (*Pinus contorta*) needles. The natural variation in moisture content and chemical composition was factored in by analyzing fuel samples throughout the growing season. It was also observed that when live fuels were heated, the needles underwent a structural failure resulting in the release of water in an explosive process unlike in dead fuels, wherein water was released through evaporation alone. Ignition times differed for fuels with identical FMC's that were tested during different seasons, due to the structural changes that occur in these fuels [29, 42, 47, 50, 52]. McAllister et al. [65] made an important observation that moisture is released in live fuels at the time of ignition and suggested that

the extremely vigorous fires observed in high moisture content live fuels could be attributed to the different physical mechanisms through which water is stored, causing it to evaporate at different rates. Including the effects of moisture evaporation prior to, and at the time of ignition in fire behavior models is thereby important to better predict ignition characteristics in live fuels.

1.4 Firebrand Propagation

While understanding the ignitability of live fuels is crucial in gaining an insight into the process of ignition in recipient fuels, it is also crucial to understand the pattern in which firebrands are deposited on the recipient fuels. The ground deposition pattern provides an insight on the number of firebrands landing over a given area. For instance, the larger the number of firebrands depositing in a given area, it is reasonable to expect that it would lead to a higher probability for creation of spot fires. Some of the important factors which determine the number of firebrands landing in a given area are the air turbulence, firebrand density and the elevations from which firebrands descend.

Several works have been performed in the past focusing on predicting firebrand motion during flight. One of the pioneering works in this regard was performed by Tarifa et al. [107]. They performed wind tunnel experiments with spherical and cylindrical tethered firebrands of various sizes and material properties. From these experiments, correlations for drag were found and the paths followed by firebrands determined numerically. In the numerical calculations, they made two critical assumptions: firebrands fall at their terminal velocities and the horizontal velocity

8

component of the firebrands is equal to that of the background fluid velocity. Anthe-nien et al. [5], Stephen and Fernandez-Pello [105] simulated propagation of firebrands in an atmospheric boundary layer modeled by a prescribed horizontal velocity, which varied with elevation according to the logarithmic or power law correlation. Furthermore, Stephen and Fernandez-Pello [105] assumed firebrands to be spherical in shape and influenced by drag and gravity forces. Manzello et al. [56, 57] conducted experiments by burning Douglas-fir and Korean pine trees and analyzed the size and mass distribution of the generated firebrands. From these experiments it was found that cylinders are the most common shapes for firebrands. The diameter of the cylindrical firebrands was measured to be of the order of few millimeters and the length was few tens of millimeters. Recently, Suzuki and Manzello [106] quantified physical characteristics of firebrands collected from an urban fire. Suzuki and Manzello [106] observed that the size and mass distribution of the firebrands were independent of the deposition location. The largest firebrand was measured to have a mass of 114 g with a projected area of 130 cm^2, whereas more than 60% of the firebrands had mass less than 0.1 g with a significantly lower projected area of 2 cm^2. A similar observation was also made in the tree burn experiments of Manzello et al. [56, 57], where, regardless of the species and tree height, majority of the generated firebrands were measured to have mass less than 0.1 g.

In more recent numerical works, firebrands were modelled to be cylindrical and/or disk-shaped under the action of the forces of drag, lift and gravity [36, 49, 78, 96, 97]. The propagation of firebrands lofted by buoyant plumes representing wildfires in cross flows has been the subject of previous computational fluid dynamics (CFD)

based works [38, 49, 96, 97, 110]. Huang et al. [38], Koo et al. [49], Sardoy et al. [96, 97] described the background flow by the Reynolds averaged Navier-Stokes (RANS) equations. They used a k-ϵ model for the treatment of the closure problem, except Koo et al. [49] who used a one-equation model. In Sardoy et al. [96], a stable thermal atmosphere was also assumed, leading to a decrease in the ambient temperature with height. The firebrands were lofted by the buoyant plume and their propagation downwind was aided by the atmospheric boundary layer. Koo et al. [49] observed that firebrands lofted by buoyant plumes created by canopy fires travelled further than that created by surface fires. Also, in comparison to cylindrical firebrands, Koo et al. [49] observed that disc shaped firebrands travelled a longer distance in the streamwise direction. For the case of canopy fires, Sardoy et al. [97] deduced that the landing distance was insensitive to the initial velocity of firebrands, as the firebrand velocity approached that of the ambient flow in short time scales. However, in these works it must be noted that the explicit role of turbulent fluctuations in the motion of firebrands was neglected. A precise description of turbulent dispersion/diffusion of firebrands requires a full resolution of these fluctuations. Since the impact of turbulent fluctuations was neglected, the dispersion and diffusion of firebrands were further underestimated. In such scenarios validating the mean flow or turbulent stresses is also not feasible. In these works, while the buoyant plume was modeled as a heat source or through an integral plume model, the inlet condition describing the atmospheric boundary layer was always modeled in terms of the logarithmic or power law correlation.

Himoto and Tanaka [36], Pereira et al. [83], Thurston et al. [109], Tohidi and Kaye [110] conducted large-eddy simulation (LES) to model the background flow field. In LES, resolved velocities are used to advance firebrands so the turbulent fluctuation effects on firebrands are directly taken into account to a great extent. Only the effects of the subgrid-scales (SGS), which contain significantly less turbulent kinetic energy than the resolved scales, are discarded on firebrands. Himoto and Tanaka [36] considered disk-shaped firebrands under the drag, lift, and gravitational forces and released them from a point very close to the ground over a heat source representing a primary fire and found that the distribution of landed firebrands exhibited a log-normal function in the streamwise direction and a normal distribution in the spanwise direction. Pereira et al. [83] treated firebrands as spherical particles subject to drag and gravitational forces. Thurston et al. [109] completely neglected firebrand inertia, assuming the firebrand velocity as the sum of the still-fluid terminal velocity and the resolved velocity of the background flow. This neglect is valid only for firebrands with very small masses [64].

Tohidi and Kaye [110] conducted LES for their experimental configuration [111] where non-burning firebrands were released in a combined field of two canonical wall-bounded flows: a fully developed channel flow and a fully developed pipe flow. In this configuration, firebrands were mainly lofted by the updraft of the fully developed pipe flow and propagated downwind by the combined flow field. The firebrand paths for various firebrand sizes were then statistically characterized as a function of the downwind distance. Tohidi and Kaye [111] observed firebrands to rotate significantly and at times, move transverse to the wind direction. Hence, modelling lift and ro-

11

tational effects on firebrands was also emphasized in their work. The interaction of these flows somewhat resembled the cross-flow condition in a wildfire event; however, this interaction did not account for the non-isothermal buoyancy effects. Although turbulent fluctuations were accounted in their simulations, the effect of these fluctuations on the dispersion and deposition of firebrands was not characterized. Also, in their work, while a laboratory scale wind tunnel was used to establish the flow field, the firebrand size was not scaled in consistent with the dimensions of the wind tunnel and hence geometric similarity was not satisfied. Hence, applicability of these results for a real-scale atmospheric boundary layer and applicability in terms of short-range or long-range spotting is not clear. It is thereby crucial to understand the impact of turbulent fluctuations on the firebrands to better understand the propagation stage of the spotting mechanism.

1.5   Motivation and Objectives

The goal of the present work was two fold. First, to investigate the ignition characteristics of live fuels by piloted ignition, which helps to improve our understanding of the ignitability condition of recipient fuels as relevant to the landing stage in the spotting mechanism. The live fuel ignition study was mainly guided by the experiments of McAllister et al. [65]. As discussed in Section 1.3, live fuels exhibit different rates of moisture evaporation. This is attributed to the distinct states in which water is stored: free state and bound state. Free water in live fuels exists within the cell cavities, whereas bound water exists within the cell walls. The main focus of this work was to improve the conventional FMC evaporation model for live fuels by in-

12

cluding the effects of both free and bound water and thereby determine the ignition characteristics of live fuels.

Second, to investigate the explicit role of turbulence in the propagation and deposition of firebrands for an intermediate spotting range. Winds, which are characterized by turbulence, are critical in the spread of wildland and WUI fires. In particular with respect to firebrands, turbulence is expected to play a unique role in the propagation of firebrands by dispersing and diffusing them, and hence influencing their landing locations. The turbulent boundary layer (TBL) in the atmosphere is found to be similar to that of the canonical flat plate boundary layer [51]. In the past, several studies have approximated this boundary layer by using the power law or logarithmic correlation to estimate wind speeds as a function of elevation above the ground [9, 35, 38, 96, 97]. Random turbulent fluctuations are then superimposed on this mean profile to represent a TBL [9, 35]. However, the Reynolds stresses obtained from such a method compares poorly with that of the canonical TBL. The focus of this work, is to study the dispersion of firebrands in a more realistic TBL. The specific objectives of the current study are:

- To investigate live fuel ignitions and their mass loss rates influenced by free and bound water evaporation.

- To study the impact of air turbulence in the dispersion of flying firebrands for the intermediate range of spotting.

- To investigate and quantify the ground deposition pattern for firebrands falling under the influence of a TBL.

13

- To determine the thermal content of firebrands after landing and thereby identify regions prone to the creation of spot fires.

1.6 Outline

Following the introduction and motivation presented in Sections 1.1-1.6, a detailed formulation of the physics based model utilized for the firebrand study is presented in Chapter 2. The investigation of pyrolysis models is discussed in Chapter 3. The dispersion and deposition of firebrands in a TBL without considering the effects of thermal degradation is discussed in Chapter 4. Next, the effect of thermal degradation is included and the dispersion and deposition of the firebrands is investigated in Chapter 5. Summary of the work, important conclusions and some recommendations for future work are proposed in Chapter 6. The Appendix contains discussion on the computational methodology of the turbulent inflow boundary condition and additional figures associated with the discussion of results in Chapters 4 and 5.

CHAPTER 2

MATHEMATICAL AND COMPUTATIONAL METHODOLOGY

As noted in Chapter 1, the current study comprises of understanding the ignition characteristics of live fuels which is relevant to the landing stage of firebrands and understanding the dispersion and deposition of firebrands in a turbulent flow field. This involves many underlying physical phenomena such as fluid dynamics, combustion and thermal degradation of solid fuel. It also constitutes the transport of Lagrangian particles such as firebrands coupled with the fluid flow. In this work, the Wildland-urban interface Fire Dynamics Simulator (WFDS-SVN 9977) is employed to achieve the research objectives outlined in Chapter 1. WFDS is an extension of the capabilities of the Fire Dynamics Simulator (FDS5) to outdoor fire spread problems [69]. WFDS uses the method of computational fluid dynamics to solve the governing equations pertaining to fluid motion, combustion and heat transfer in a three-dimensional framework. The method of large-eddy simulation is used to deal with turbulence in WFDS. Since the relevant governing equations are standard and described comprehensively in the references cited [67, 69], they are not described here. In Chapter 3, to study live fuel ignitions, WFDS was adapted by modifying the existing moisture evaporation model (discussed in detail in Chapter 3). In Chapter 4

15

and Chapter 5, to study the dispersion of firebrands, WFDS was modified extensively to include equations to solve for the dynamical and thermal behavior of firebrands. Additional boundary conditions to generate TBLs was also added as a new feature. Results from the model described in the following section are presented in Chapter 4 and Chapter 5.

2.1 Background Flow Equations

The Wildland-urban interface Fire Dynamics Simulator (WFDS) [67, 69], as set up to use the dynamic Smagorinsky model for the SGS stresses for LES, is employed to study the dispersion of firebrands in a TBL. The dynamic Smagorinsky model has the advantage that the model coefficient in the calculation of eddy viscosity is dynamically calculated based on the local flow conditions without a prior specification of the coefficient. The transport of firebrands in the current work is studied for the intermediate range spotting at regions away from the influence of the main fire. Here, the impact of heat transfer from the main fire on the background flow or the transport of firebrands is insignificant. Therefore, for the results described in Chapter 4 and Chapter 5, the influence of heat transfer or combustion processes on the fluid dynamics were not considered and the features that model the transport of energy and chemical species in WFDS were not utilized.

2.2 Firebrand Equations

The firebrands are assumed cylindrical, undergoing both translational and rotational motions. These motions are described in the Lagrangian framework through

16

solving a set of equations that are presented here for individual firebrands. The equations pertaining to translational motion are solved in the fixed inertial frame (x, y, z) (also used for the fluid equations) and the rotational motion equations are solved in the particle reference frame (x_r, y_r, z_r), which is attached to the firebrand and can translate and rotate depending on the motion of the firebrand. An identical approach was used by Oliveira et al. [78] for the description of firebrand motion. The firebrands are treated as point particles and the impact of SGS on them is neglected. Heavier firebrands are expected to be less sensitive to SGS fluctuations. There are previous models based on deterministic approaches, e.g., Shotorban and Mashayek [98], or stochastic approaches, e.g., Shotorban and Mashayek [99], to take the effects of these fluctuations into account for spherical particles experiencing the drag force. The extension of these models to include cylindrical particles is not trivial and beyond the scope of the current study.

2.2.1 Firebrand Translation

The translational motion equations of firebrands are presented in this section. Figure 2.1 shows a schematic diagram with the forces acting on a cylindrical body carried by in a flow.

If $\vec{x}_{\mathrm{p}}(t)$ and $\vec{V}_{\mathrm{p}}(t)$ denote the position and velocity of the center of mass, then

$$\frac{d\vec{x}_{\mathrm{p}}}{dt} = \vec{V}_{\mathrm{p}},$$

(2.1)
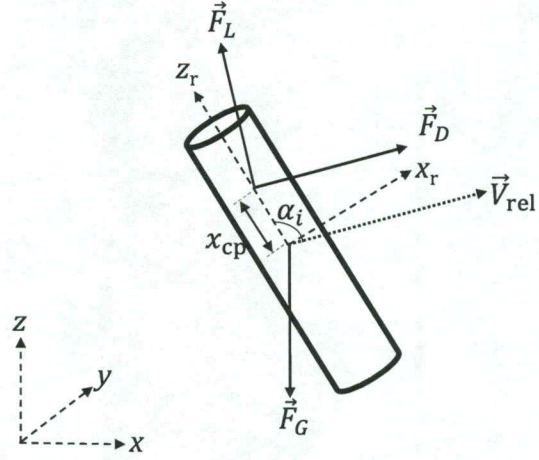
Figure 2.1: Schematic diagram of a cylinder in a cross flow with the inertial and rotating coordinate systems, and acting forces.

$$m_{\mathrm{p}}\frac{d\vec{V}_{\mathrm{p}}}{dt} = \vec{F}_G + \vec{F}_D + \vec{F}_L, \tag{2.2}$$

where m_{p} is the firebrand mass and $\vec{F}_G$, $\vec{F}_D$, and $\vec{F}_L$ are the gravitational, drag, and lift forces, respectively. Equation 2.1 is the standard definition of velocity given in terms of the rate of change of position and Equation 2.2 is defined based on the Newton's second law. Here $\vec{F}_G$, which includes the buoyancy effect, is given by:

$$\vec{F}_G = (\rho_\text{p} - \rho_\text{gas})V_\text{p}\vec{g}, \tag{2.3}$$

where ρ_p and ρ_gas denote the density of the firebrand and the carrier flow, respectively, V_p is the firebrand volume, and $\vec{g}$ is the gravitational acceleration. In Equation 2.2, $\vec{F}_D$ and $\vec{F}_L$ are calculated through a model proposed by Hoerner [37] for cylindrical objects:

$$\vec{F}_D = 2C_D \rho_\text{gas} ab|V_\text{rel}||\sin\alpha|^3 \vec{V}_\text{rel}, \tag{2.4}$$

$$\vec{F}_L = 2C_D \rho_\text{gas} ab \left(|V_\text{rel}|\sin\alpha\right)^2 \cos\alpha \frac{\hat{z}_r \times \vec{V}_\text{rel} \times \vec{V}_\text{rel}}{|\hat{z}_r \times \vec{V}_\text{rel} \times \vec{V}_\text{rel}|}, \tag{2.5}$$

where a and b denote the radius and length of the cylinder, respectively, $\vec{V}_\text{rel}(t) = \vec{U}(\vec{x}_\text{p}(t), t) - \vec{V}_\text{p}(t)$ is the cylinder velocity relative to the local flow, where $\vec{U}(\vec{x}, t)$ is the resolved Eulerian velocity of the fluid flow. The model proposed by Hoerner [37] was based on experiments performed on cylindrical objects, wires and cables subjected to cross-flow scenarios. This model is more suitable for cylindrical objects subjected to flows with sub-critical Reynolds numbers, $\text{Re}_b < 10^5$. It is noted that the Hoerner's assumption serves as a limitation in determining the drag coefficient in the event of flow separation and generation of wake behind cylindrical objects.

In computations, $\vec{U}(\vec{x}_\text{p}(t), t)$ is calculated via a trilinear interpolation of the flow velocities at cell faces to the location of firebrand. In Equation 2.5, $\hat{z}_r$ is the unit vector in the axial direction of the cylinder, and α is the incidence angle between the relative velocity vector and $\hat{z}_r$. Based on experiments involving cylindrical rigid bodies

19

subjected to cross-flow, the drag coefficient proposed by Kelbaliyev [46], Oliveira et al.

[78] is used. This drag coefficient is given by

$$
C_D = \begin{cases}
\frac{10}{Re_\alpha^{0.778}}, & \text{for } Re_\alpha \leq 0.1 \\[2em]
\frac{10}{Re_\alpha^{0.778}} \left[1 + \frac{Re_\alpha^{1.875}}{60 + 6.8 Re_\alpha^{1.156}} \right], & \text{for } 0.1 < Re_\alpha \leq 6 \times 10^3 \\[2em]
1.1, & \text{for } 6 \times 10^3 < Re_\alpha \leq 2 \times 10^5,
\end{cases}
\tag{2.6}
$$

where Re_α is Reynolds number defined by $Re_\alpha = 2\rho a |V_{rel}| \sin\alpha / \mu$ with μ.

2.2.2 Firebrand Rotation

In the non-stationary reference frame attached to the firebrand, the equations

describing the rotational motion as given by the Euler rotation equations read:

$$
\mathbf{I} \cdot \frac{d\vec{\omega}}{dt} + \vec{\omega} \times (\mathbf{I} \cdot \vec{\omega}) = \vec{T},
\tag{2.7}
$$

where $\mathbf{I}$ is the moment of inertia and $\vec{\omega}$ is the angular velocity of the firebrand. The

moment of inertia measured along the principle axes of the cylindrical firebrand is

given as, $\mathbf{I}_{x'} = \mathbf{I}_{y'} = m_p a^2 / 4 + m_p b^2 / 3$ and $\mathbf{I}_{z'} = m_p a^2 / 2$. The torque $\vec{T}$ is given as

$$
\vec{T} = \vec{T}_{resis} + \vec{T}_{hydro},
\tag{2.8}
$$

20

where $\vec{T}_{\mathrm{hydro}}$ is the torque due to hydrodynamic force, and $\vec{T}_{\mathrm{resis}}$ is the frictional torque due to air resistance. The torque due to hydrodynamic force is caused when the center of pressure (location at which the net aerodynamic forces act) and the center of mass (location of geometric centre) of the firebrand are non-coincident

$$\vec{T}_{\mathrm{hydro}} = x_{\mathrm{cp}}\mathbf{A} \cdot \left[\hat{z}_r \times (\vec{F}_D + \vec{F}_L)\right],\tag{2.9}$$

where x_{cp} is the distance between the centre of pressure and the centre of mass of the firebrand [61]. This location varies depending on the incidence angle of the firebrand and is computed via:

$$x_{\mathrm{cp}} = 3b|\pi/2 - \alpha|/8\pi.\tag{2.10}$$

The sign of x_{cp} and hence the associated torque is determined by the sign of $\cos\alpha$ as given in Yin et al. [124]. In Equation 2.9, $\mathbf{A}$ is a transformation matrix given as,

$$\mathbf{A} = \begin{pmatrix} 1 - 2(\epsilon_2{}^2 + \epsilon_3{}^2) & 2(\epsilon_1\epsilon_2 + \epsilon_3\eta) & 2(\epsilon_1\epsilon_3 - \epsilon_2\eta) \\ 2(\epsilon_2\epsilon_1 - \epsilon_3\eta) & 1 - 2(\epsilon_3{}^2 + \epsilon_1{}^2) & 2(\epsilon_2\epsilon_3 + \epsilon_2\eta) \\ 2(\epsilon_3\epsilon_1 + \epsilon_2\eta) & 2(\epsilon_3\epsilon_2 - \epsilon_1\eta) & 1 - 2(\epsilon_1{}^2 + \epsilon_2{}^2) \end{pmatrix},\tag{2.11}$$

where $\epsilon_1, \epsilon_2, \epsilon_3$ and η denote the quaternions [33].

Since the aerodynamic forces are calculated in the inertial reference frame, a transformation matrix, $\mathbf{A}$ is used to obtain the hydrodynamic torque in the particle reference frame. The components of the transformation matrix are calculated as a function of the four Euler parameters (also called quaternions).

In Equation 2.8, the frictional torque is determined by:

$$\vec{T}_{\text{resis}} = -\rho|\vec{\omega}|ab^4 \left\{ 0.538 + 3.62 \left(\frac{\rho|\vec{\omega}|ab}{\mu} \right)^{-0.778} \right\} \vec{\omega}, \qquad (2.12)$$

which acts a resistive torque and hence reduces the angular velocity of the firebrand.

The formulation in Equation 2.12 was adapted from Oliveira et al. [78], wherein, a

local rotational drag coefficient is integrated over the length of the cylinder to obtain

the overall resistance. The constants in Equation 2.12 are based on experiments

performed on cylindrical objects subjected to cross-flow scenarios [46]. The resistive

torque is calculated in the firebrand rotational reference frame and hence a co-ordinate

transformation is not required. The orientation of the cylinder is tracked in terms of

the Euler parameters instead of the Euler angles, thereby eliminating the singularity

problem. Finally, the ordinary differential equations used to track the evolution of

the Euler parameters [76, 123] in terms of the angular velocity are:

$$\begin{bmatrix} \frac{d\epsilon_1}{dt} \\[2mm] \frac{d\epsilon_2}{dt} \\[2mm] \frac{d\epsilon_3}{dt} \\[2mm] \frac{d\eta}{dt} \end{bmatrix} = \frac{1}{2} \begin{bmatrix} \eta\omega_x - \epsilon_3\omega_y + \epsilon_2\omega_z \\[2mm] \epsilon_3\omega_x + \eta\omega_y - \epsilon_1\omega_z \\[2mm] -\epsilon_2\omega_x + \epsilon_1\omega_y + \eta\omega_z \\[2mm] -\epsilon_1\omega_x - \epsilon_2\omega_y - \epsilon_3\omega_z \end{bmatrix} . \qquad (2.13)$$

2.2.3 Firebrand Burning

During transport, firebrands thermally degrade and thereby lose mass and

also exchange heat with the surroundings. Since the dimensions of the firebrands

considered in the current work are approximately few millimeters in diameter and few centimeters in length, the thermally thin model is used. According to this model, the temperature of the firebrands is assumed to be spatially uniform throughout its entirety. In such a case, the conduction thermal resistance of the firebrand is less significant as compared to its convection thermal resistance. During burning, firebrands experience mass loss due to the processes of pyrolysis and char oxidation. Arrhenius-type rate equations were used to model the processes of pyrolysis and char oxidation. Firebrands also exchanged heat with the surrounding air through the mechanisms of convection and thermal radiation. The energy equation for the firebrand is given as:

$$m_{\mathrm{p}}c_{\mathrm{p}}\frac{dT_{\mathrm{p}}}{dt} = -\Delta h_{\mathrm{pyr}}\dot{m}_{\mathrm{pyr}} - \Delta h_{\mathrm{char}}\dot{m}_{\mathrm{char}} - \nabla \cdot \mathbf{q}_c - \nabla \cdot \mathbf{q}_r, \tag{2.14}$$

where T_{p}, is the firebrand temperature and c_{p} is its heat capacity set equal to 1466 J/kg-K [97]. The first two terms on the right hand side of Equation 2.14 represent the energy release due to the process of pyrolysis and char oxidation, respectively. Here, Δh_{pyr} represents the enthalpy of volatilization and is equal to 418 kJ/kg [69, 96] and Δh_{char} is the enthalpy of char oxidation set equal to 12×10^3 kJ/kg. In Equation 2.14, $\mathbf{q}_c$ and $\mathbf{q}_r$ denote convective and radiative heat fluxes of the firebrand. These fluxes are modeled as:

$$\nabla \cdot \mathbf{q}_c = hA(T_{\mathrm{p}} - T_\infty), \tag{2.15}$$

23

$$\nabla \cdot \mathbf{q}_r = \sigma \epsilon A(T_{\mathrm{p}}^4 - T_{\infty}^4). \tag{2.16}$$

In Equation 2.15, A is the surface area of the firebrand and h is the convective heat transfer coefficient calculated through the Nusselt number relation, $h = \mathrm{Nu}k/d$. Here, a formulation of the Nusselt number for cylindrical objects in cross-flow scenarios is used [16].

$$\mathrm{Nu} = 0.3 + \frac{0.62\mathrm{Re}^{1/2}\mathrm{Pr}^{1/3}}{[1 + (0.4/\mathrm{Pr})^{2/3}]^{1/4}} \left[1 + \left(\frac{\mathrm{Re}}{282000}\right)^{5/8}\right]^{4/5}, \tag{2.17}$$

In Equation 2.16, σ is the Stefan-Boltzmann constant and ϵ is the emissivity, set equal to 0.9, which is a characteristic of wildland vegetation [69]. The activation temperature and the pre-exponential factor used in the Arrhenius equations are based on the *Pinus* species. The equation for the mass evolution of the firebrand is given as:

$$\frac{dm_{\mathrm{p}}}{dt} = -\dot{m}_{\mathrm{pyr}} - \dot{m}_{\mathrm{char}}, \tag{2.18}$$

where for $i \equiv \mathrm{pyr}\ \mathrm{or}\ \mathrm{char}$

$$\dot{m}_i = -m_i A_i \exp\left(\frac{-E_i}{RT_{\mathrm{p}}}\right), \tag{2.19}$$

where m_i represents mass, $\dot{m}_i$ is the mass loss rate, A_i is the pre-exponential factor, T_{p} represents the vegetation temperature, R is the universal gas constant and E_i is

the activation energy. In Table 2.1, A_i and the activation temperature, defined by $T_i = E_i/R$, are tabulated for different firebrand species and char oxidation [34, 71].

Table 2.1: Thermokinetic parameters for burning firebrands [34, 71].

Species	A_i	T_i (K)
Pyrolysis gas	725 (s^{-1})	6899
Char	430 (m/s)	9000

2.3 Numerical Integration of Firebrand Equations

The time integration scheme for the fluid solver in WFDS is a second order Runge-Kutta (RK) predictor-corrector method with a varying time step. The firebrand equations are solved using a second order Adams Bashforth (AB2) scheme [88], with a time step twenty times smaller than the current time step used in the RK scheme for the fluid flow equations. The Adams Bashforth scheme has the advantage that it takes into account the variable time step as determined by the fluid solver to predict the solution at the successive integration step. According to the Adams Bashforth scheme, for a differential equation of the form $dy/dx = f(x, y)$, the value at the next integration step $y(x_{k+1})$ is given as:

$$y(x_{k+1}) = y(x_k) + f(x_k, y_k)h_k \left(1 + \frac{\alpha_k}{2}\right) + f(x_{k-1}, y_{k-1})h_k \left(-\frac{\alpha_k}{2}\right). \qquad (2.20)$$

25

Here, $\alpha_k = h_k/h_{k-1}$ is the ratio between the discrete integration steps at the current and previous values.

The Adams Bashforth scheme implemented in WFDS was also numerically verified for a simplified case of a spherical particle for which an analytical solution was known. In this case, the effect of lift was neglected and only the forces of drag and gravity were considered. There was no wind and it was assumed that the firebrand does not experience mass loss. The drag force, $\vec{F}_d = 6\pi\mu R\vec{V}_{\text{rel}}$, given by the Stokes law was assumed to be linearly dependent on the relative velocity. Here, μ and R are the viscosity of air and radius of particle respectively. The viscosity of air was considered to be 1.85×10^5 kg/m-s. The analytical solutions for the velocity and position for such a case is:

$$\vec{V}_{\text{p}} = \vec{C}e^{\frac{k}{m_{\text{p}}}t} - \frac{v_{\text{p}}(\rho_{\text{p}} - \rho_{\text{gas}})\vec{g}}{k},\tag{2.21}$$

$$\vec{x}_{\text{p}} = \int \vec{V}_{\text{p}}dt + \vec{B} = \frac{m_{\text{p}}\vec{C}}{k}e^{\frac{kt}{m_{\text{p}}}} - \frac{v_{\text{p}}(\rho_{\text{p}} - \rho_{\text{gas}})\vec{g}}{k}t + \vec{B}.\tag{2.22}$$

Here, $k = 6\pi\mu R$, $\vec{B}$ and $\vec{C}$ are the integration constants. As a test case, the radius of the spherical particle is considered to be 5 cm and the mass is 3.7 g and $\rho_{\text{p}} \gg \rho_{\text{gas}}$. These values are of the order of length scales of firebrand particles as observed by experiments [57]. The path followed by the particle is tracked and compared with analytical solutions obtained using the same initial conditions. In this case it is observed that the particle takes 1.74 s to reach the ground. figure 2.2 (a) shows the variation of the height of the particle from the ground at various instances

26

in time and figure 2.2 (b) shows the variation of distance covered by the particle in the horizontal direction. It is observed that the solution obtained by solving the particle momentum equation using the variable Adams Bashforth scheme matches exactly with the analytical solution.

For the above case, the convergence of the solution with reduction in time step was also investigated as shown in figure 2.3. To estimate the error, the exact solution was first determined from the finest time step of $\Delta t = 0.001$ s. Solutions obtained from coarser time steps were then subtracted from the exact solution to determine the temporal discretization error. The errors thus obtained were then plotted as a function of the time steps. The error for time steps less than 0.01 is of the order 10^{-4} s. Also, the slope estimated from the AB2 scheme is comparable to the ideal slope expected for a second order discretization method, which is a straight line, $y = x^2$ on a log-log scale. For all the simulations considered in the current work, the discrete time integration steps was close to 10^{-4} s.
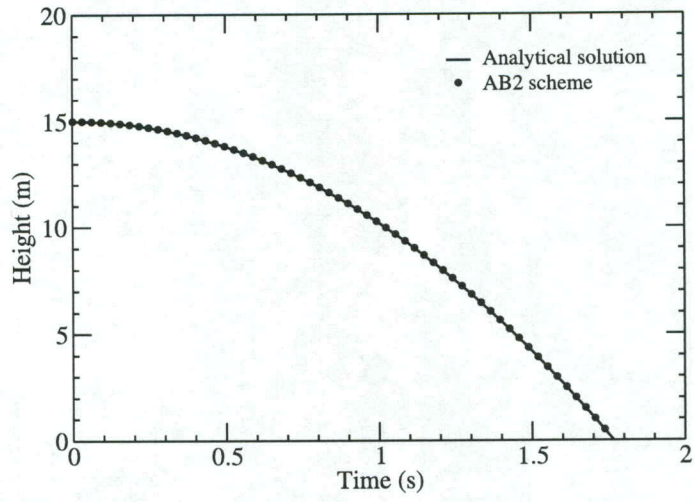
(a)
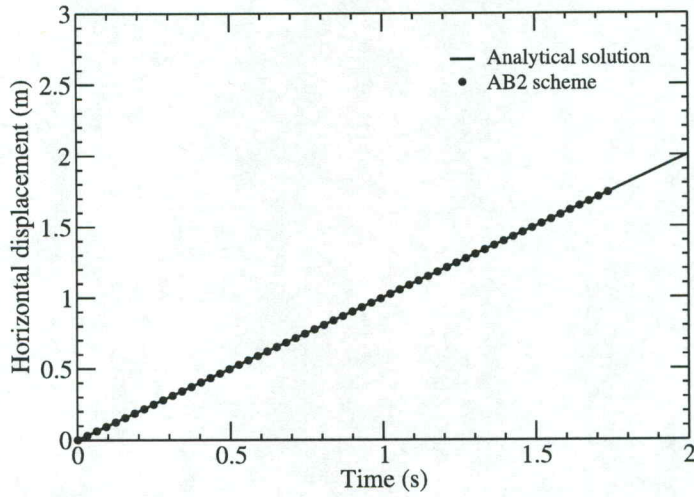
(b)

Figure 2.2: Numerical verification of the Adams Bashforth scheme for a spherical particle undergoing Stoke's drag.
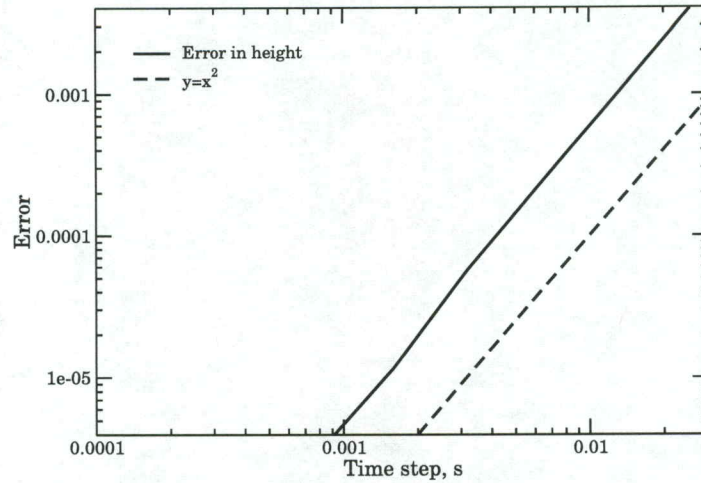
Figure 2.3: Verification of the second order Adams Bashforth time integration scheme; showing variation in discretization error versus time step

2.4 Generation of Turbulent Boundary Layer

As discussed in Chapter 1, the current work is most relevant to the landing stage of intermediate or long-range spotting. For this range of spotting, firebrands travel distances of the order of several meters away from the primary fire front. The effect of the primary fire on the background flow or the transport of firebrands is insignificant. In these regions, firebrands are mainly transported and dispersed by the turbulent atmospheric flow field devoid of any thermal effects. To model such a flow, in the current work, an atmospheric flow field which represents a neutral TBL is considered. Such a TBL is observed to closely follow the canonical turbulent boundary flow over a smooth flat plate [51]. Generation of such a TBL often requires

a lengthy developmental section, starting from a laminar flow and transitioning to a TBL at downstream locations. To obviate the need for a lengthy developmental section, a recycling method is implemented here to generate a TBL based on the work of Lund et al. [54]. The recycling method is advantageous in the sense that it is computationally less expensive and produces a realistic TBL with statistics in good agreement with well established experiments on canonical turbulent boundary flows. Here, the recycling method proposed by Lund et al. [54] was added as a new feature to WFDS. The recycling method is capable of generating a TBL from the inlet of a computational domain. The velocity components at a downstream location are rescaled and recycled at the inlet to generate the TBL. The premise behind this approach is the inherent similarity in the mean and turbulence properties exhibited by TBLs. The recycling procedure is briefly reviewed in this section and detailed discussion pertaining to the scaling procedure has been provided in the Appendix.

According to this method, the velocity field at the inlet of the domain is first initialized using the Spalding law in the mean sense. The Spalding law is a single formula, which relates the non-dimensional velocity to the non-dimensional wall normal distance, spanning the entire TBL height. At the inlet, the Spalding law is also superimposed with random fluctuations of 10% turbulent intensity. Such a flow develops to yield a realistic TBL at a downstream location in the domain. Once such a flow reaches a statistically stationary state, the velocity components at the inlet plane are obtained by the recycling method. The recycling plane is set to a location 80% downstream of the domain as shown in figure 2.4.
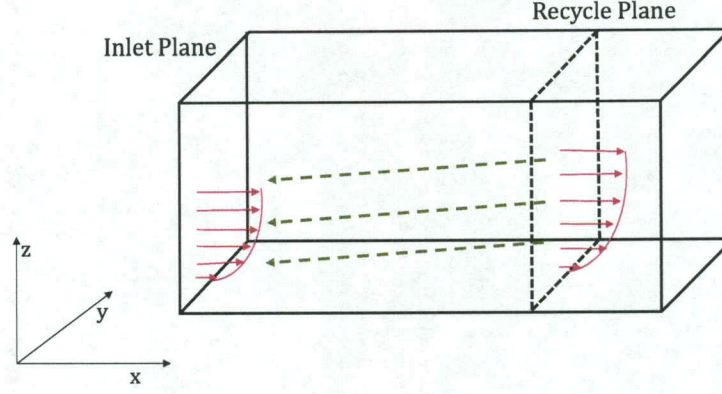
(a)

Figure 2.4: Schematic diagram of the inlet boundary condition calculated via recycling technique

At the recycling plane, the velocity components in the inner and outer layer of the boundary layer are decomposed into a mean, U_i and its fluctuating part, u_i''. Here, the mean velocity is based on an average calculated over both, spanwise direction and time. Since the velocity profile satisfies scale similarity within the boundary layer, a scaling factor based on friction velocity is used to rescale the mean and fluctuating components. To apply the recycling procedure, first the TBL is divided into inner and outer regions. In the inner region where viscous effects are predominant, the law of the wall is used to relate the velocity components at the recycling plane to that of the inlet plane. Similarly, away from the wall, in the outer region, the law of the wake [17] is used. Accordingly, the composite profile over the entire boundary layer is represented by

$$(u_i)_{\text{inlet}} = [(U_i)_{\text{inlet}} + (u^{'}_{\ i})_{\text{inlet}}]^{\text{inner}}[1 - W(\eta_{\text{inlet}})] \ +$$

$$[(U_i)_{\text{inlet}} + (u^{'}_{\ i})_{\text{inlet}}]^{\text{outer}}[1 - W(\eta_{\text{inlet}})], \tag{2.23}$$

where

$$W(\eta) = 0.5\left[\frac{1 + \tanh\left[\frac{\alpha(\eta-b)}{(1-2b)\eta+b}\right]}{\tanh(\alpha)}\right] \tag{2.24}$$

is the weighting function which takes into account the transition from inner to outer

layer. The parameters α and b are equal to 4 and 0.2 respectively. These values are

chosen such that the weighting function is zero at $\eta = 0$ and unity at $\eta = b$. Hence,

at the inner region of the boundary layer, the term $[1 - W(\eta_{\text{inlet}})]$ has more weight

and at the outer region of the boundary layer, $W(\eta_{\text{inlet}})$ has more weight.

The other boundary conditions used in the recycling method is described in

the rest of the section. At the top boundary of the domain, the vertical component of

the gradients of horizontal and lateral velocities, $\bar{u}$ and $\bar{v}$ respectively, are set to zero

as given in Equation 2.25. The vertical component of velocity, $\bar{w}$ is computed based

on the mean free stream horizontal velocity, U_∞ and displacement thickness of the

TBL, δ^*, as given in Equation 2.25. The derivative is obtained by first calculating the

displacement thickness as a function of the streamwise distance and then performing

a linear regression to determine $d\delta^*/dx$,

$$\frac{\partial \bar{u}}{\partial z} = 0, \quad \frac{\partial \bar{v}}{\partial z} = 0, \quad \bar{w} = U_\infty \frac{d\delta^*}{dx}. \tag{2.25}$$

At the exit boundary, the convective outflow boundary condition [55, 79] given

in Equation 2.26 was implemented and added as a new feature to WFDS. The con-

vective outflow boundary condition is well suited for the TBL problem wherein the

velocity component perpendicular to the outflow plane is significant. To handle this

boundary condition, a first order upwind differencing scheme was used to discretize

the spatial derivative and the second order explicit predictor corrector scheme was

used to discretize the temporal derivative which is in accordance with the temporal

discretization used in WFDS for the carrier phase equations. In addition, a correc-

tion factor, c is also taken into account to satisfy global mass conservation. Here, c

is computed based on the mean velocity at the inlet,

$$\frac{\partial \bar{u}_i}{\partial t} + c \frac{\partial \bar{u}_i}{\partial x} = 0.$$
(2.26)

In the current work, the boundary layer was simulated for two Reynolds num-

ber cases, i.e., $\mathrm{Re}_\theta = 10^3$ and 10^6, as illustrated in Chapter 4. Here, Re_θ is defined

based on the momentum thickness at the inlet and the freestream velocity [54]. The

viscous layer was resolved at the wall for the low Reynolds number case whereas the

Werner-Wengle wall model [116] was used for the high Reynolds number case with

the first off-wall grid point lying in the logarithmic region of the TBL. The Werner-

Wengle wall model is used to obtain the tangential velocities at the first off wall grid

point. The wall being impermeable, the velocity component normal to it is set equal

to zero. The Werner-Wengle wall model is a piecewise function which relates the

non-dimensional velocity u^+ with the non-dimensional wall co-ordinate y^+. Here, if

33

$y^+ < 11.81$, it is assumed that the first off wall grid point lies within the viscous sub-layer and a linear approximation for velocity is used Equation 2.27. If $y^+ > 11.81$, it is assumed that the same point lies within the logarithmic layer of the boundary layer and a 1/7th power law approximation is used to determine velocity Equation 2.28,

$$u^+ = y^+ \quad \text{for} \quad y^+ < 11.81, \tag{2.27}$$

$$u^+ = 8.3 y^{+1/7} \quad \text{for} \quad y^+ > 11.81. \tag{2.28}$$

In the spanwise direction, the periodic boundary condition is used on the lateral sides of the domain due to spatial homogeneity.

CHAPTER 3

PHYSICS-BASED MODELING OF LIVE WILDLAND FUEL IGNITION EXPERIMENTS IN THE FIST APPARATUS

3.1 Introduction

In this Chapter, the burning characteristics of live fuels by piloted ignition is investigated enabling to better understand the ignitability condition of recipient fuels as relevant to the landing stage in the spotting mechanism. As discussed in Chapter 1, firebrands with sufficient thermal energy can act as a source of pilot ignition and initiate spot fires in the recipient fuel. The possibility of creation of spot fires is dependent on the properties of the recipient fuel such as, type of species, density and moisture content. Amongst these properties, the FMC plays an important role in determining the limiting criteria for ignition of recipient fuel. The FMC is defined as the ratio of moisture mass to dry mass of the fuel. Live fuels have moisture contents much larger than 100% of their oven dry weight [114]. Owing to the differences in chemical composition and how water is stored in live and dead fuels, live fuels burn at fuel moisture contents where dead fuels do not. The moisture of extinction for dead fuels is less than 30% FMC, whereas experiments based on the burning of live fuels [65, 85, 119] show that live fuels can sustain fire spread for FMC beyond the

range prescribed for dead fuels. The most unpredictable fires often occur in crowns of vegetation composed of live fuel elements. These crown fires can be uncontrollable and have a higher spread rate compared to surface fires [95].

Correlations between moisture content and ignition times for cellulosic materials were deduced in the works of Atreya and Abu-Zaid [7], Moghtaderi and Fletcher [70], Simms and Law [100]. For woody fuels, moisture was found to increase the energy required for ignition, resulting in a delayed ignition time. Here, ignition time was determined as function of moisture content and material properties of wood such as emissivity, thermal conductivity and density. McAllister et al. [65] performed piloted ignition experiments, using the Forced Ignition and Flame Spread Test (FIST) apparatus on live fuels considering species such as Douglas-fir (*Pseudotsuga menziesii*) and lodgepole pine (*Pinus contorta*). These fuels were collected throughout the growing season, thereby the natural variation in moisture content and chemical composition was factored in. These two species behaved as thermally intermediate materials with the existence of temperature gradients within the needles during pyrolysis. McAllister et al. [65] observed moisture release in live fuels at elevated temperatures (greater than 100°C). Unlike dead fuels, release of moisture due to structural failure in live fuels was also observed. Fuels tested during different seasons were also found to ignite at different times for the same fuel moisture contents due to the structural changes that occur in these fuels [29, 42, 47, 50, 52].

Since evaporation of water is an endothermic reaction, fuel moisture content affects heat transfer and combustion processes in both solid and gas phases, hence delaying the time to ignition. In the solid phase, moisture affects thermal properties

36

such as density, thermal conductivity and specific heat whereas in the gas phase, water vapor dilutes flammable pyrolysates and absorbs energy [3, 28]. The modeling of a wildland fire by Albini [3] and the modeling of premixed and non-premixed flames by Ferguson et al. [26] showed significant impact of fuel moisture on the flame. While some studies [8, 65, 90] reported the simultaneous evolution of water vapor and pyrolysis gases during ignition, most numerical models [21, 69, 87] for solid fuel degradation considered a sequential process of evolution of water vapor and pyrolysis gases wherein water is assumed to evaporate first (at temperatures close to 100°C), followed by the pyrolysis gas release.

An important parameter which describes the storage of water is the fiber saturation point (FSP). FSP refers to the point in the drying process at which only water bound in the cell walls remains and all other water, called free water, have been removed from the cell cavities. Below FSP, the wood cell shrinks and changes physically. FSP for wood lies in the range 23-30% [43, 94] on a dry weight basis. Previous experiments on live fuels [32, 74, 85] have suggested that free water is released at temperatures close to the boiling point of water while bound water and pyrolysis gases vaporize at temperatures greater than 200°C. Hence, it is important to include these effects in the modeling of moisture in live fuels. Prince [89] and Prince and Fletcher [90] conducted ignition experiments on manzanita leaves and developed evaporation models differentiating live and dead fuels. Their work emphasized modeling bound water in live fuels which accounted for the release of moisture in the temperature range 266-315°C. The models showed a good agreement between predicted and experimental mass loss. Using Arrhenius parameters for bound water Prince and Fletcher [90]

and Yashwanth et al. [121] performed physics-based modeling to study the effect of heating modes and moisture content on ignition of manzanita leaves and found the predicted ignition and burnout time to be consistent with experimental results.

The aim of the present study is to improve the understanding of ignition and combustion of live foliage based on the recent experiments of McAllister et al. [65]. Here, Wildland-urban interface Fire Dynamics Simulator (WFDS SVN9977) [66, 69], in which solid fuels are represented by discrete particles, was used for computations. Since the current version of WFDS does not differentiate between bound and free water in fuel, bound and free water were modeled via Arrhenius rate equations in the solid fuel thermal degradation module. Hence, the fuel was assumed to undergo a three-stage decomposition process, consisting of evaporation of bound and free water, pyrolysis, and char oxidation. The pyrolyzate gas was assumed to be methane that reacted with air through a single-step mixing-controlled chemical reaction [120, 122].

3.2   Numerical Model and Computational Setup

The experimental setup of McAllister et al. [65] described above is replicated in the WFDS framework. WFDS solves the three-dimensional, low Mach number, time dependent transport equations for the flow through the wind tunnel. The large eddy simulation (LES) with Deardorff's model [23] for subgrid-scale terms is utilized to deal with turbulence. To calculate thermal radiation, a radiation transport equation is solved with a non-scattering gray gas assumption. The solid phase is modeled as discrete particles fixed in space. Particles are assumed thermally thin and optically black fuel elements. The convective and radiative heat transfer between the gas phase

38

and solid vegetation particles is assumed present. The solid fuel particles experience mass loss with an increase in temperature. As the temperature of the fuel increases, free water, bound water and pyrolysis gas release occurs and finally char oxidation takes place. The solid phase degradation model for solid fuel is based on the Arrhenius rate equation:

$$\dot{m}_i''' = -m_i''' A_i \exp\left(\frac{-E_i}{RT_{\text{veg}}}\right) \tag{3.1}$$

where m_i''' represents mass per unit volume, $\dot{m}_i'''$ is the mass loss rate per unit volume, A_i is the pre-exponential factor, T_{veg} represents the vegetation temperature, R is the universal gas constant and E_i is the activation energy. Here, i is a generic index used for the species free water, bound water and dry fuel. In Table 3.1, A_i and the activation temperature, defined by $T_i = E_i/R$, are tabulated for three species.

Table 3.1: Thermokinetic parameters for solid fuel degradation

	A_i (s^{-1})	T_i (K)
Free water	5.13×10^{10}	$10,584$
Bound water	3.0×10^{13}	$18,000$
Pyrolysis gas	3.63×10^4	$7,250$

To model the pyrolysis process, by default, WFDS uses thermokinetic parameters available for pine needle combustion (shown in the table above) [34, 87]. The same constants are used for Douglas-fir needles here since the thermokinetic constant values are unknown for Douglas-fir needles. This seems to be a reasonable approximation given that both species belong to the *Pinaceae* family of species. A

39

similar approximation was also made by Mell et al. [69]. The thermokinetic constants of bound and free water used here were compiled from the works of Bryden et al. [13], Chan et al. [15], Prince and Fletcher [90], Yashwanth et al. [121]. It is noted that the species-specific thermokinetic constants for bound water was based on the experiments conducted on manzanita leaves with a suggested activation temperature of 20,000 K [90]. A sensitivity analysis on the activation temperature of bound water was performed and it was observed that changing the activation temperature by 10% resulted in less than 1% change in the results (such as peak mass loss rate and heat release rate). The energy equation for the fuel is:

$$\rho c_p \frac{dT_{\text{veg}}}{dt} = -\Delta h_{\text{vap}} \dot{m}'''_{\text{free}} - \Delta h_{\text{vap}} \dot{m}'''_{\text{bound}} - \Delta h_{\text{pyr}} \dot{m}'''_{\text{pyr}} - \nabla \cdot \mathbf{q}_c - \nabla \cdot \mathbf{q}_r, \qquad (3.2)$$

where the first three terms on the right hand side represent the energy release due to the evaporation of free and bound water, and release of pyrolysis gases, respectively. Here, Δh_{vap} represents the enthalpy of moisture vaporization set equal to 2259 kJ/kg [69], which is used for both free and bound water here, and Δh_{pyr} is the enthalpy of volatilization set equal to 418 kJ/kg [69]. In Equation 3.2, $\mathbf{q}_c$ and $\mathbf{q}_r$ denote convective and radiative heat fluxes, respectively, to the bulk of fuel.

The computational domain resembled the FIST apparatus displayed in figure 3.1 [65]. It consisted of a small wind tunnel, infrared heater, coiled wire ignitor and a high precision mass balance. The Douglas-fir needles were placed on a sample holder located on the mass balance and heated from above by an infrared heater producing

40
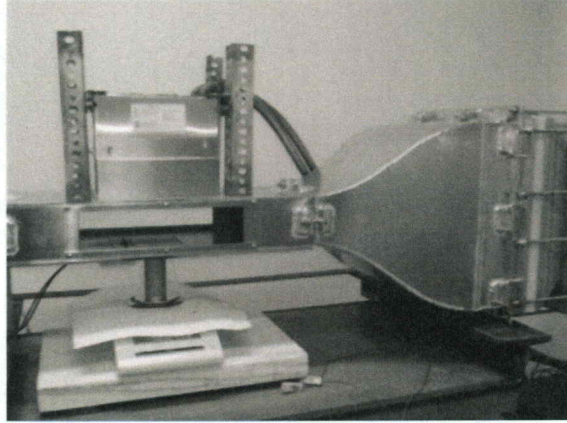
Figure 3.1: Forced ignition and flame spread test (FIST) apparatus used in McAllister et al. [65]

a uniform heat flux of 50 kW/m² at its surface. An airflow over the sample pushed the pyrolysis gases from the heated sample over an ignitor placed at a downstream location. In the experiments, since the radiant heater alone was insufficient to achieve ignition, the ignitor was held at a temperature above 1000°C, thereby heating the gas phase and initiating ignition. These values approximate the high heat fluxes associated with a wildfire.

Shown in figure 3.2 is the computational domain with dimensions $60 \times 28 \times 10.5$ cm (L $\times$ W $\times$ H) in x, y, and z directions, respectively. These dimensions were consistent with the actual dimensions of the midsection of the wind tunnel where experiments were carried out. The body of the wind tunnel used in the experiments, was made of aluminum 6160 and painted on the inside with high temperature flat black stove paint. The floor of the wind tunnel had a thickness of 3/8″ and a layer of mica of thickness 1/4″. Also, it was observed that the fire was located at a distance
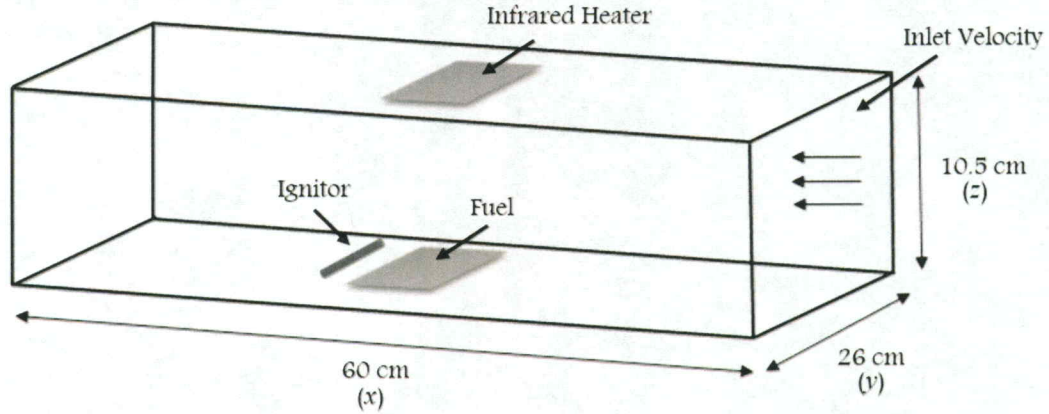
Figure 3.2: Computational domain of the wind tunnel setup used in the FIST apparatus. Fuel is uniformly distributed in a 9 cm×9 cm rectangular region.

close to 10 cm away from the walls of the wind tunnel. Considering the material properties, proximity of the fire to the walls and the occurrence of ignition in a time period of about 40 s, the walls were assumed to have minimal heating effect on the results. Hence, the walls of the wind tunnel were modeled to be inert and maintained at an ambient temperature of 293 K. A velocity inlet boundary condition at the right entrance of the wind tunnel established a laminar airflow with a velocity of 1 m/s and an open boundary condition was specified at the left exit. The Douglas-fir needles with an initial total mass of 4 g, were approximated as fixed, thermally-thin fuel elements with homogeneous composition and uniform distribution within a rectangular region with dimensions similar to the sample holder (9 cm in length and 9 cm in width) used in experiments. The vegetative dry and moist mass was also uniformly distributed among all fuel elements. The infrared heater was modeled as a 9 × 9 cm surface maintained at a temperature of 971 K, thereby producing a heat

42

flux of 50 kW/m^2 at the surface of the heater. A few non-reacting fuel particles held at a constant temperature of 1500°C modeled the ignitor, located at a distance 1.2 cm downstream of the fuel elements, centered 6 mm off the bottom. It is noted that McAllister et al. [65] mentioned the ignitor temperature was above 1000°C without giving an exact value for the ignitor temperature.

Ignition criteria is commonly defined as the time taken by the solid fuel to reach a specific ignition temperature. Based on experiments on live fuel burns [41, 101, 119] it is found that the ignition temperature for live fuels lies in the range 300-355°C. It is also noted that the ignition temperature varies with the fuel moisture content and is often dependent on the experimental setup. Here, we defined time to ignition as the time at which the global heat release rate reaches one half of its initial peak value. Since the peak value of heat release rate varies as a function of FMC, the ignition criteria varies with FMC as well. Based on the range of FMC observed over different seasons in the experiments, a range of 0% (dry fuel) and 70-130% was considered. Two types of model were considered for water: one assumed water at a free state only and the other included bound water in addition to free water. The initial mass distribution of free and bound water was determined by the FSP. Since the FSP of the investigated Douglas-fir needles were unknown, the FSP of wood, equivalent to 30% of FMC [94] is considered. Accordingly, for FMC ranging from 70-130%, the bound water mass decreased from 0.71 g to 0.52 g, while the initial free water mass increased from 0.95 g to 1.74 g. A total of nine simulations were performed. Four simulations considered FMC in the range of 70-130% for each water model type and one simulation with no moisture, representing dry fuel. A uniform grid size of 5 mm

was used in all simulations. In this work, LES is used to model turbulence wherein the filter size is the computational grid size. Hence, SGS terms, which are a function of the filter size, and subsequently the filtered gas phase equations which include SGS terms, change with the change in grid size [86]. So, a grid dependency study, as it is practiced in simulations of laminar flows or direct numerical simulations of turbulent flows, is inadequate. We have conducted the simulations with the highest possible resolution. Furthermore, to test the adequacy of the resolution, we used a criterion based on the characteristic flame diameter, D^*. Although this test was suggested for buoyant plumes, it was also used for wind tunnel scenarios and compartmental fires [80, 113]. For a uniform grid size Δx of 5 mm and for the range of moisture contents studied, the ratio of $D^*/\Delta x$ was found to vary in the range 13.2 to 16.0. It has been noted from previous studies [25, 80, 113] that this ratio must be in the range between 4 and 16 to obtain results adequate for engineering calculations. All simulations were performed for a burning time of 250 s, using 40 processors of the dense memory cluster at the Alabama Supercomputing Center.

3.3 Results and Discussions

Figure 3.3 shows the ignition time versus FMC. For all moisture contents, it was found that by including the effect of bound water, ignition occurred around 5 s prior to that observed in the cases where moisture was regarded as free water only. The ignition times obtained from the experiments had an uncertainty of about 2.5 s. For the free water only case, the simulated ignition times were found to lie within the observed uncertainty in experimental measurements for all moisture contents. For

44

the free and bound water case, at 70% FMC, there was a difference of around 5 s between the simulated and experimental ignition times (considering the uncertainty of 2.5 s). However, for higher moisture contents (to 130% FMC), this difference is lower and the simulated ignition times lie within the uncertainty of the experimental values. The reason for delayed ignition in the free water only case can be attributed to the fact that ignition was only observed after significant amount of moisture was released from the fuel at temperatures close to 100°C. Since, evaporation of water is an endothermic process, a significant increase in fuel temperature is inhibited during this process thereby delaying the process of volatilization and hence ignition. On the other hand, when the effect of bound water was included, a part of the moisture was released at temperatures close to 100°C and the rest was released only after the solid fuel attained temperatures close to 200°C. The process of volatilization began prior to the release time of bound water, thereby resulting in the release of pyrolysis gases and initiation of ignition relatively earlier. For dry fuel, the experimental and simulated time to ignition was 9 and 10 s, respectively. A linear regression was conducted on the experimental data displayed in figure 3.3 and the experimental data available for the dry fuel to find a correlation between the ignition time and FMC [65]. The regression equation was found to be $t_{ig} = 0.266 \times FMC + 8.83$ for the experimental data. A linear regression was also performed for the modeling data where moisture content was assumed to be in both free and bound water states, as shown in figure 3.3, and the modeling data for dry. The regression equation was $t_{ig} = 0.2185 \times FMC + 9.58$ for the modeling data. The slopes in these two correlations compared well with each other. The deviation between the simulated and experimental values could have two
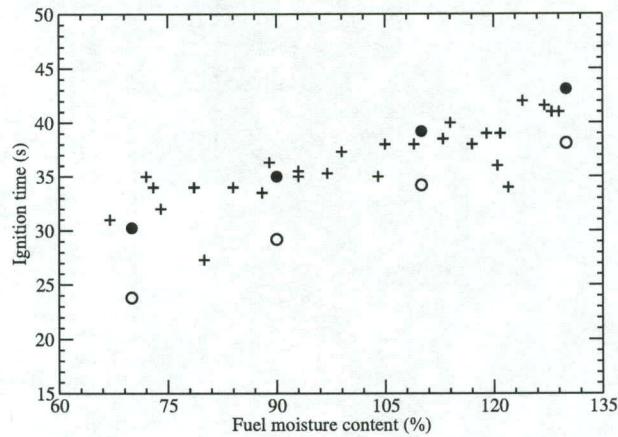
Figure 3.3: Variation of ignition time against fuel moisture content in experiments (+); modeling with FMC in the free only state (●); and modeling with FMC in the free and bound states (○).

reasons: 1) It was found in the experiments [65] that the fuels that were harvested at different seasons but had an identical FMC showed different ignition times; 2) It was also found in the experiments [65] that in addition to the process of evaporation, an explosive process of rupturing of the heated vegetation cell walls contributed to the release of moisture. As a result of this explosion, it was speculated that some of the volatiles were also released with water. In the modeling study, neither the effect of season nor the phenomena of explosion was taken into account.

Figure 3.4 shows the temporal evolution of the total fuel mass. The experiments were performed thrice every week during the growing season from March-October. Because of seasonal changes, the FMC was different each week. The experimental data in figure 3.4 and figure 3.5 was obtained by burning twelve samples, each

46

harvested in a different week, with FMC's ranging from 70 to 130%. The burning measurement of each sample was terminated soon after flaming ignition was observed in the gas phase. On the other hand, the simulations were performed until the fuel was completely burned. Depending on the initial fuel moisture content, the burning time varied from 150 to 200 s. It was observed in both experiments and simulations that the fuel mass loss was insignificant up to around 10 s. After this time, the temperature of the fuel element increased to values larger than the boiling point of water and the processes of evaporation and devolatilization became significant; hence, the mass dropped rapidly. At 200 s, the volatiles and moisture were completely released, leaving behind char which underwent oxidation. Comparing inset plots in figure 3.4(a) and (b) reveals that in the beginning, mass loss occurs slower in panel (b) than panel (a). This slower mass loss occurs because the free water evaporation is completed sooner in (a) than in (b), as there is more free water to be evaporated in the free water only case than in the free and bound water case. Overall, simulations compare better against experiments for the mass loss when water is treated in both free and bound states.

In figure 3.5, time histories of the total mass loss rate of the fuel for various FMC's are displayed. It was observed that the peak value of mass loss rate decreased with an increase in FMC. The peak mass loss rate for all moisture contents occurred well after ignition was observed, between times 30-50 s. The case with FMC of 70% had a maximum peak at 0.084 g/s.

In order to gain a better insight into evaporation of fuel moisture, mass loss rates of free and bound water are plotted against time in figure 3.6. As the temperature
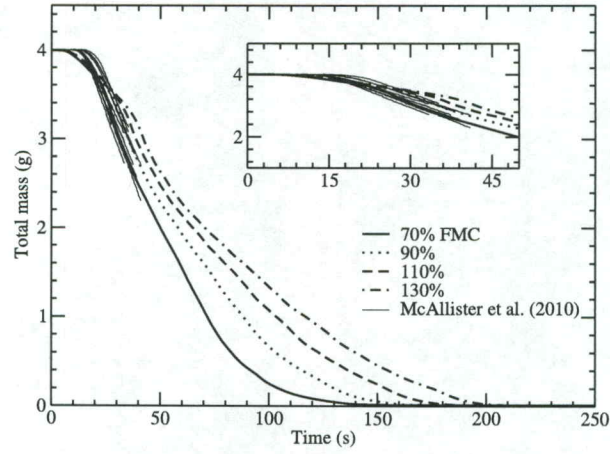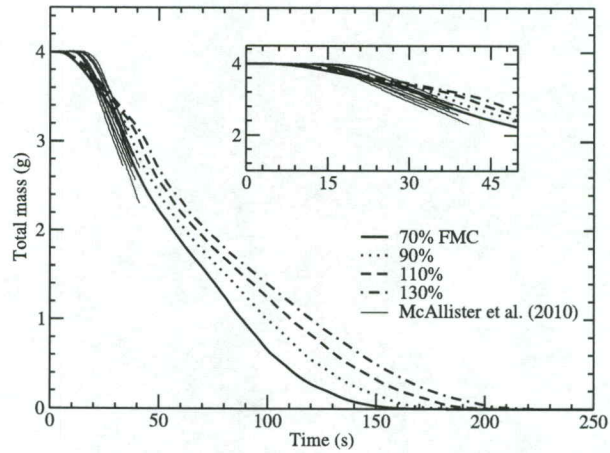
Figure 3.4: Variation of total mass of the fuel with time in modeling (lines) and experiments (symbols) for fuels with moisture content ranging from 70-130%; (a) free and bound water case; (b) free water only case. The inserted panel shows comparison between modeling and experimental data up to t=50 s.

48
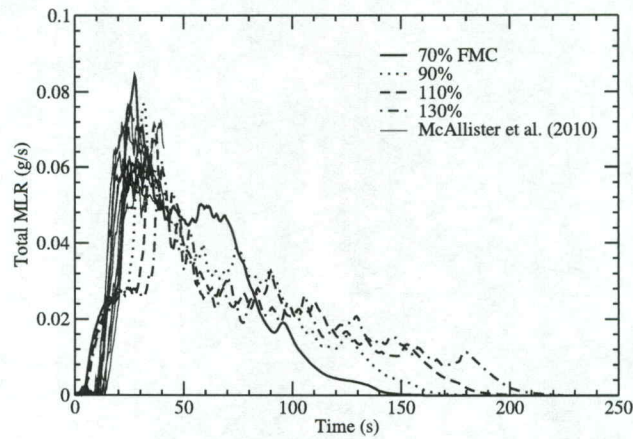
Figure 3.5: Variation of total mass loss rate with time in modeling (lines) and experiments (symbols) for fuels with moisture content ranging from 70-130%.

of the fuel element increased close to the boiling point of water, free water was first released. Figure 3.6(a) shows the peak mass loss rate of free water increased with an increase in moisture content and the maximum peak was observed for moisture content 130% at 0.0275 g/s occurring at time 28 s. Also it was observed that free water was completely released before 75 s in all cases. On the other hand, the initiation of bound water evaporation was observed at a later time around 15 s after free water evaporation was initialized. Here, the fuel elements attained temperatures greater than 200°C, also seen in figure 3.6(b). For all moisture contents, it was observed that the peak mass loss rate of bound water occurs close to the time of ignition. It is noted that bound water was released simultaneously with the fuel volatiles and the evaporation of bound water was completed almost 60 s after the evaporation of free water was completed. Also, for larger FMC's, the ratio of bound water mass to free

water mass is smaller given that the total mass of fuel is identical in all modeling cases. Hence, unlike free water, it was observed here that the peak mass loss rate of bound water decreased with an increase in moisture content. This peak occurred approximately 15 s after the peak mass loss rate of free water did. The peak MLRs of free and bound water are plotted against FMC in figure 3.7. For a moisture content of 70%, the peak mass loss rate of free water was larger than that of bound water approximately by a factor of 1.25. It almost linearly increased to 2.0 for FMC of 130%.

In figure 3.8, the variation of solid and gas phase temperatures with time is shown at a location close to the ignitor (1.2 cm upwind of the ignitor). The solid and gas phase at this location attained a maximum temperature of 600°C. For an FMC of 130%, it was observed that in the first 30 s, the temperature of the solid fuel increased up to 100°C. At this temperature, the evolution of free water was dominant, which is also evident from figure 3.6(a). After 30 s, with an increase in temperature (> 200°C), bound water and pyrolysates were released. To better understand the evaporation of free and bound water as function of temperature, figure 3.8 is plotted for the single fuel element located 1.2 cm upwind of the ignitor. From this figure, it was observed that at temperatures close to 200°C around 40 s, free water evaporation is completed and bound water evaporation was initiated.

The variation of heat release rate (HRR) with time is shown in figure 3.9. The peak value of HRR decreased with an increase in moisture content, owing to the fact that the dry mass of the fuel decreased with an increase in FMC. The case with 70% FMC had a peak HRR of 2.0 kW while the 130% FMC had a peak HRR of
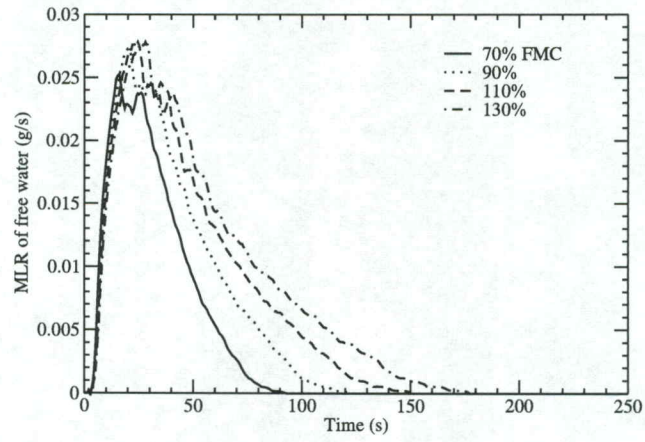
(a)
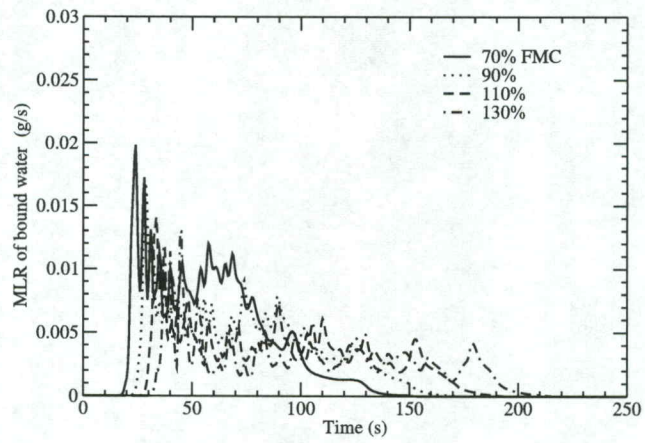
(b)

Figure 3.6: Variation of fuel moisture mass loss rate with time; (a) free water; (b) bound water.
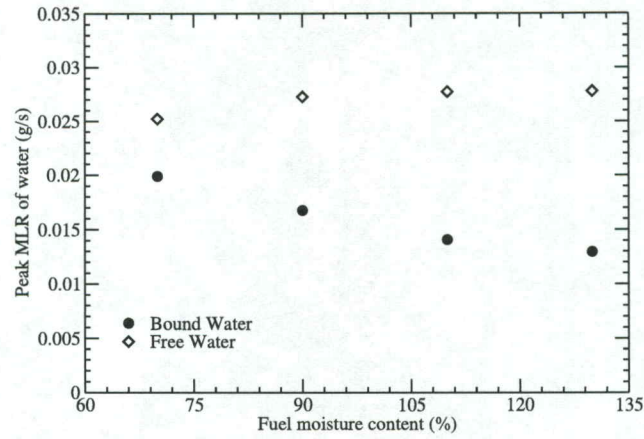
Figure 3.7: Variation of peak mass loss rate of free and bound water against fuel moisture content.
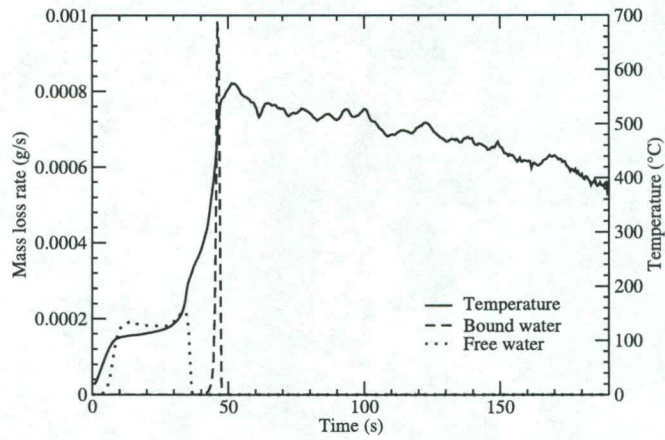
Figure 3.8: Temporal variation of mass loss rate of free and bound water along with the associated solid phase temperature for a fuel element located 1.2 cm upwind of the ignitor.
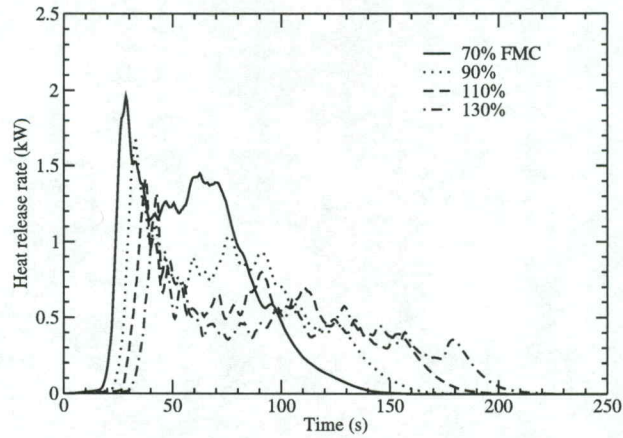
Figure 3.9: Variation of heat release rate with time for various fuel moisture contents.

1.3 kW. The ignition times, discussed earlier, were determined using the peak values of HRR. Also, the peak values were observed close to 5 s after the time instant at which ignition was defined.

In figure 3.10, distribution of gas phase temperatures on an xy slice plane located at $z = 0$ are shown at two different times 130 and 135 s for 130% FMC. The heat received from the radiant heater caused the fuel particles to release volatiles, which due to the effect of air flow, was convected over the ignitor located at the downstream location, thereby initiating gas-phase ignition. Hence, the fuel particles located close to the ignitor, were subjected to high temperatures and burnt faster than fuel elements away from it. As time progressed, the rest of the fuel elements burned in a pattern opposite to the direction of wind as observed in the case of a backing-like fire.

53
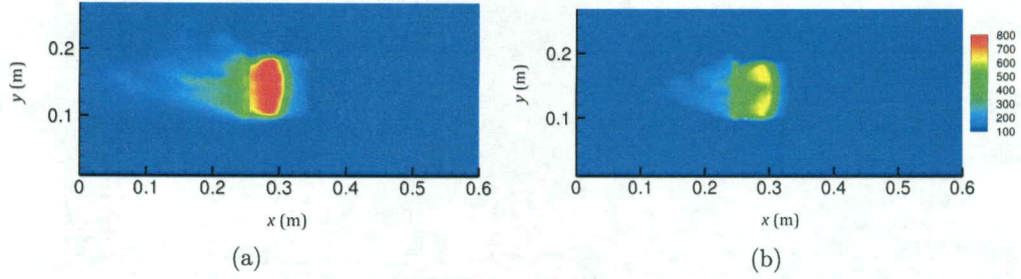
Figure 3.10: Temperature contours (in °C) of gas phase at a horizontal slice plane passed at $z = 0$ cm (top view) for fuel with 130% FMC at (a) $t = 130$ s; and (b) $t = 135$ s.

In figure 3.11, vertically oriented slice planes with contour plots of moisture mass fraction and gas phase temperatures are plotted at time 130 s for 130% FMC. At this time instant, which was well beyond the ignition and peak mass loss time instants, high mass fractions of moisture was observed at locations close to the solid fuel. The gas phase temperatures in this region were observed to be well above 800°C, thereby establishing the behavior of release of moisture in live fuels beyond the time to ignition.

3.4 Chapter Summary

A computational study was performed to improve our understanding of the ignitability condition of recipient fuels as relevant to the landing stage in the spotting mechanism. The live fuel ignition study was guided by the piloted ignition experiments on live Douglas-fir needles in the FIST apparatus [65]. A particle-based approach was used to model the burning of the needles wherein the particles were assumed thermally thin. The fuel moisture content was assumed to be in both free and
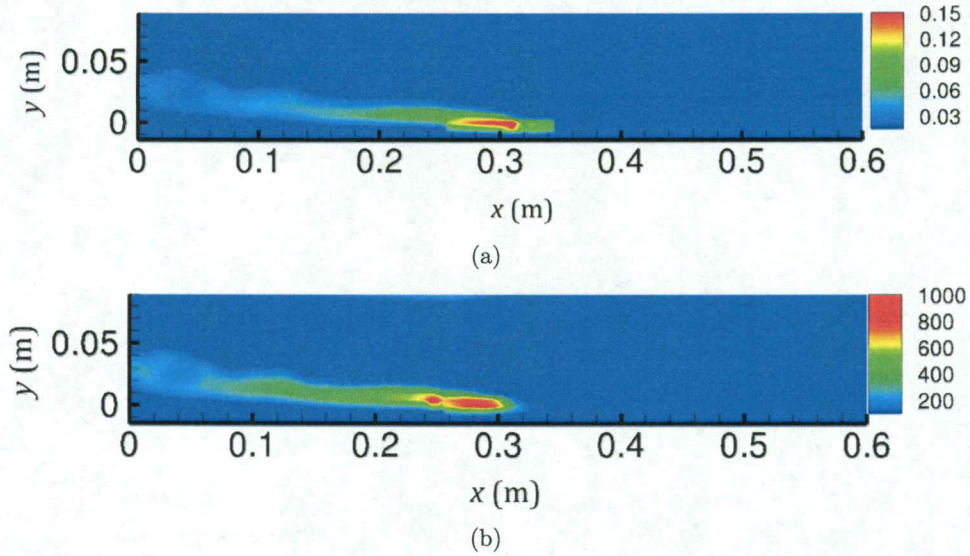
Figure 3.11: Color contours at a vertical slice plane passing through $y = 13$ cm (mid-section of the domain) at time instant $t = 130$ s for fuel with 130% FMC; (a) moisture mass fraction contours; and (b) gas phase temperature contours (in °C).

bound states. The evaporation of free and bound water was modeled by Arrhenius-type rate equations. Hence, the fuel was assumed to undergo a three-stage decomposition process, including evaporation of free water and bound water, pyrolysis and char oxidation. There was a difference of around 5 s between the simulated and experimental ignition times at FMC 70% when the bound water was accounted for in the simulation. However, for higher FMC, the simulated ignition times were within the uncertainty of the experimental values. This difference could be attributed to the seasonal effects on needles or evaporation of water by the rupture of cell walls observed in experiments. Neither effect was taken into account in simulations. The mass loss rates obtained by modeling were in a good agreement with those obtained by experiments. The relative error between the simulated and modeled maximum

peaks was within 5%. It was also observed that free water evaporated at temperatures close to boiling point of water whereas bound water and volatiles released later at temperatures close to 200°C. Simulations showed that significant amount of bound water remained in the fuel when ignition occurred.

CHAPTER 4

DISPERSION AND DEPOSITION OF FIREBRANDS IN A
TURBULENT BOUNDARY LAYER

4.1 Introduction

In this Chapter, results pertaining to the the dispersion and deposition of non-burning firebrands in a spatially developing TBL are presented. The firebrand equations discussed in Chapter 2 are solved for the motion of flying cylindrical firebrands. The recycling method, also described in detail in Chapter 2, is used to generate the TBL by LES. The main objective is to understand the turbulent dispersion of firebrands and its subsequent effects on the ground distribution of deposited firebrands. These results are most relevant to the landing stage of firebrands for intermediate or long-range spotting, as the primary fire or its influence on the carrier flow is not included in the simulations.

4.2 Computational Setup

To generate the TBL, a computational domain with physical dimensions of $250 \times 40 \times 75$ m is used in the x, y and z directions, respectively. A grid resolution of $420 \times 67 \times 90$ is used with the grid stretched polynomially in the z direction. The first

off-wall grid point is located such that it lies in the logarithmic region of the boundary layer ($y^+ \approx 1000$). The computational domain height used in this study corresponds to the atmospheric surface layer where the flow is insensitive to the earth's rotation [45]. In the current study, a TBL with a free stream wind velocity of 18.8 m/s was considered. This velocity corresponds to the average measured wind speeds in the event of real-fire scenarios (case study of New Jersey fires). Also, the Beaufort scale characterizes this wind speed to be of scale 8, where wind speeds are defined as gales (strong winds) at which possibility of twigs breaking off from trees are high. Initially the Spalding law profile [104] is imposed on the inlet with 10% turbulent intensity with a free stream velocity of 18.8 m/s and a boundary layer height of 25 m. As the flow develops, a realistic TBL was generated at the downstream location. Velocity components were then recycled from the recycle plane located at 80% of the length of the domain. At all times, the inlet boundary layer thickness was fixed to be 25 m. Once the TBL reached a statistically stationary state, firebrands were released continuously from a point at heights of 20 m and 40 m, at locations within and above the boundary layer respectively. In total, 40,000 firebrands were tracked for each case and the maximum volume fraction of the firebrand with respect to the computational cell size was of the order of 10^{-5}. These release heights correspond roughly to the heights to which firebrands of the size considered in our work are lofted in wildfires.

The dimensions pertaining to the firebrand length and diameter were based on the experiments of Manzello et al. [57] where real-scale fire experiments were performed by burning trees and the size distribution of firebrands collected from these experiments were reported. Most firebrands were cylindrical in shape with mean
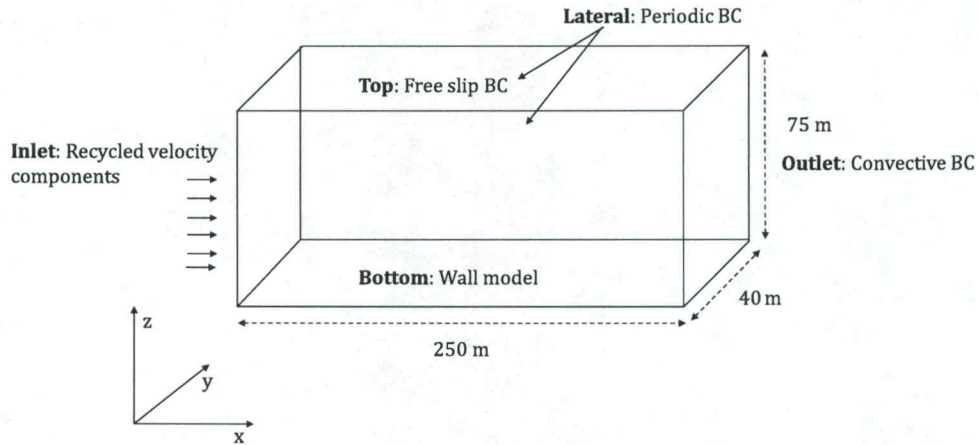
Figure 4.1: Computational domain used to generate the turbulent boundary layer along with the relevant boundary conditions.

length and diameter of 40 mm and 3 mm respectively. These mean dimensions have been used for all firebrands in the current study. The firebrand length (40 mm) is an order of magnitude smaller than the grid size. Three firebrand densities of 70 kg/m^3, 230 kg/m^3 and 570 kg/m^3 were investigated. These densities are representative of the wide range of firebrand densities observed in real fire scenarios. Here, 230 kg/m^3 is the actual measured firebrand density (of material cedar wood) in the Oaklands hill fire conflagration [81]. The lower and higher limits of density correspond to density of charred firebrand and the density of unburned firebrand (cedar wood) [92, 117] respectively. First, a test case was considered with the computational domain and Reynolds number equal to that studied in the work of Lund et al. [54]. Here, the computational domain had physical dimensions of $2.36 \times 0.37 \times 0.71$ m in the x, y and

z directions, respectively. A grid resolution of $100 \times 64 \times 45$ was used with the grid stretched polynomially in the z direction. The first off-wall grid point was located at $y^+ = 1$. The free stream velocity was 1 m/s and boundary layer height at the inlet was 0.22 m. After validating the recycling method with that of Lund et al. [54], the same method was then applied to the TBL with free stream velocity of 18.8 m/s. For the case with the lowest density firebrand released from 40 m height, the domain in the x direction was extended to 400 m.

4.3 Results and Discussions

First, a preliminary validation was performed for the presented dynamical model of the cylindrical firebrands against the experimental data of non-burning cylindrical firebrands released in quiescent air Oliveira et al. [78]. To simulate this experiment, firebrands with a density of 215.5 kg/m^3 (balsa wood) of length and radius 80 mm and 5 mm, respectively, were considered. The major axis of the firebrand had an initial orientation of 60° with the vertical axis and it was released from a height of 8.7 m with zero initial velocity. The initial conditions and the properties of the firebrands are consistent with that used in [78]. The path followed by the firebrand during its descent in the current study and that obtained from both numerical and experimental works of [78] are displayed in figure 4.2. In figure 4.2 (a), the firebrand position and orientation is shown at equal time intervals of 0.05 s from the time of release to the time of landing. The current results compare closely with both experimental as well as numerical results of [78] up to a height of 5.5 m. It should be noted that the experimental data are unavailable after the cylindrical firebrand

falls below ≈4 m. It took 2.08 s for simulated firebrands to land. This time was measured 1.8 s in the experiments and calculated 2.05 s in [78]. One reason for the discrepancy between simulations and experiments at later times could be attributed to the simplified dynamical model that is implemented for the cylindrical firebrand. Also, uncertainties in measurements may contribute to the observed difference.
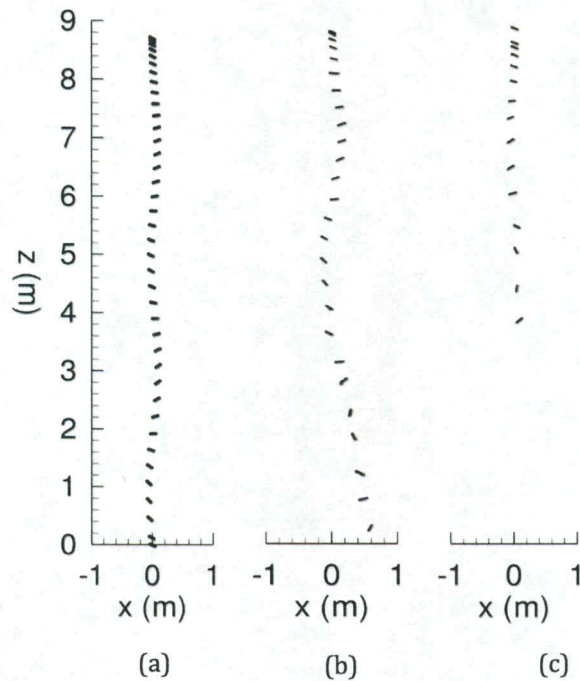
Figure 4.2: Snapshots of a cylindrical firebrand falling in quiescent air; (a) simulation (current work); (b) simulation of Oliveira et al. [78] and (c) experiment Oliveira et al. [78].

Now the results of the TBL study is discussed. In order to provide a pictorial overview of the flow field, contour plots of the instantaneous velocity magnitude within vertical planes in the computational domain are shown in figure 4.3. Also, the isosurface of Q-criterion and slice plane showing vorticity magnitude is illustrated in figure A.2 in the Appendix. At the inlet, the boundary layer height is 25 m with a free-stream velocity of 18.8 m/s. Two release points considered for firebrands are located very close to the inlet at heights of 20 m and 40 m at the midplane in the spanwise direction. One point was within the boundary layer and the other above it.

Figure 4.4 shows the mean flow velocity profile in the standard TBL coordinates, i.e., $u^+ = U/u_\tau$ versus $z^+ = z u_\tau / \nu$, where $u_\tau = \sqrt{\tau_w / \rho}$ and τ_w is the wall shear stress. Displayed in this figure are two sets of data of the current study: one for $Re_\theta = 10^3$, which was for a case initially used to test the recycling method, as illustrated in the previous section, without firebrands; and the other for $Re_\theta = 10^6$, which used the same method in a larger domain where firebrands were simulated. The definition of Re_θ is given in Chapter 2. The mean streamwise velocity at a downstream location was calculated by averaging in both time and the homogeneous direction, after statistically stationary state is reached. Also, included in figure 4.4 are the computational data of [39, 54, 91, 103] and experimental data of [22]. Good comparison is observed between the data obtained in the present work and the data available in literature for both the inner layer ($z^+ < 5$) as well as the log layer ($z^+ > 50$) of the TBL.
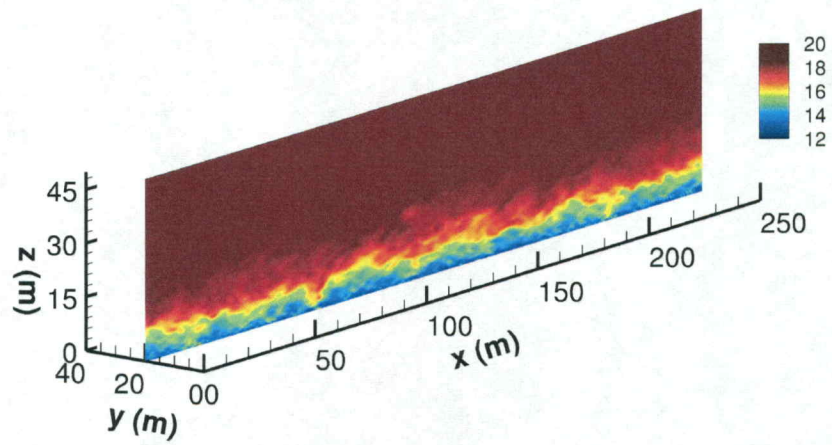
(a)
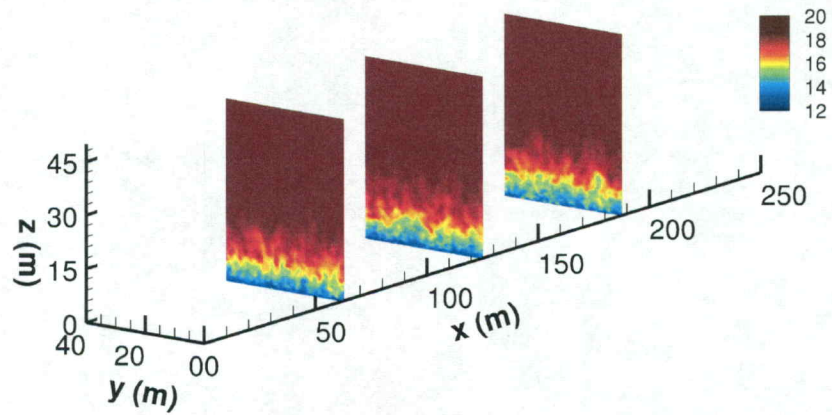
(b)

Figure 4.3: Instantaneous velocity magnitude on (a) the xz slice plane at the mid-section of domain (y=20 m) and (b) zy planes located at $x = 62.5, 125.0, 187.5$m.
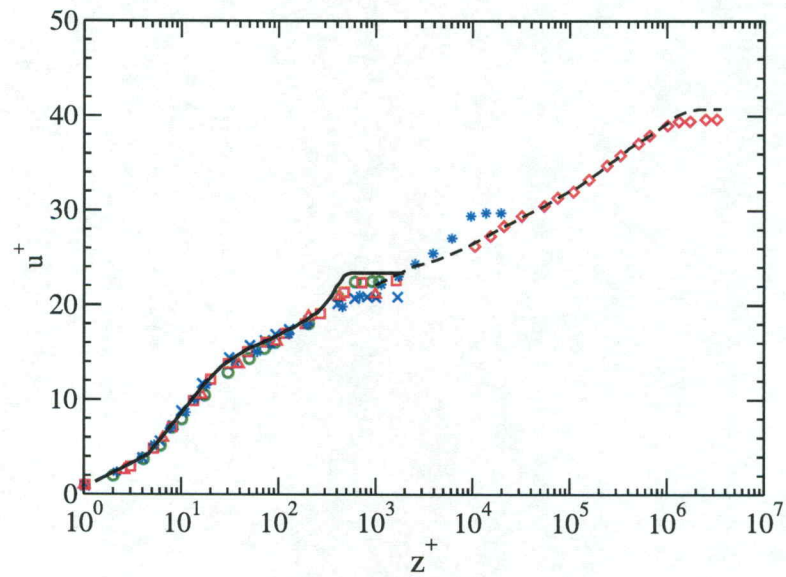
Figure 4.4: Normalized mean streamwise velocity of the flow plotted against the wall normal coordinate. Solid and dashed lines indicate the test cases with $Re_\theta = 10^3$ and 10^6, respectively. Symbols are the computational data of Inoue and Pullin [39] ◇, Wu and Moin [118] △, Lund et al. [54] □, Rai and Moin [91] ×, Spalart [103] ○; and experimental data of De Graaff and Eaton [22] ∗.
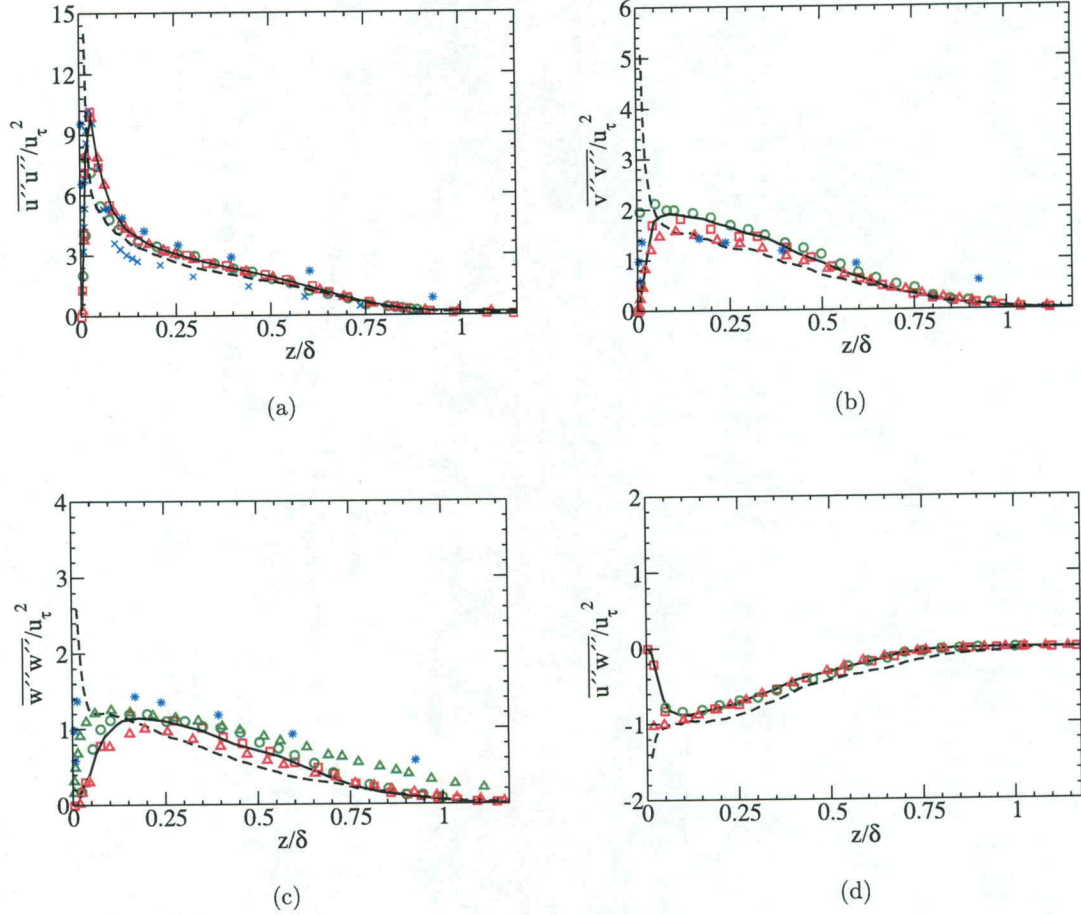
Figure 4.5: Square root of Reynolds stresses normalized by the shear velocity versus the wall coordinate normalized by boundary layer thickness. See the caption of figure 4.4 for the legend.

In figure 4.5 (a-d), the dimensionless Reynolds stresses are plotted against z/δ, where δ is the boundary layer thickness. Also, for comparison, the data available in literature (symbols) are plotted using the same notation as in figure 4.4. The Reynolds stresses are normalized by the friction velocity in this figure. For the simulated case of $Re_\theta = 10^3$, the boundary layer was resolved up to $z^+ = 1$, which is the region close to

the wall. A good agreement between this case and the data available in the literature is seen in this region. On the other hand, for the simulated case of $Re_\theta = 10^6$, which uses a significantly coarser grid as the Werner-Wengle wall model was applied, the first off-wall cell lies in the logarithmic region of the boundary layer. The sharp rise observed in panels (a-c) for this case in the inner region very close to the wall, which is in disagreement with other cases, is because the wall model provides only an estimate of the velocity components in this region. However, comparison away from the wall is very good.

In the rest of this section, statistics pertaining to the firebrand positions and velocities are presented and discussed for three firebrand densities and two release heights. A statistical approach is essential in characterizing the behavior of firebrands carried in turbulent flows, as the trajectories of individual firebrands are distinct although released under identical initial conditions. This distinction is attributed to the uniqueness of the sequence of the flow velocities that each firebrand samples from release to landing in turbulence, and is manifested by the uniqueness of the landing location of the firebrand, as evident from the results to be presented. The statistical quantity associated with each curve in the following figures are calculated using an ensemble of flying (suspended) firebrands released from the same point. On the other hand, the time that each firebrand takes to land is different. The curve is displayed until the time right before the first firebrand in the ensemble lands.
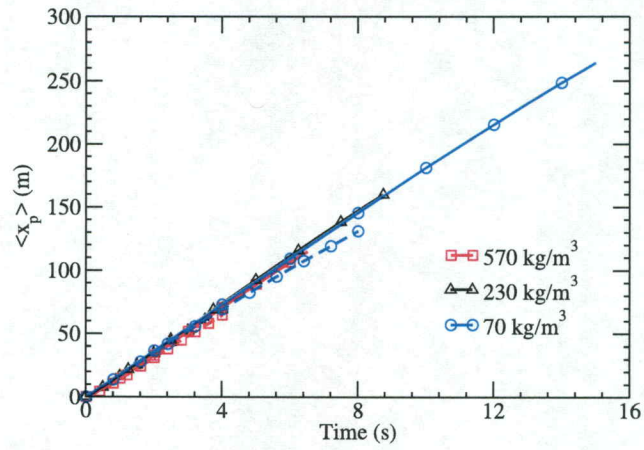
(a)
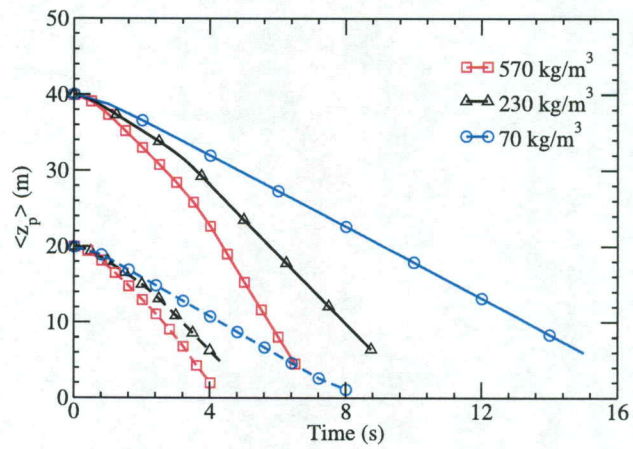
(b)

Figure 4.6: Temporal variation of the mean (a) spanwise and (b) vertical components of firebrand positions for release heights of 20 m (dashed lines) and 40 m (solid lines).

In figure 4.6, the time evolution of the streamwise and vertical components of the mean firebrand position, $\langle x_p \rangle$ and $\langle z_p \rangle$, respectively, is displayed for all simulated

cases. As seen in figure 4.6(a), $\langle x_p \rangle$ exhibits an almost linear functionality with time. The streamwise firebrand position is largely determined by the streamwise component of carrying flow velocity. Since the mean of this component does not vary significantly in the streamwise direction, the streamwise firebrand position varies almost linearly. On the other hand, in the vertical direction, the terminal velocities attained by firebrands are largely a function of firebrand densities. Thereby, the effect of density on the mean position and dispersion is largely seen on the vertical direction. The firebrands with the lowest density of 70 kg/m³ which were released from a height of 40 m travelled the longest distance ($\sim$ 275 m) while the ones with the highest density which were released from a lower height of 20 m, travelled the shortest distance ($\sim$ 75 m). For firebrands with identical densities, the ones released from the height of 40 m, take approximately twice the time to reach the ground as compared with the ones released from the height of 20 m. As evident in figure 4.6(b), the gravitational force acting on larger density firebrands is more dominant so they descend faster than lower density firebrands. Also, the mean elevation of firebrands almost linearly decreased with time for the lowest density firebrands. For completeness, the scatter plots showing all firebrand paths for initial density of 230 kg/m³ and release heights of 20 m and 40 m are illustrated in figures A.3 and A.4 in the Appendix.

The time variation of the streamwise and vertical components of the mean firebrand velocity is shown in figure 4.7. The mean firebrand velocity in the spanwise direction is calculated to be negligible so it is not displayed in this figure. As can be seen in figure 4.7(a), the mean streamwise velocities of firebrands increase very rapidly to values close to the local flow velocity, which is in the range 17-18.8 m/s

68
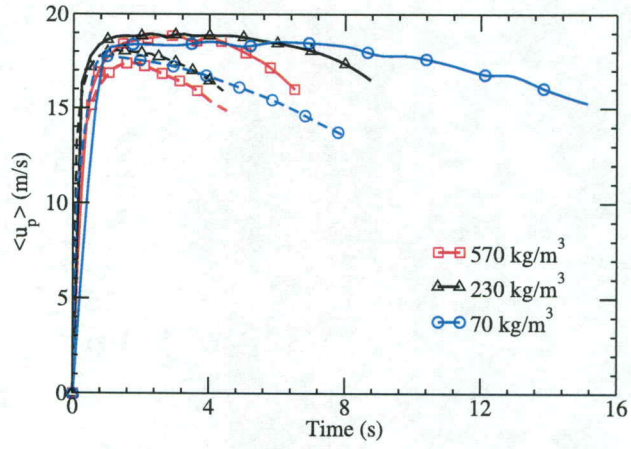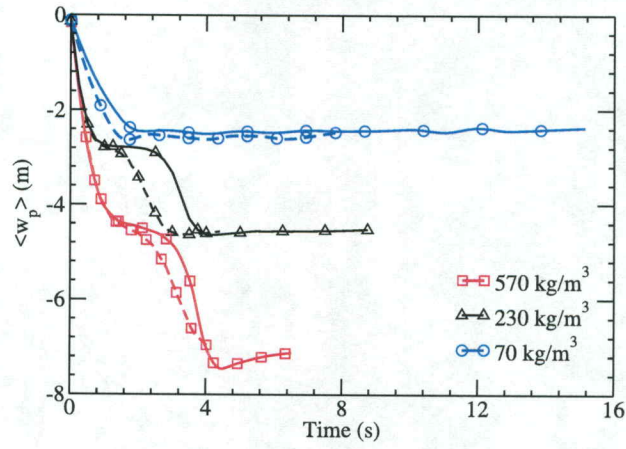
Figure 4.7: Temporal evolution of the mean (a) streamwise and (b) vertical components of the firebrands velocities for release heights of 20 m (dashed lines) and 40 m (solid lines)

69

depending on their release heights. This increase is because of an initial large magnitude of the drag and lift forces, as the relative velocities between the firebrands and their local flows are initially large (see Equation 2.4 and Equation 2.5). The gravitational forces in the vertical direction are dominant, as evident by the negativity of $\langle w_p \rangle$ in figure 4.7(b), resulting in the descent of the firebrands. In a boundary layer, since the mean streamwise flow velocities decrease with a reduction in elevation, in the average sense, the drag forces in the streamwise direction decrease while firebrands descend. This is the reason for the decrease of $\langle u_p \rangle$ after the initial times, as seen in figure 4.7(a). It is seen in figure 4.7(b) that $\langle w_p \rangle$ becomes almost constant prior to the firebrands reaching the ground. This constant value can be regarded as the mean terminal velocity. At the terminal velocity, the forces due to drag and lift are balanced by the force of gravity in the vertical direction so the acceleration of the firebrand is zero. Initially the firebrands have no oscillations upon release. As they begin to descend, the firebrands begin to oscillate about the 90° angle, which is also a stable equilibrium point for falling cylindrical rigid bodies [78, 123]. Once the aerodynamic forces balance the gravitational force, the firebrands attain the terminal velocity and the oscillations are damped out as they fall stably at the 90° angle. Firebrands with lower densities have shorter time response and hence the oscillations damp out quickly. On the other hand, firebrands with higher densities with longer response times oscillate for a longer period of time and hence the first plateau is observed. However, at later times when the forces balance each other, $\langle w_p \rangle$ asymptotes towards the terminal velocity.

It is observed that firebrands with same densities released from different heights reach the same mean terminal velocity. The firebrands with the least density of 70 kg/m^3 reach a mean terminal velocity of 2.5 m/s in a time period of 2 s, while firebrands with the highest density of 570 kg/m^3 reach a mean terminal velocity close to 7.8 m/s in a time period of 4 s. Based on the wind tunnel experiments, Tarifa et al. [107] proposed the terminal velocity assumption wherein firebrands were assumed to travel at their terminal velocity at all times. This assumption has also been widely used to track the motion of firebrands [2, 36]. However, the terminal velocity approximation may be applicable for simplified wind and plume models [49] and is not suitable for turbulent flows. Such flows have an effect of modulating the velocity of the firebrand, thereby inhibiting the firebrands from achieving the terminal velocity at all times. As evident in the figure 4.7(b), it must be emphasized that depending on the density and the background wind, a time delay exists in achieving the terminal velocity. Thus the terminal velocity approximation would incorrectly predict the position of firebrands and will not hold for the scenarios described in the current work.

To help in understanding the extent of spatial dispersion of firebrands in various directions, the dispersion tensor defined by $\langle x'_{\mathrm{p},i}(t) x'_{\mathrm{p},j}(t) \rangle$, where $x'_{\mathrm{p},j}(t) = x_{\mathrm{p},j}(t) - \langle x_{\mathrm{p},j}(t) \rangle$, is calculated. The temporal evolution of firebrand dispersion is displayed in figure 4.8 and figure 4.9. For all the cases, it is seen that the dispersion is zero at the release time and increases over time. This zero initial value is attributed to the release of firebrands from a fixed point in every simulation. For the cases with release height of 40 m, since the release point is in the outer layer and the flow is laminar

71

in this layer, firebrands descend initially without experiencing turbulence. Hence, dispersion for the first few seconds do not gain an appreciable value until firebrands enter the boundary layer which is turbulent.

On the other hand, the initial time for dispersion to gain an appreciable value is shorter in the cases where the release point is at 20 m above the ground, which is in the TBL. For both release height cases, it is seen that the dispersion of firebrands is higher for lower firebrand density since it has less inertia. Dispersion in the streamwise direction is found to be larger than the other components. This is because, as evident from figure 4.5, the magnitude of the Reynolds stress for the carrying phase is the largest in the streamwise direction. Hence, the turbulent fluctuations in the background flow has an effect of dispersing the firebrands more significantly in this direction. Also, from figure 4.5, the magnitude of Reynolds stresses in the spanwise direction is greater than the vertical component. However for the firebrands, as shown in figure 4.8 it is observed that the vertical component of dispersion is greater than the spanwise component. This behavior is observed because, in the vertical direction, since the densities of the firebrands are much larger than the density of the carrier flow, the gravitational force acting on the firebrand is dominant in comparison to the forces acting on the firebrand in the spanwise direction. For the same reason, the lighter firebrands for both the release height cases disperse laterally more than the heavier firebrands. Hence, the overall effect of the TBL on the firebrands is to cause significant dispersion in the streamwise direction. In figure 4.9 the variation of the most significant off-diagonal dispersion component is shown. Figure 4.9 does not include a panel for $\langle x'_p y'_p \rangle$ and $\langle y'_p z'_p \rangle$ as these dispersion components remain very close

72

Figure 4.8: Temporal evolution of turbulent dispersion of firebrand in the streamwise (top row), spanwise (midde row) and vertical direction (bottom row) for firebrands released from a height of 20 m (left panels) and 40 m (right panels).

Figure 4.9: Temporal evolution of variation of the off-diagonal turbulent dispersion component. Firebrands released from 20 m and 40 m height are shown on the left and right panels respectively.

to zero at all times in the simulations. The negligible value of the off-diagonal dispersion components of the firebrands is attributed to the less dominant shear stresses of the carrier flow field calculated as a function of the spanwise direction. However, the quantity, $\langle x'_p z'_p \rangle$ is significant owing to the larger fluctuations in the streamwise and vertical components of velocity.

The rate at which firebrands are spatially deposited is crucial to understanding the phenomena of rate of fire spread which in turn is a function of firebrand release height, density and ambient wind speed. In figure 4.10 and figure 4.11, the turbulent diffusivity of firebrands [11, 18, 108] defined by

$$D_{ij}(t) = \frac{1}{2} \frac{d \langle x'_{p,i}(t) x'_{p,j}(t) \rangle}{dt}, \tag{4.1}$$

is plotted against time. The diffusivity tensor, indicates the rate at which firebrands are spatially dispersed. In the work of [108], it was demonstrated that, when gravitational effects on particles are neglected, the diffusivity of particles correlates with that of the carrier flow. It was also emphasized in several works [6, 20, 44, 93, 102] that the turbulent fluctuations in the carrier flow can significantly impact the diffusion of particles with low inertia. In the current study however, the density of firebrands is much greater than the density of the air/carrier flow. Since the high inertia firebrands rapidly descend and encounter different fluid regions, their diffusion is not well correlated with that of the carrier flow. It is found that the diffusivity of the firebrands in the streamwise and the spanwise directions increases with time for all the cases. This is due to the increased turbulent fluctuations encountered within the TBL. For a given release height, the firebrands with the least density have larger variances and hence are more diffusive. In both spanwise and streamwise directions, the diffusivity of firebrands having the least density is almost twice as that of the firebrands with the highest density at times close to deposition on the ground. However, in the vertical direction, the diffusivity of firebrands peaks and then plateaus at the time of deposition. This behavior is observed because the firebrands descend through the TBL where turbulent fluctuations affect its motion and increase its diffusivity. With further increase in time, the gravitational force acting on the firebrand balances the aerodynamic forces and the acceleration of the firebrands tend to zero, hence decreasing its diffusivity. This decrease in diffusivity at terminal/asymptotic velocities is also discussed by [20] in the context of turbulent diffusion of heavy particles.

The off-diagonal component shown in figure 4.11 is representative of the rate of change of correlations of the fluctuation in displacements. Here, similar to dispersion, among all off-diagonal diffusivity components D_{xz} had a significant value. Since the fluctuations in spanwise displacements is small, the other components D_{xy} and D_{yz} remained close to zero. Overall, in figure 4.8-figure 4.11, the statistical quantities relating to firebrands such as turbulent dispersion and diffusivity are presented. From these statistics, the impact of the flow turbulence for varying firebrand densities is understood. While the dispersion tensor helps to understand the extent to which firebrands are dispersed in various directions, the turbulent diffusivity tensor provides further information regarding the rate at which firebrands are spatially dispersed. It is seen that these quantities are largely a function of the firebrand release height and density.

Firebrand velocity variances are shown in figure 4.12. It is seen that they are zero at the beginning, which is attributed to the release of firebrands with zero velocities. After the release, the variances increase for the 20 m height cases whereas they remain very close to zero for the first few seconds and then increase for the 40 m ones. The reason for this difference is illustrated here. The 20 m height release point is located within the TBL whereas the 40 m one is above it. The flow above the boundary layer is laminar, as evident by vanishing Reynolds stresses for large z^+'s in figure 4.5. Thus, the firebrands released from the 40 m height point do not encounter turbulence until they enter the boundary layer. As a result, they possess identical velocities at identical times during their flight from the release point to where they enter the boundary layer. Hence, the firebrand velocity variances are zero and their trajectories
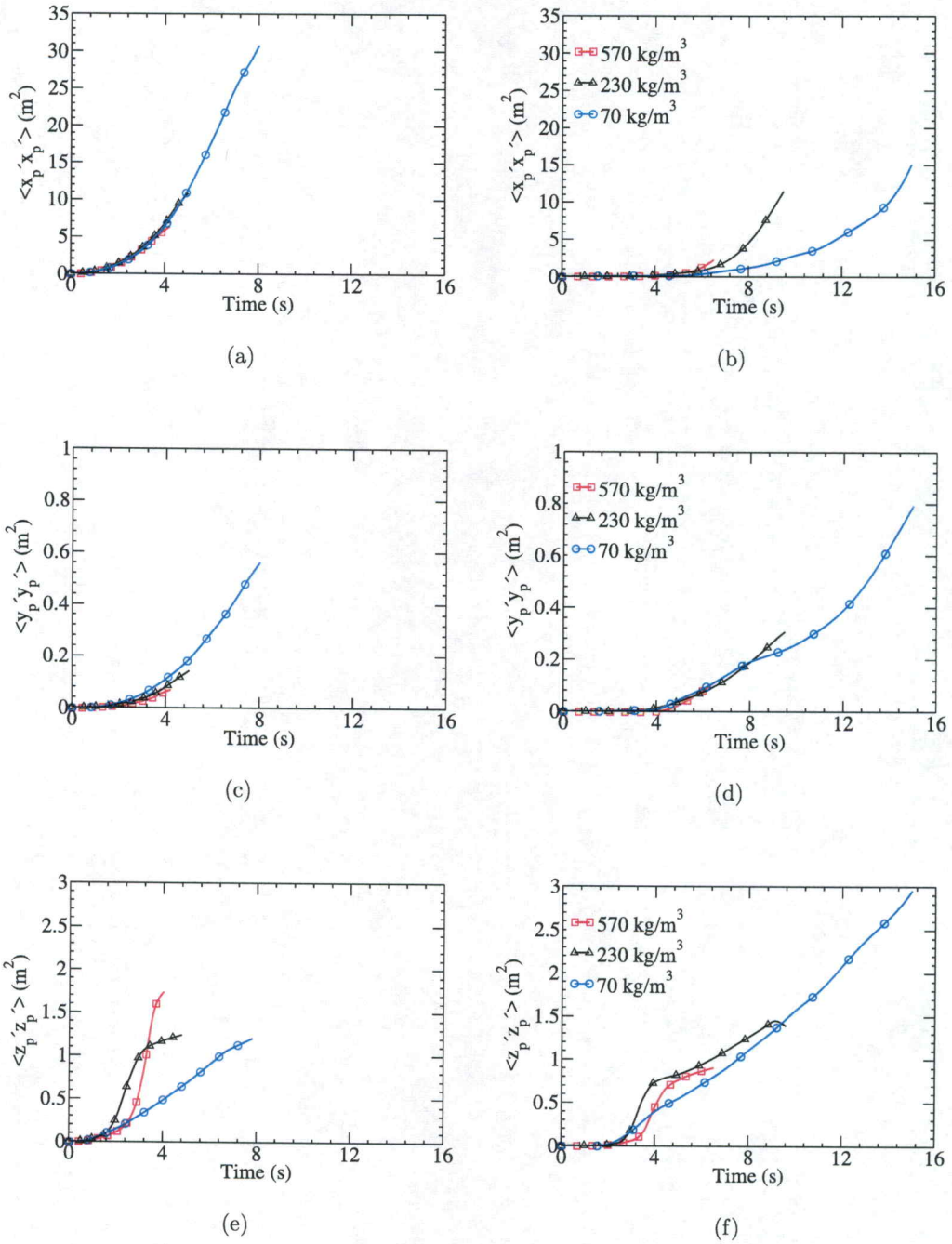
76
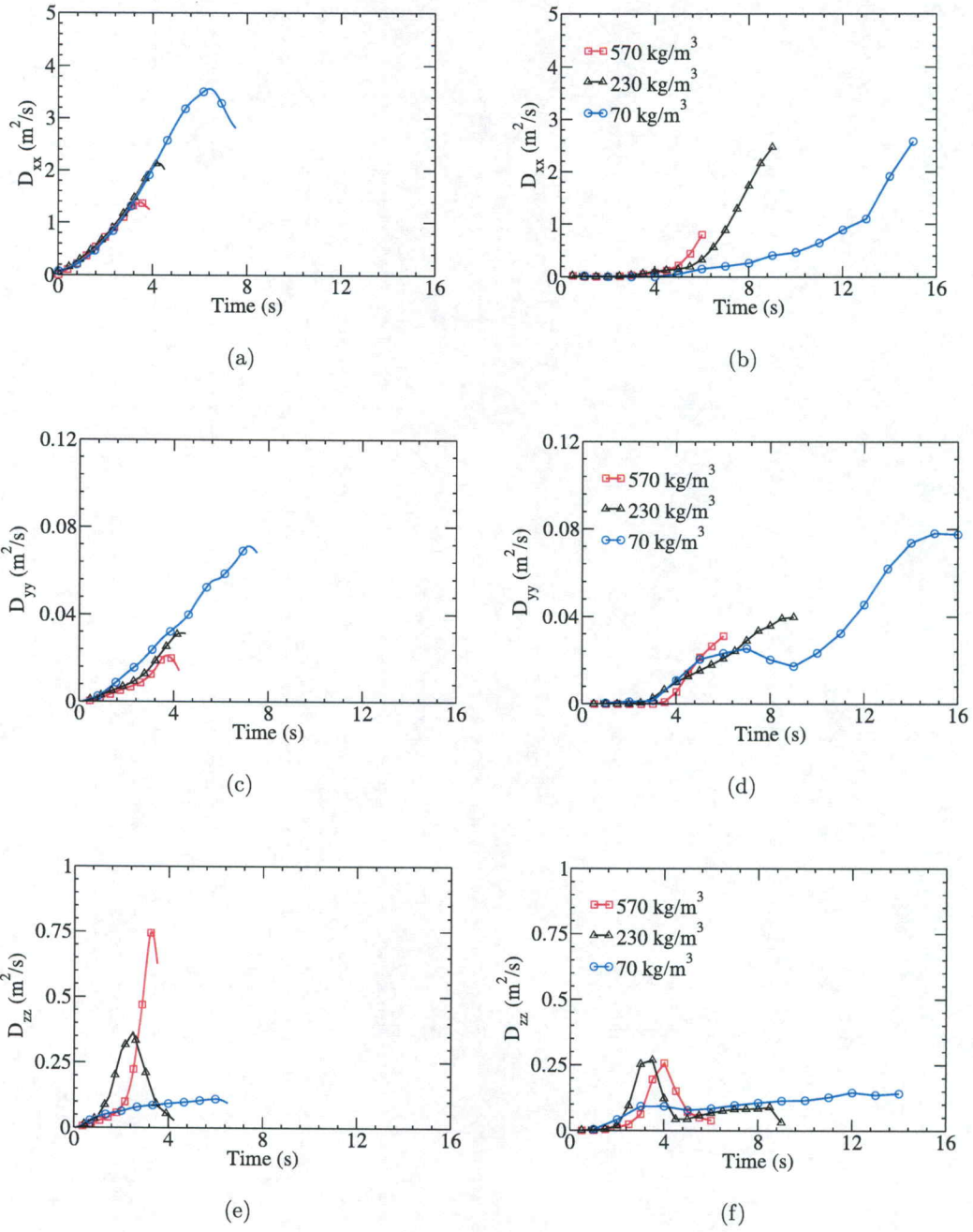
Figure 4.10: Temporal evolution of turbulent diffusivity components of firebrands in streamwise (top row), spanwise (middle row) and vertical (bottom row) directions for the release height of 20 m (left panels) and 40 m (right panels).

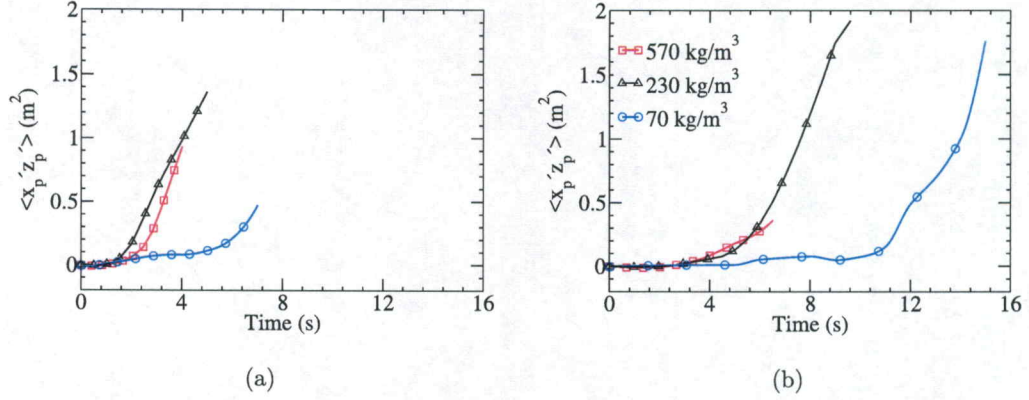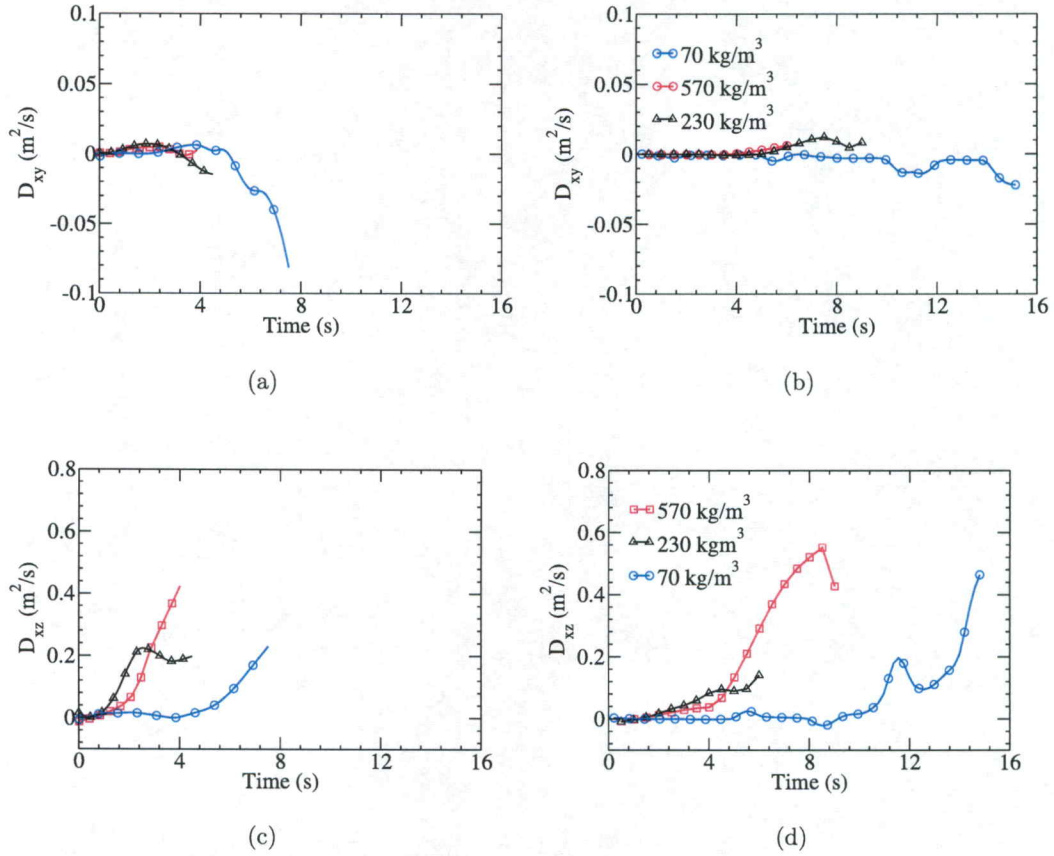**Figure 4.11**: Time evolution of the off-diagonal components of the turbulent diffusivity for a release height of 20 m (left panels) and 40 m (right panels).

are identical while outside of the boundary layer. As could be seen in figure 4.12, the variance of the firebrand velocity in the spanwise direction is the least among all directions for a given density and release height. A unique noticeable aspect is with panels (e) and (f) in figure 4.12. That is a sharp peak in the variance of the velocity in the vertical direction for two largest densities. This peak is a result of the competition between the hydrodynamic force, viz., the combined drag and lift forces, and the body force, viz. the combined gravitational and buoyancy forces. While

the former is under the influence of turbulence, the latter is not. Starting with zero values, vertical velocity variances grow because of the turbulence in the flow. On the other hand, as time progresses, firebrands gain a mean terminal velocity as the projection of the hydrodynamic force in the vertical direction balances with the body force in the average sense. The vertical velocities of heavier firebrands deviate slightly from the mean terminal velocity (see figure 4.7(b)).

Figure 4.13 displays the covariance of the firebrand velocities $\langle u_p' w_p' \rangle$ vs time. The other co-variances are not shown, as they do not have appreciable values. For the firebrands released at the 20 m height, the covariance $\langle u_p' w_p' \rangle$, increases upto the time at which the terminal velocity is attained. However, at later times, $\langle u_p' w_p' \rangle$ tends to a negative value and varies similar to the shear stress of the carrier flow, which is displayed in figure 4.5. In case of the firebrands released outside the boundary layer, the initial peak in $\langle u_p' w_p' \rangle$ is less pronounced as the firebrands reach their terminal velocity just before entering the turbulent region. Hence, at early times the covariance is close to zero as the firebrands descend through the free-stream region and later becomes negative due to the shear stress of the carrying flow.

The likelihood of ignition by spotting will be higher if a large number of deposited firebrands are accumulated in close proximity of each other. Thus, characterization of the pattern of deposition of firebrand will help to delineate areas prone to spotting ignition. The number density of the deposited firebrands, defined as the number of firebrands deposited per unit area, is a variable that can be calculated to quantify the particle accumulation. On the other hand, it can be shown that the number density is proportional to the probability distribution function (PDF) of the streamwise and
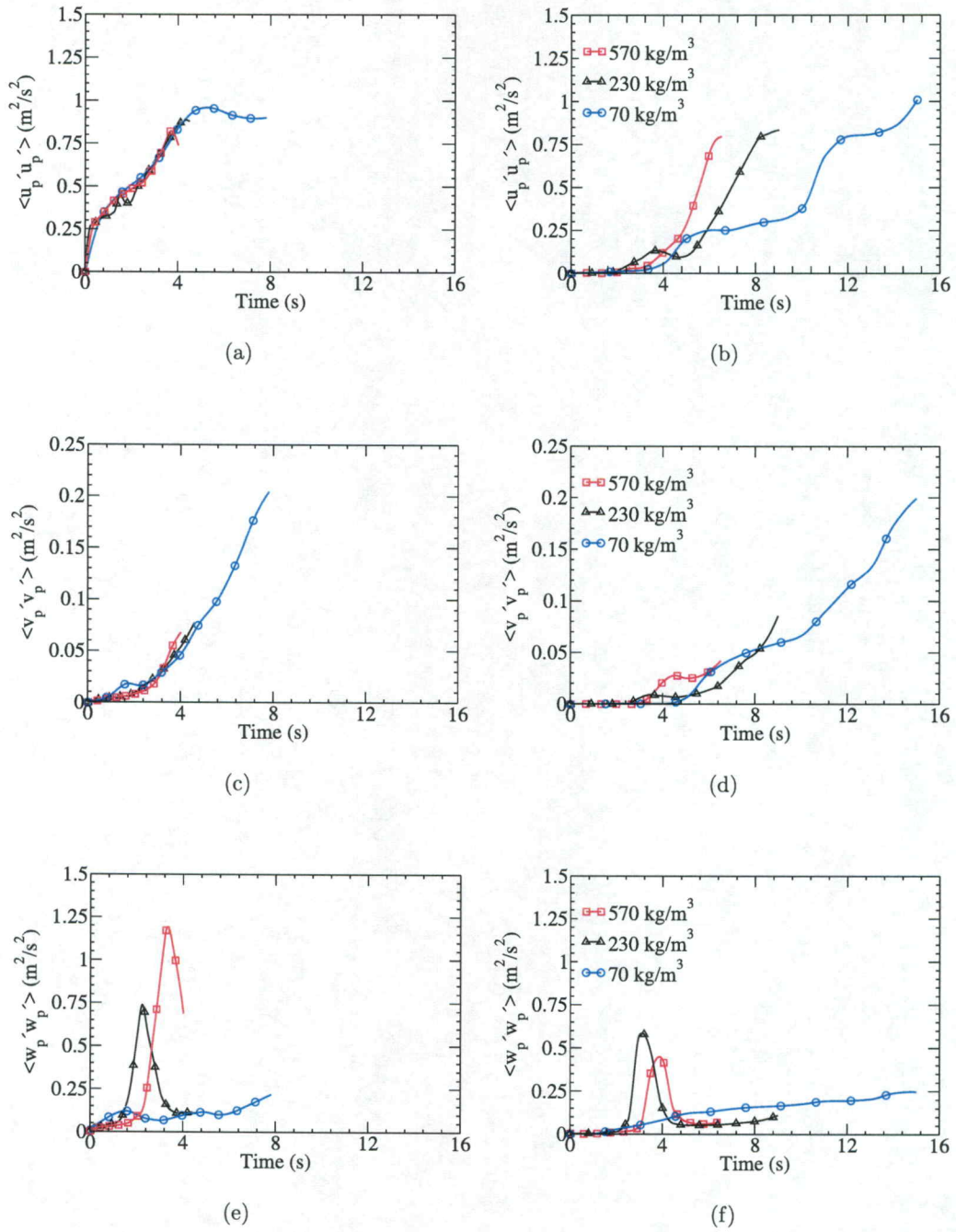
Figure 4.12: Temporal evolution of the variances of the firebrand velocities for the release heights of 20 m (left panels) and 40 m (right panels).
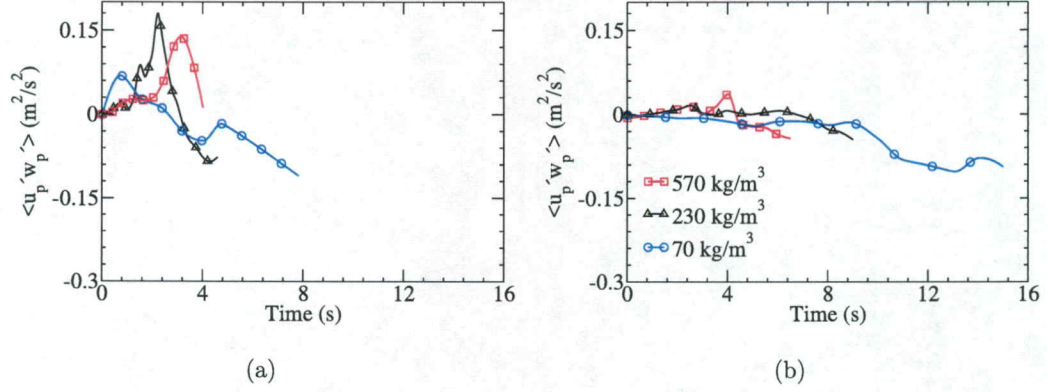
Figure 4.13: Time evolution of the co-variances of firebrand velocities for the release heights of 20 m (left panels) and 40 m (right panels).

spanwise coordinates of the deposited firebrands. In figure 4.14, the contour plots of this function are displayed (x and y axes do not use the same scale). If f indicate this PDF, it is calculated by:

$$f(x,y) = \frac{1}{nh^2} \sum_{p=1}^{n} K\left(\frac{x - x_{\mathrm{p}}}{h}, \frac{y - y_{\mathrm{p}}}{h}\right) \tag{4.2}$$

where, h is the bandwidth parameter, n is the total number of the deposited firebrands and $K(x,y)$ is called the smoothing kernel, which is calculated by $K(x,y) = K(x) \cdot K(y)$ in the current work, where $K(x)$ is a standard normal distribution. Also, x_{p} and y_{p} are the coordinates of a deposited firebrand in the streamwise and spanwise directions, respectively. It is noted with the given definition, $f(x,y)$ satisfies the normalization condition, meaning that its integration over the area is unity. Here, f also indicates the probability density function of the landing coordinates of a released firebrand.

81
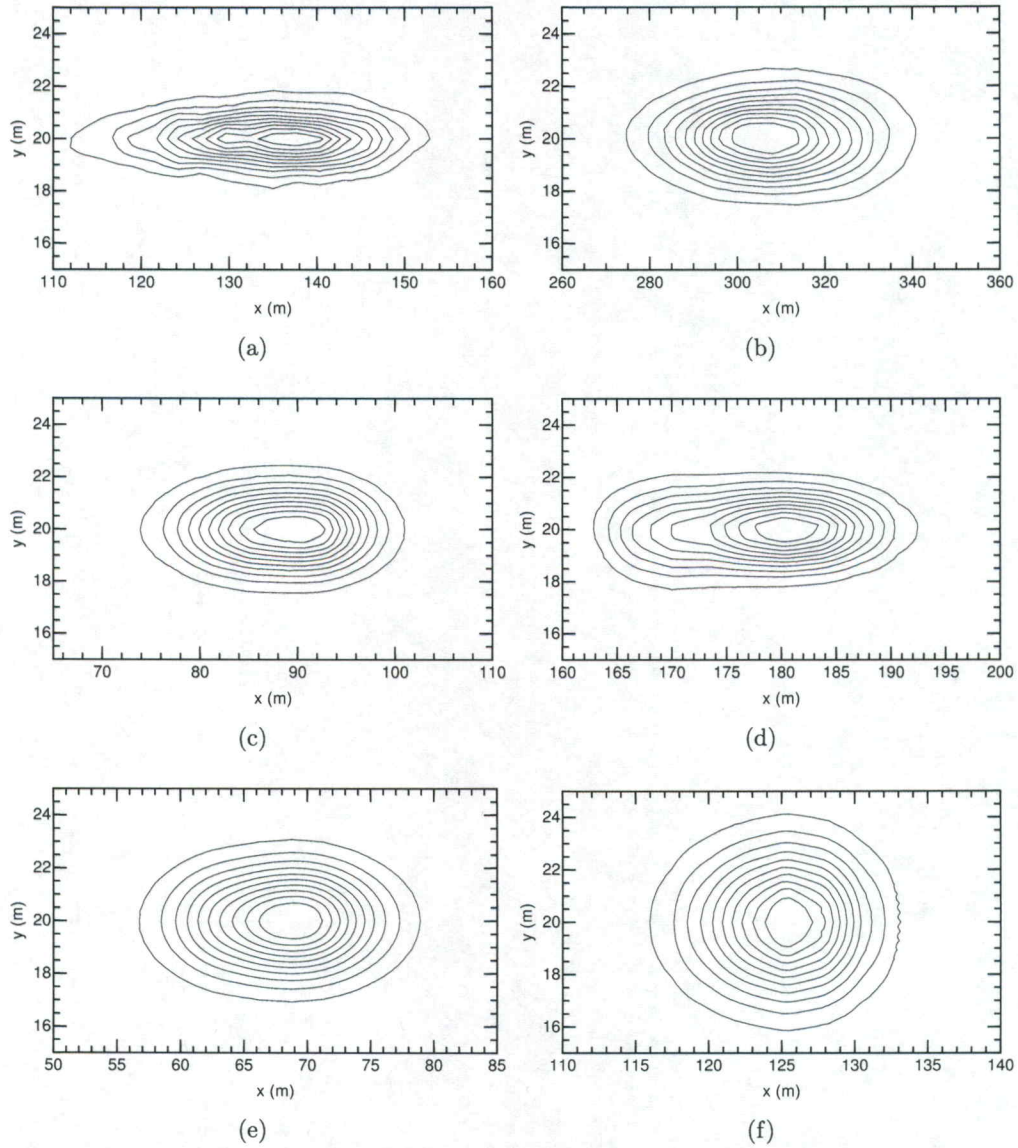
Figure 4.14: Contour plots of the probability distribution of deposited firebrands for the release height = 20 m (left column) and 40 m (right column) for $\rho_p = 70$ kg/m^3 (top row), 230 kg/m^3 (middle row) and 570 kg/m^3 (bottom row). The innermost contourline has a maximum value of 0.02 and the outermost has a minimum value of 0.002.

In figure 4.14, the contour lines of the PDF of the deposited firebrands are displayed. In each panel of figure 4.14, the innermost contour line indicates the region with the highest probability of deposition.The contour lines resemble ellipses with minor and major axes in the spanwise and streamwise directions, respectively. This appearance is an indication of a larger dispersion in the streamwise direction than in the spanwise direction. The streamwise distribution of the firebrands with the lowest density 70 kg/m^3 and the release height of 40 m is almost 1.6 times greater than the release height at 20 m. This factor is found to decrease to 1.2 when the firebrand density is increased to 230 kg/m^3 and stays nearly equal to 1.0 for the case with firebrand density of 570 kg/m^3. Additionally, in the Appendix a three dimensional representation of the PDF for the lowest density case is illustrated in figure A.5.

Normalized statistics pertaining to the landing locations of the firebrands for all cases is reported in Table 4.1. Here, statistical quantities are normalized by the release height z_r. They help to characterize the PDF's displayed in figure 4.14. Table 4.1 confirms the mean streamwise coordinate of the deposited firebrands $\langle x_p \rangle$ increases as the firebrand density decreases. A similar trend is seen for the variances in the streamwise and spanwise directions. Except for the case with firebrand density of 570 kg/m^3, firebrands released from the 40 m height have a smaller normalized streamwise variance, as compared to that from the 20 m release height. This difference is because the firebrands falling from the 40 m elevation attain a terminal velocity just before reaching the TBL and also owing to inertia, these firebrands are less susceptible to be influenced by the turbulent fluctuations as compared to the case with release height of 20 m. For the lowest density firebrand, when released from a height of 40 m, the

ratio of the streamwise and spanwise variances is the largest ∼45. The distribution of the deposited firebrands appears symmetric in the spanwise direction, as seen in figure 4.14, because of a statistical symmetry of the carrier flow in this direction and that all firebrands are released at the symmetry plane located at $y = 20$ m. Our calculations also showed that $\langle y_p \rangle = 20$m for the deposited firebrands in all cases.

Also, shown in Table 4.1 are the multivariate skewness and kurtosis of the PDF to quantify the deviation of the PDF from a bivariate Gaussian distribution. For a Gaussian distribution, the multivariate skewness is zero. From Table 4.1 it is seen that the skewness is nonzero and positive in all cases. For the cases where firebrands were released from a height of 40 m, the deposition of firebrands is more skewed. Here, firebrands traverse through the TBL for a longer period in time as compared to the ones released from a lower elevation. However, for the lowest density case (70 kg/m^3) released from a height of 40 m, the ground distribution is less skewed. Here, the firebrands first travel through the free-stream velocity region, where turbulence is lacking in the carrier flow, and then through the TBL where fluctuations in flow velocities become significant. When the density of the firebrand is low, the firebrands reach their terminal velocity well before entering the TBL. Once the firebrand reaches its terminal velocity, which is the maximum velocity attained in the vertical direction, it is not largely affected by the fluctuations in the TBL. Hence, the deposition is less skewed as compared to the other cases. Also shown in Table 4.1 is the kurtosis for various cases. Based on Mardia's kurtosis test [62, 63], for a bivariate distribution, the kurtosis for a normal distribution is eight. For the bivariate PDF shown here, for all the cases, the kurtosis is greater than eight and hence we conclude that the

Table 4.1: Normalized statistics pertaining to the distribution of deposited firebrands.

Release Height (m)	Density (kg/m^3)	$\langle x_p \rangle / z_r$	$\langle x'_p x'_p \rangle / z_r^2$	$\langle y'_p y'_p \rangle / z_r^2$	$\langle x'_p y'_p \rangle / z_r^2$	Bivariate Skewness	Bivariate Kurtosis
	570	3.40	0.07	0.01	1.00E-4	0.04	8.21
20	230	4.40	0.10	0.01	7.50E-5	0.03	8.36
	70	6.71	0.22	0.01	-2.00E-4	0.08	8.59
	570	3.12	0.01	2.73E-3	6.25E-5	0.12	8.78
40	230	4.44	0.03	2.83E-3	2.18E-4	0.28	9.11
	70	7.70	0.15	3.43E-3	2.94E-5	0.08	8.64

distribution is leptokurtic. Except for the cases with firebrand densities 570 and 230 kg/m^3 released at 20 m height, the calculated multivariate kurtosis deviated more than 5% of that of a normal distribution.

4.4 Chapter Summary

In the current work, the impact of turbulence in the ambient wind on the transport and deposition of firebrands in a TBL was studied. Specifically, the motion of firebrands was tracked for the spotting range classified to be intermediate wherein firebrands are carried mainly by the turbulent ambient wind, and the flow field is essentially uninfluenced by heat release. In a real fire scenario, firebrands are generated in various shapes and sizes, and mass and size distributions. This study is limited to cylindrical firebrands with the choice of the physical properties of firebrands motivated by the tree burn experiments of Manzello et al. (2007, 2009) where generated firebrands were predominantly cylindrical in shape. A Lagrangian particle tracking module was developed to solve for the coupled translational and rotational motion of cylindrical firebrands. This model was then integrated with WFDS to solve for the

background air flow turbulence. Using the rescaling and recycling method of [54], a TBL was generated. The statistics of the resulting flow field obtained from such a boundary layer was then validated against data available in the literature. Firebrands were released consecutively in the TBL at points within and above the boundary layer edge with identical physical properties and initial velocities. The path followed by the firebrands and ground deposition was studied for three cases of densities ranging from 570 to 70 kg/m^3. Due to inertia, the firebrands with density of 70 kg/m^3 released from a height of 40 m, travelled the longest distance approximately 275 m, while the firebrand with the highest density released from a height of 20 m, travelled the least distance which is approximately 75 m. Although, firebrands were released with zero initial velocities, all firebrands accelerated rapidly and attained velocities close to the free stream velocity within approximately 1 second and all firebrands attained their terminal velocity at the time of deposition. The spatial distribution of firebrands which is mainly understood in terms of statistical quantities such as dispersion and diffusivity was also studied. For firebrands released at the height of 40 m, the dispersion remained close to zero until the firebrands encountered the TBL after which the dispersion increased significantly. Normalized statistics pertaining to the distribution of landed firebrands was also calculated. Statistics pertaining to the coordinates of the landed firebrands in the streamwise and spanwise directions were calculated. In all simulated cases, the streamwise variance was found substantially larger than the spanwise variance. The co-variance was found negligible. After calculation of skewness and kurtosis, deviation from Gaussianity was found significant in the cases cases where the density of firebrands was 230 and 570 kg/m^3 and

the release height was from 40 m. The statistical techniques that are introduced in this work to characterize the moving and deposited firebrands can have applications in situations where flow configuration is different from what is considered in this work.

CHAPTER 5

DISPERSION AND DEPOSITION OF BURNING FIREBRANDS IN A
TURBULENT BOUNDARY LAYER

5.1 Introduction

In Chapter 4, the dispersion and deposition of non-burning firebrands in a TBL
was studied. During transport, firebrands burn, thereby losing heat and mass due
to pyrolysis, char oxidation, convection and radiation. In this chapter, the effects of
burning are included with the firebrand dynamic model introduced in Chapter 4 and
statistical analysis is carried out to investigate the effects of background air turbu-
lence on the dispersion and ground deposition of burning firebrands. The burning of
cylindrical firebrands was modeled using the thermally thin assumption as described
in Equation 2.14-Equation 2.19. The firebrands undergo mass loss due to pyroly-
sis and char oxidation processes. Arrhenius-type rate equations were used to model
these processes. The associated thermokinetic parameters are shown in Table 2.1
[34, 71]. Firebrands also exchanged heat with the surrounding air through convection
and thermal radiation.

5.2 Computational Setup

The computational setup considered here to simulate the TBL is the same as that described in Chapter 4, where the computational domain size is $250 \times 40 \times 75$ m in the x, y and z directions, respectively. The grid resolution is $420 \times 67 \times 90$ and stretched polynomially in the z direction. The free stream velocity of the considered TBL is 18.8 m/s with the boundary layer height set to 25 m at the inlet. Four simulations were performed with two different firebrand initial densities of 570 and 230 kg/m^3 and two release heights of 20 and 40 m. In each simulation, firebrands were released consecutively from the release point. At the time of release, the temperature of the firebrands was assumed 773 K. The initial physical properties, such as the firebrand length and diameter are the same as that described in Chapter 4. Additionally, justification for the choice of parameters including wind speed, boundary layer height, and densities of firebrands is discussed in detail in Chapter 4.

5.3 Results and Discussions

5.3.1 Validation of the Firebrand Burning Model Against Wind Tunnel Experiments

First, to validate the Arrhenius based firebrand burning model, simpler stand alone computations were performed to replicate previous experiments [73] where several samples of oven dried cylindrical firebrands were held fixed and burned in a wind tunnel. Here, firebrands were held in a uniform air flow of velocities of 4.5 and 6.7 m/s. Firebrands had a length of 12.7 cm and diameter ranging from 1.3 to 2.5 cm.

Four different wood species, namely, Ponderosa Pine, Englemann Spruce, Western Larch and Western Red Cedar were used for firebrand samples. Their density varied from 300 to 800 kg/m^3. The firebrands were first ignited and after burnout, their remaining fractional loss was measured. In the experiments, the fractional loss was defined as

$$\text{Fractional Loss} = 1 - \frac{\rho_p D}{\rho_{p,0} D_0}, \tag{5.1}$$

where, $\rho_p, D, \rho_{p,0}$ and D_0 are the final density, final diameter, initial density and initial diameter of the firebrand respectively. In total, 33 experiments were performed, including multiple experiments for each species with different firebrand densities and dimensions.

In the present study, using the firebrand burning equations Equation 2.14 and Equation 2.18, two distinct sets of computations were carried out for conditions similar to Muraszew's experiments. In the first set, the thermokinetic parameters for the various firebrand species were adopted from the work of Sardoy et al. [97], in which a similar validation study was performed. In Sardoy et al. [97], the thermokinetic constants of Pinus species were used for the Ponderosa Pine firebrands. For the rest of the species, due to lacking precise thermokinetic constants, Sardoy et al. [97] used the ones available for forest litter, as shown in Table 5.1.

In the experiments, since the firebrands burned for a long duration (> 100 s), they also underwent surface regression. For the 33 experimental cases, comprising various species, it is noted that the average firebrand diameter decreased by 30% of

Table 5.1: Thermokinetic parameters for the pyrolysis gas for different firebrand species [97].

Species	A_i (s^{-1})	T_i (K)
Ponderosa Pine	725	6899
Forest Litter	3.2	4402

that of the original. Hence, Sardoy et al. [97] assumed firebrands to be thermally thick, and accounted for surface regression in the radial direction. For this reason, in the current validation exercise, the equations governing the regression of the firebrand [97] was also included in the firebrand degradation model:

$$\frac{dV_{\mathrm{p}}}{dt} = -R_{\mathrm{char}}S, \tag{5.2}$$

where

$$R_{\mathrm{char}} = -\frac{48 D_{O_2} \rho_{\mathrm{gas}} \ln(1 - \gamma Y_{O_2})}{32 D \gamma} \left(\frac{T}{273}\right)^{0.75} (1 + 0.272 \mathrm{Sc}^{1/3} \mathrm{Re}^{1/2}). \tag{5.3}$$

As shown in Equation 5.2, the firebrand is assumed to undergo reduction in volume only via char oxidation process. Furthermore, in this model, it is assumed that the rate of char oxidation is mainly governed by the rate at which oxygen diffuses onto the surface of the fuel. It is noted that Equation 5.3 was originally proposed by Mulcahy [72] for spherical particles; however, Sardoy et al. [97] used it for cylindrical and disk shape firebrands. In Equation 5.3, D_{O_2} is the diffusion coefficient of oxygen set to 18×10^{-6} m^2/s, Y_{O_2} is the mass fraction of oxygen and Sc is the Schmidt number at standard air condition and set to 0.71 here. In these computations, it is
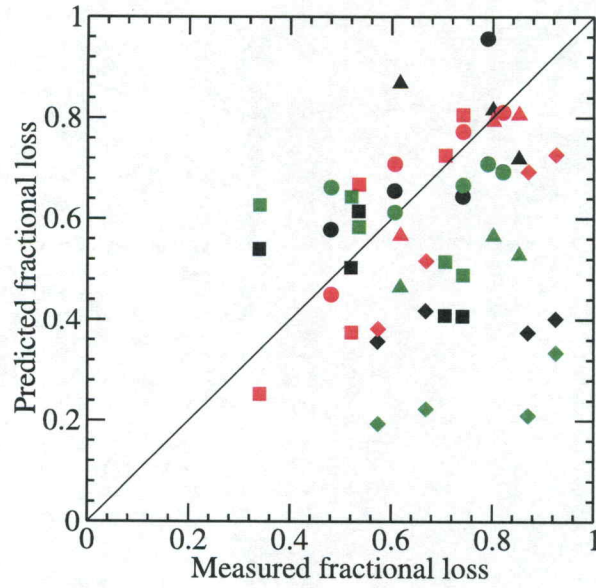
(a)
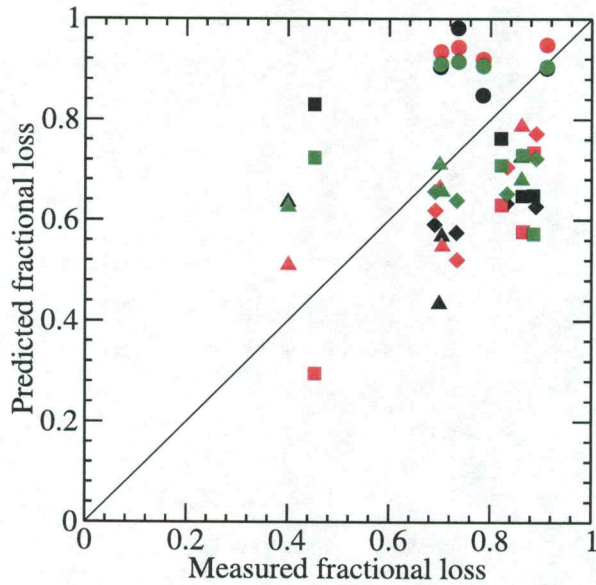
(b)

Figure 5.1: Predicted fractional loss versus measured fractional loss [73] for fire-brands of different species (Ponderosa Pine (circle); Englemann Spruce (square); Western Larch (triangle); Western Red Cedar (diamond) for two wind velocities: (a) 15 mph and (b) 10 mph in current simulations with kinetic parameters adopted from Sardoy et al. [97] (black symbols) and Porterie et al. [87] (green symbols) and simulations of Sardoy et al. [97] (red symbols).

assumed that, during the pyrolysis process, the oxygen mass fraction is negligible in the vicinity of the firebrand due to the presence of pyrolysis gases whereas during the char oxidation process, the mass fraction of oxygen, is set to its value 0.23 at the standard air condition. The Reynolds number, Re is calculated based on the relative velocity between the firebrand and the ambient air and an equivalent sphere diameter.

In the second set of computations, the thermokinetic parameters of the pyrolysis gas (shown in Table 3.1), adopted from the work of Porterie et al. [87] was used for all firebrand species. Also, since Equation 5.3 is applicable for spherical particles [72], in the second set of computations, the surface regression of the firebrands was not considered. The standalone validation computations were performed by solving the coupled ordinary differential equations pertaining to mass and temperature evolution and the surface regression of the firebrand using the fifth order Runge-Kutta scheme to advance in time. The initial firebrand properties such as the density, length and radius were consistent with that of the experiments.

As illustrated in figure 5.1, the predicted fractional losses from both sets of computations were plotted against the measured fractional loss from experiments. Computations performed using the model adopted from Sardoy et al. [97] are represented by black symbols and those performed using thermokinetic parameters of Porterie et al. [87] are represented by green symbols. The simulated data of Sardoy et al. [97], represented by red symbols, are also shown in this figure. Also, different symbols with different shapes are used to represent the various firebrand species. It is observed that the predicted data using the model adopted from Sardoy et al. [97] are relatively close to that of the experimental data for most of the cases. For both wind speeds,

93

the computed fractional loss of the Ponderosa Pine species lies within 20% of the experimental measurements. Also, for all the species, most of the simulated fractional losses lie well within the range of the numerical data of Sardoy et al. [97]. However, few of the model predictions pertaining to the Englemann Spruce and Western Larch species are observed to deviate significantly from the experimental data. The discrepancies between the experimental and numerical results are attributed to the fact that, during the experiments, some of the firebrands were only partially burned whereas others were blown away and yielded lower fractional density values at the end of the experiment. The uncertainty in thermokinetic constants in the Arrhenius model may also be a source of error.

Since the overall agreement between the experiments and the simulations were found to be relatively close for the Ponderosa Pine species, for the LES simulations described in the next section, the firebrand burning model was based on the thermokinetic parameters for the Ponderosa Pine species as given by Sardoy et al. [97]. However, the surface regression of the cylindrical firebrands was not considered due to the limitation in its applicability to burning cylindrical firebrands.

5.3.2 Simulation of Burning Firebrands Released in a Turbulent Boundary Layer

In the present section, statistics pertaining to burning firebrands released in the TBL are presented for simulations with different initial firebrand densities and release heights. The statistics in each simulation are calculated by performing an ensemble
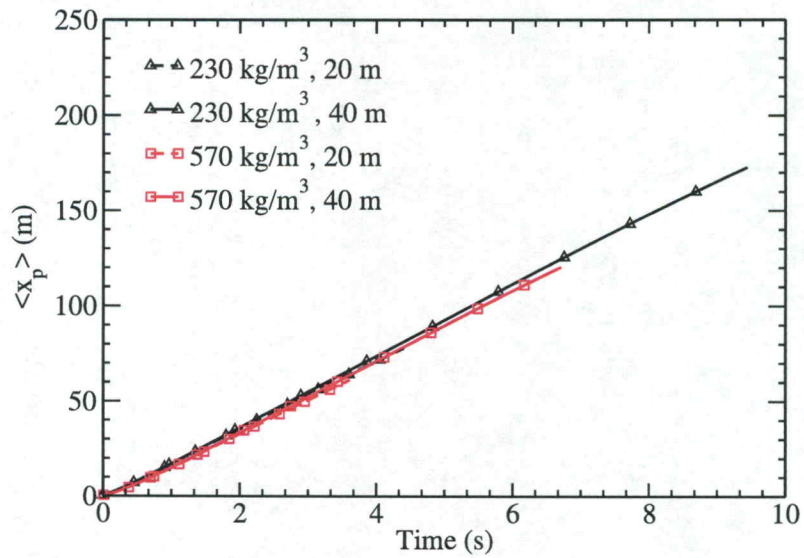
(a)
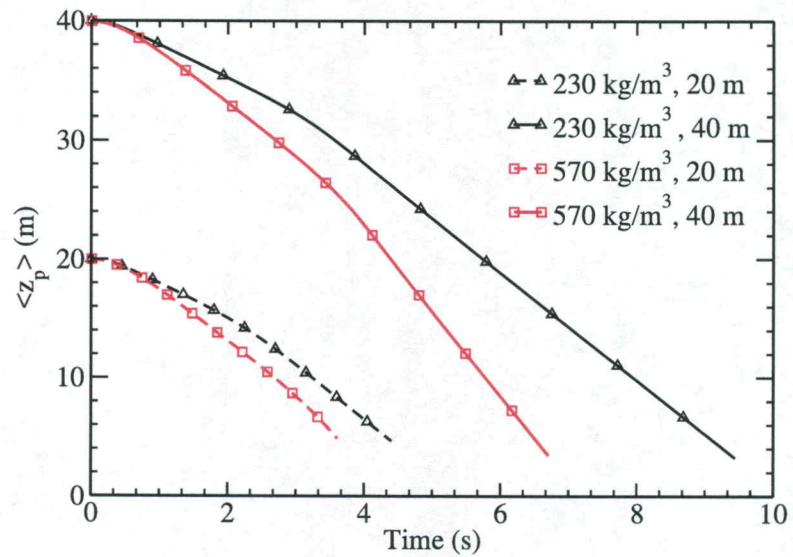
(b)

Figure 5.2: Temporal variation of the mean (a) streamwise and (b) vertical components of firebrand positions for release heights of 40 m and 20 m for initial densities of 230 and 570 kg/m³.
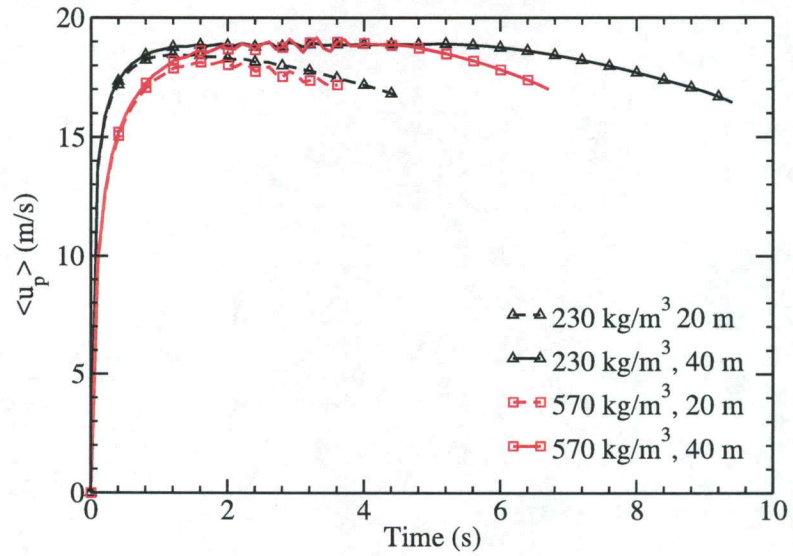
(a)
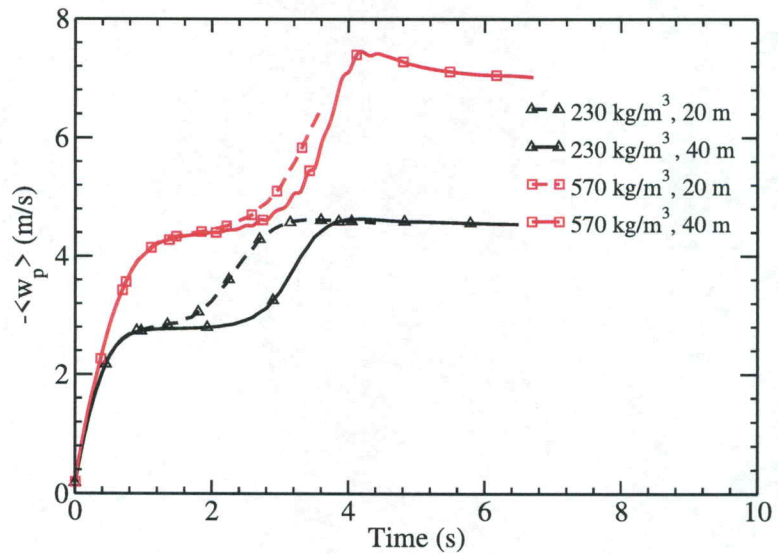
(b)

Figure 5.3: Temporal evolution of the mean (a) streamwise and (b) vertical components of the firebrands velocities for release heights of 40 m and 20 m for initial densities of 230 and 570 kg/m^3.

average over all firebrands from the time of release to the time of deposition (similar to that discussed in Chapter 4).

In figure 5.2(a) and (b), the time evolution of the mean streamwise and vertical position of the firebrands is shown. It is noted that the burning firebrands exhibit similar trends in the temporal evolution of the mean position in both streamwise and vertical directions as compared to that of the non-burning firebrands discussed in Chapter 4. In the streamwise direction, the mean position of firebrands varied almost linearly with time. Since burning firebrands lose mass, they travel for a longer distance as compared to non-burning firebrands. Specifically, for firebrands released from a height of 40 m with an initial density of 570 kg/m^3, they travel around 10 m (in the mean sense) further than the non-burning ones at the time of deposition. The variation of the firebrand mean velocity was found to be comparable with the non-burning case discussed in Chapter 4.

Figure 5.3(a) shows that although firebrands were released with zero initial velocities, they closely attained the streamwise velocity of the background flow in a relatively short time (within 2 s upon release). As seen in figure 5.3(b), the magnitude of the mean vertical velocity of the firebrands increases owing to the gravitational force and firebrands reach their terminal velocity prior to deposition. The plateau in the mean vertical velocity prior to terminal velocity is attributed to the orientation of the firebrand during descent. This behavior was also observed and discussed in the results obtained with non burning firebrands in Chapter 4. Overall, the mean vertical velocity of burning firebrands is observed to be closely comparable to that of non-burning firebrands.

97

One of the most significant factors influencing the possibility of the creation of spot fires is the firebrand temperature at the time of deposition. To better understand what influences this temperature, time histories of the mean firebrand density and temperature are examined in figures 5.4 and 5.5 respectively. At the time of release, firebrands have an initial set temperature of 773 K. The condensed phase reactions, which include the process of pyrolysis and char oxidation are largely a function of the temperature of the firebrand. Arrhenius rate equations as given by Equation 2.18 and Equation 2.19 are used to determine the rates of pyrolysis and char oxidation. At early times, the rate at which the condensed phase reactions occur is significantly higher than at later times (also lower temperatures). Since the firebrand diameter is kept unchanged throughout flight, the mean firebrand density decreases very rapidly at early times and remains nearly constant afterwards as the firebrand cools to lower temperatures.

It is noted that vegetative fuels pyrolyze above a temperature ranging between 400 and 500 K across various plant species [69, 71]. Hence, at later times, as the firebrand temperature drops below 500 K, as shown in figure 5.5, the condensed phase reactions cease. As a result, the firebrand density does not vary with time, as observed in figure 5.4. Since the firebrand dimensions considered in this work are relatively small, i.e., 1.5 mm in radius and 4 cm in length, it is observed that firebrands cool rapidly and undergo a reduction in density only within the first few seconds of their release time. Also, for the cases with firebrands having an initial density of 570 kg/m^3, the density reduces significantly with time in comparison to the firebrands with an initial density of 230 kg/m^3 which cool rapidly as time progresses. For instance,

the firebrands with a density of 570 kg/m^3 undergo a reduction in density by 20 kg/m^3, whereas the reduction in density for the 270 kg/m^3 is an order of magnitude smaller due to rapid cooling. Furthermore, it can also be seen in figure 5.5, that the firebrands with lower density, regardless of their release heights, lose heat rapidly and attain temperatures close to the ambient at the time of deposition. However, the higher density firebrands released from a height of 20 m, have a mean temperature close to 450 K at the time of deposition.
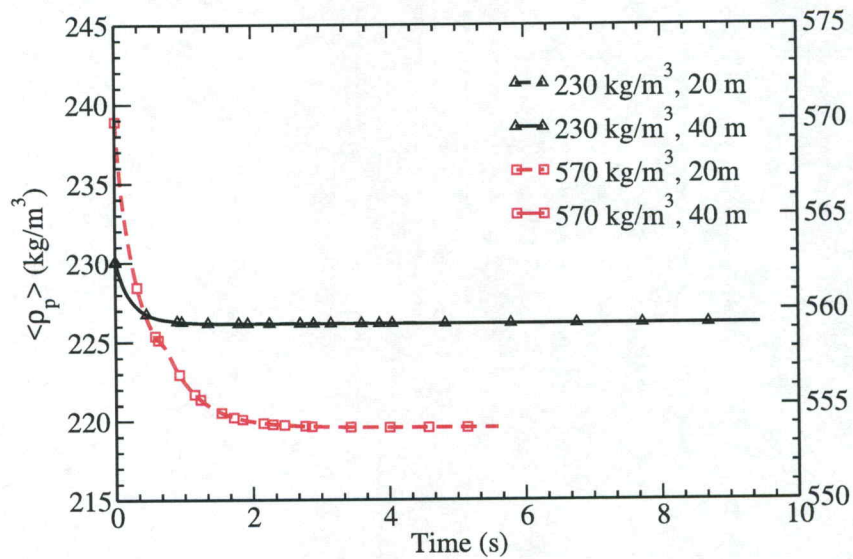
Figure 5.4: Temporal evolution of the mean density of firebrands for release heights of 40 and 20 m. The left vertical axis is for firebrands with initial density of 230 kg/m^3, and the right one for 570 kg/m^3.

The temperature of the firebrand at any given time is affected by the processes of pyrolysis, char oxidation, convective and radiative cooling. It is observed that the firebrand temperature is predominantly affected by the convective and radiative
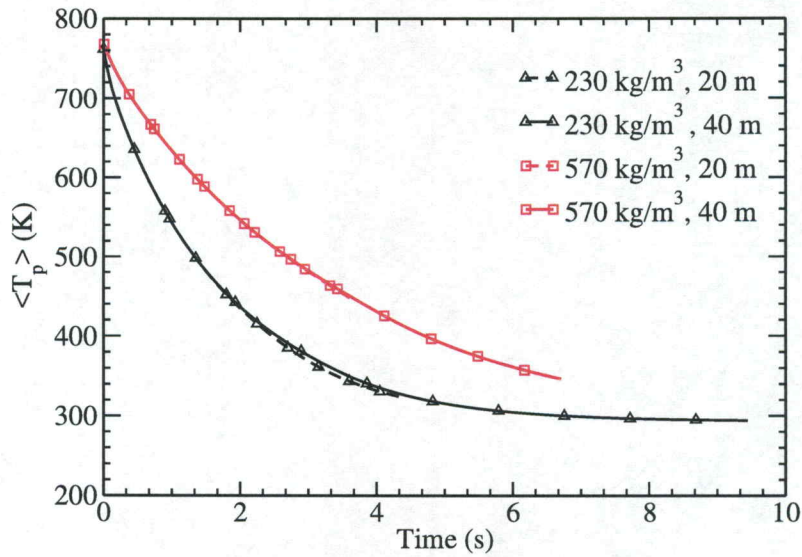
Figure 5.5: Temporal evolution of the mean temperature of firebrands for release heights of 40 and 20 m with initial densities of 230 and 570 kg/m^3.

modes of cooling. The heat loss in firebrands due to the processes of convective and radiative mechanisms is shown in figure 5.6 (a) and figure 5.6 (b) respectively. The firebrand cools by convection owing to the relative velocity between the firebrand and the ambient air. As seen in Equation 2.15 and Equation 2.17, the heat transfer coefficient is calculated in terms of the Reynolds number based on the relative velocity of the firebrand. Since the firebrands are released with zero initial velocity, the relative velocity of the firebrands with respect to the background flow is large at early times. In addition, there also exists a large temperature difference between the ambient temperature and the firebrand temperature at this stage. Due to these factors, the mean convective heat loss of the firebrand is significant at initial times, as shown in figure 5.6 (a). At later times, as the firebrand descends, the convective heat loss
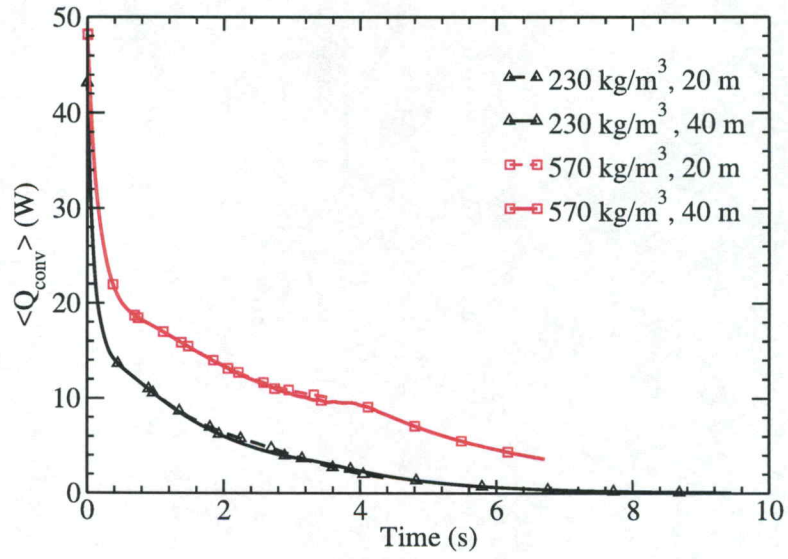
(a)
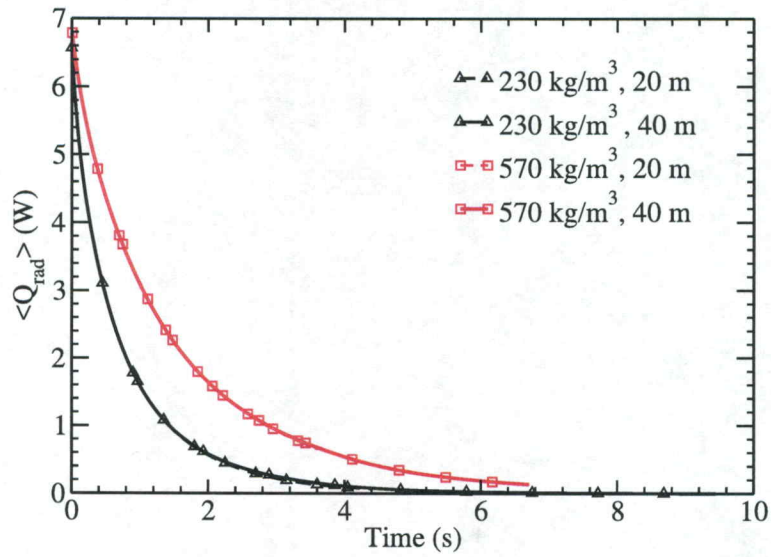
(b)

Figure 5.6: Temporal evolution of mean (a) convective and (b) radiative heat loss of firebrands released from two distinct elevations of 20 and 40 m with initial densities of 230 and 570 kg/m³.

component also decreases. The temporal variation of the mean radiative heat loss component is shown in figure 5.6 (b). Here, the firebrands have an emissivity of 0.9, which is a characteristic of wildland vegetation. As with the convective heat loss, due to the large temperature difference between the firebrand and the ambient temperature at the release time, the radiative heat loss component is also significant initially. However, it is observed that regardless of the firebrand density and release height, the component of heat loss by radiation is an order of magnitude lesser than the convective heat loss component. For the lowest density cases ($230\,\mathrm{kg/m^3}$), at times close to landing, the heat loss components approach zero as the firebrand temperature approaches that of the ambient. While on the one hand, a zero initial firebrand velocity provides a convenient framework to assess overall statistics, on the other hand, the high relative velocity, coupled with high temperature promotes significant convective cooling, which in turn deactivates the burning process.

The background air turbulence plays an important role in influencing the dynamical and thermal behavior of firebrands and hence the energy of the firebrands at the time of deposition. The turbulent wind disperses and diffuses the firebrands in various directions. In figures 5.7 and 5.8, the components of dispersion and diffusion of burning firebrands during flight is illustrated: their definitions are provided in Chapter 4. Since the firebrands released at a height of 40 m are in the free stream region at the time of release, the dispersion and diffusion components remain close to zero for a longer time as compared to the ones released within the TBL. Upon entering the boundary layer, the dynamical behavior of firebrands is significantly affected by the turbulent background air and hence the magnitude of the dispersion and
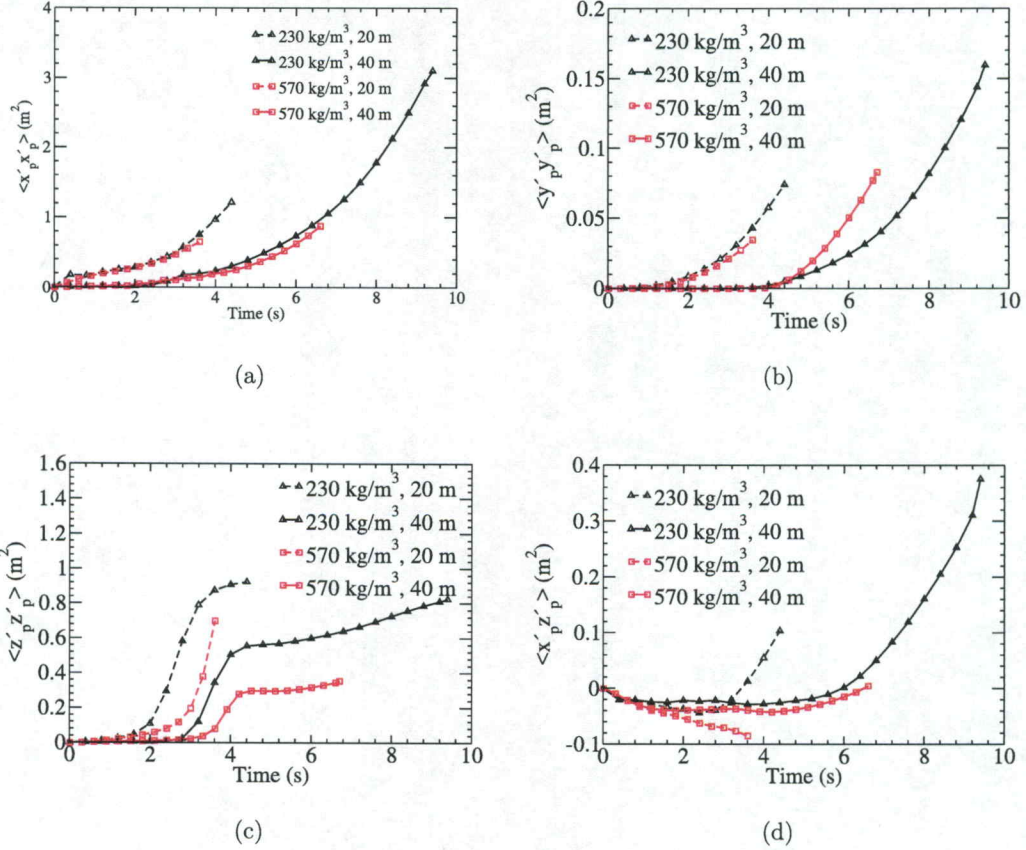
Figure 5.7: Time evolution of components of firebrand dispersion released from heights of 20 m and 40 m with initial densities of 230 and 570 kg/m^3.

diffusion components increase as time progresses. In the vertical direction, similar to the non-burning cases, the slope of the dispersion $\langle z'_p z'_p \rangle$ changes and correspondingly, the diffusivity D_{xx} peaks at early times and plateaus at the time of deposition. This behavior as explained in detail in Chapter 4 is attributed to the terminal velocity attained by the firebrands at later times. It is to be noted that only those components whose values were found to be significant is shown in these figures. Since the density reduction of the burning firebrands is less than 3% as noted earlier, the temporal
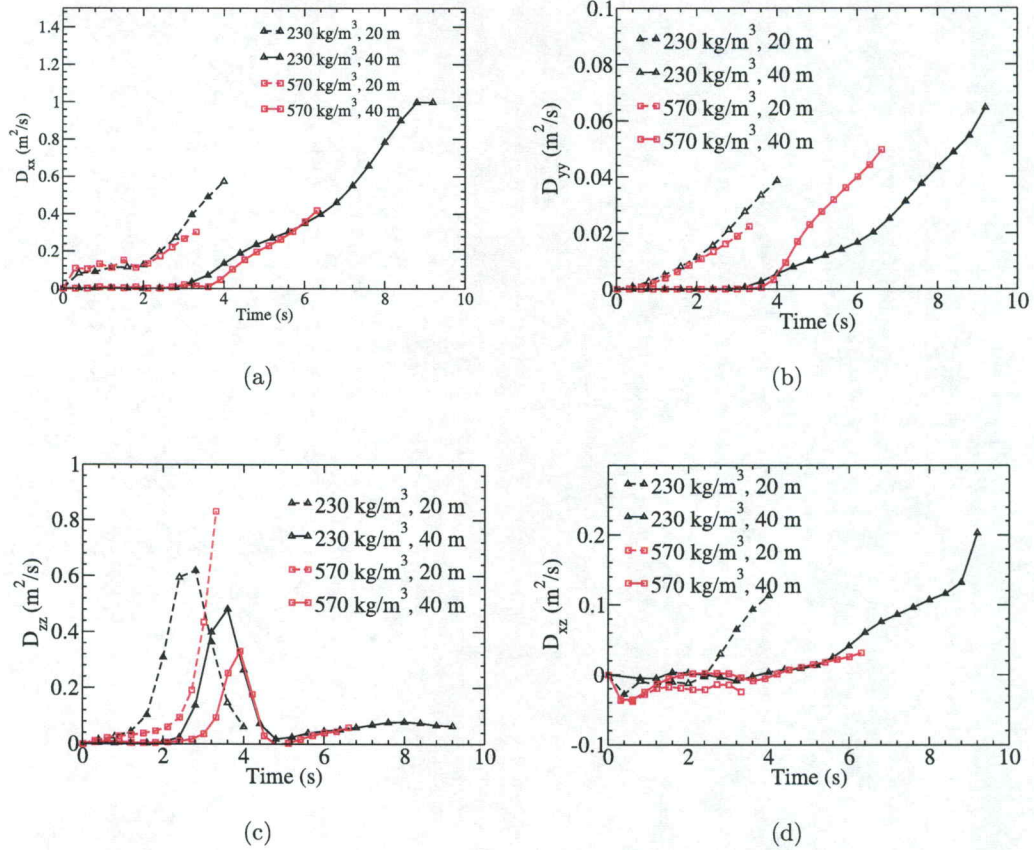
Figure 5.8: Time evolution of components of firebrand diffusion released from heights of 20 m and 40 m with initial densities of 230 and 570 kg/m³.

variation in both the diffusion and dispersion components are comparable to that of the non-burning firebrand results discussed in Chapter 4.

In order to further examine, the dispersion and diffusion of firebrands are shown in figure 5.9. All variances are zero at the beginning due to zero initial velocities at the time of release. However, owing to a high initial temperature at early times, firebrands pyrolyze at a high rate, undergoing a rapid reduction in density. Since the density of the individual firebrands may vary largely from one to another at early

104

times, the variances of the firebrand velocity $\langle u'_p u'_p \rangle$ and $\langle v'_p v'_p \rangle$ have a significantly higher value as compared to the non-burning firebrands. This is manifested by a sharp peak in figure 5.9(a,c) at the very beginning. At later times, as the firebrand temperature drops, the density reduction is not significant and the velocity variances decrease. However, at later times, the firebrand is also influenced by the turbulent fluctuations of the background flow and hence the velocity increases with time similar to the non-burning firebrands.
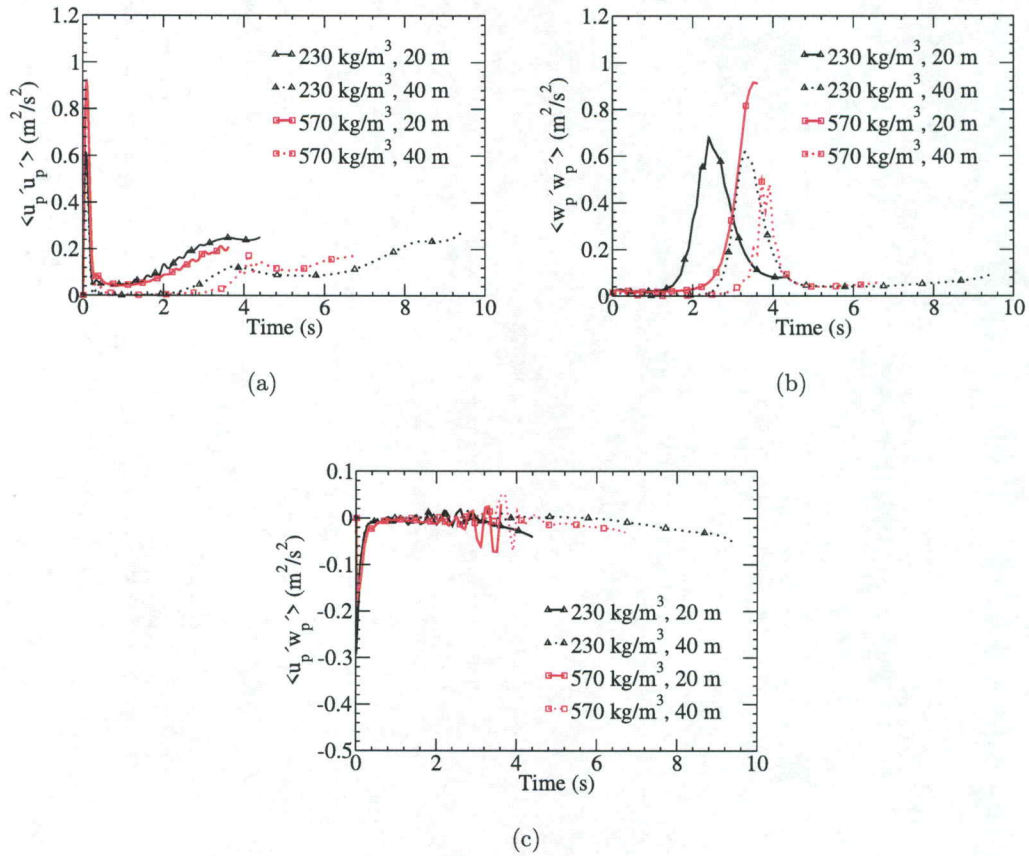

Figure 5.9: Time evolution of the variances of the firebrand velocities released from heights of 20 m and 40 m with initial densities of 230 and 570 kg/m^3.

The air turbulence also effects the density and thermal behavior of the firebrands. To illustrate this behavior, the variances in density and temperature of the firebrand are shown in figures 5.10 and 5.11. As evident from these figures, owing to the turbulent velocity field, at early times, the variances in density and temperature of firebrands released within the TBL, i.e., at height of 20 m, increases rapidly. As time progresses, the firebrand cools, condensed phase reactions cease, and hence the variances decrease. However, it is evident that for the firebrands released outside the boundary layer due to the absence of turbulence, the variances in density and temperature remain close to zero at all times. At later times, the firebrands cool and hence, when they enter the turbulent region of the boundary layer, the fluctuations do not significantly influence the density or the temperature. Thereby the variances remain close to zero at all times when released outside the boundary layer.

In order to gain further insight into the dynamics of firebrands, specifically their orientation relative to the local relative velocity is examined. Figure 5.12 shows the time variation of the mean firebrand incidence angle $\langle \alpha \rangle$. Here, the incidence angle is the angle between the firebrand major axis and the local relative velocity vector, also illustrated in figure 2.1. It is seen in figure 5.12 that the incidence angle oscillates about the 90°. At $\langle \alpha \rangle = 90°$, the hydrodynamic torque is equal to zero. As $\langle \alpha \rangle$ deviates from 90°, the hydrodynamic torque tends to resist this deviation. Hence, this angle is the stable equilibrium angle for falling cylindrical rigid bodies in still air [78, 123]. It is seen that the amplitude of the oscillations changes significantly over time with a peak at a time when the mean vertical velocity reduces almost to the terminal velocity as seen in figure 5.3(b). After this time, the aerodynamic forces

106
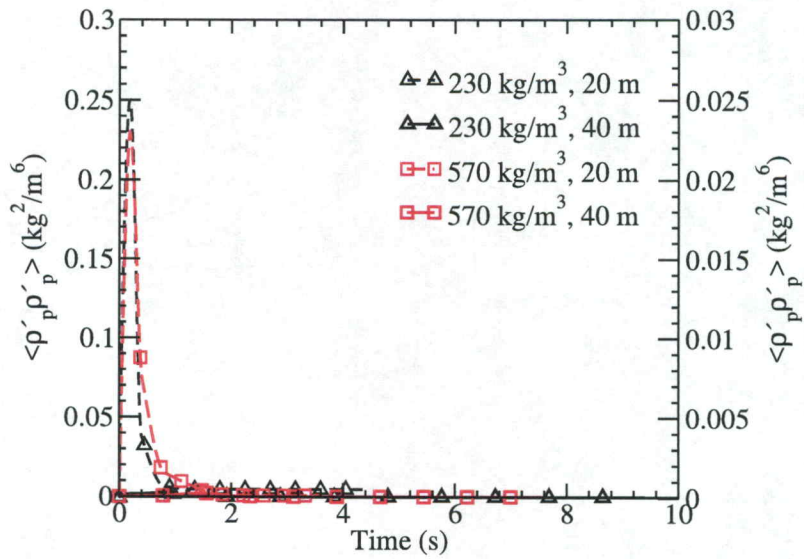
Figure 5.10: Temporal evolution of the variance of density of firebrands for release heights of 40 and 20 m. The left vertical axis is for firebrands with initial density of 230 kg/m^3, and the right one for 570 kg/m^3.

balance the gravitational force and the oscillations are damped out as they fall at a stable orientation at the 90° angle. Firebrands with lower densities have shorter time response and hence the oscillations damp out more rapidly.

In figure 5.13, the variation of the ratio of the mean drag to lift force is shown. The lift and drag forces are computed based on the model proposed by Hoerner [37] for cylindrical objects as shown in Equation 2.4 and Equation 2.5. Here, the drag and lift forces are expressed by resolving the normal force in terms of the sine and cosine components of the firebrand incidence angle, respectively. As seen in figure 5.12, the incidence angle oscillates about the 90° angle. At firebrand incidence angles close to 90°, the sine component is significantly larger than the cosine component. Hence,

107
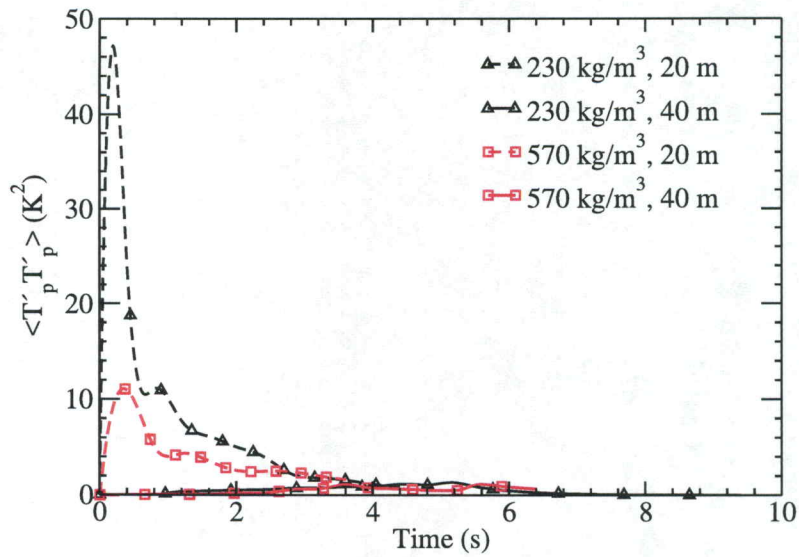
Figure 5.11: Temporal evolution of the variance of temperature of firebrands for release heights of 40 and 20 m with initial densities of 230 and 570 kg/m³.

at the time of release, the drag force acting on the firebrand is found to be greater than the lift force by two orders of magnitude. As the firebrands descend, the ratio becomes a constant with the drag force being almost twice as that of the lift force. At early times, it is noted that the drag and lift forces are significant because the firebrands are released with zero velocities and their Reynolds number is low. As seen from Equation 2.6, for low Reynolds numbers, the value of the drag coefficient used to calculate the both the lift and drag forces is substantially large. However, as time progresses, the firebrand Reynolds number increases and the drag coefficient reduces by two orders of magnitude. Hence, a substantial decrease is observed with time.

To gain insight on the correlation of the temperature of the firebrand with the fluctuating turbulent flow, the firebrand turbulent heat flux quantity is plotted in fig-
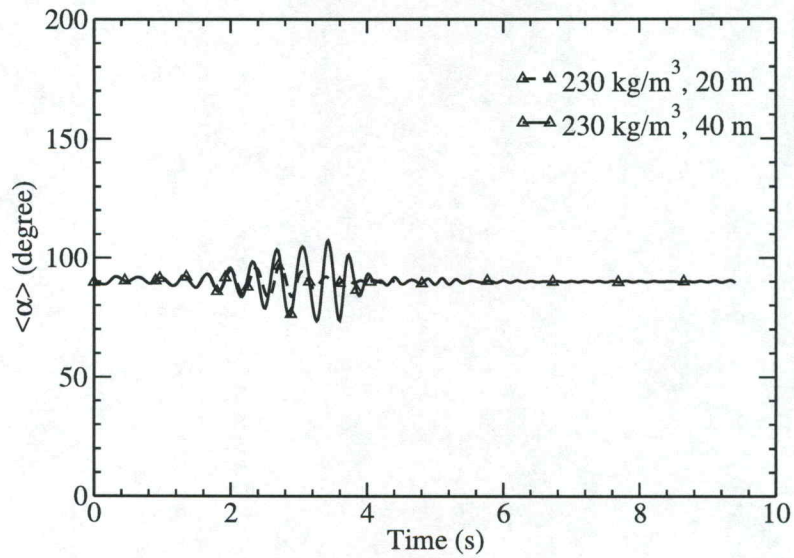
(a)
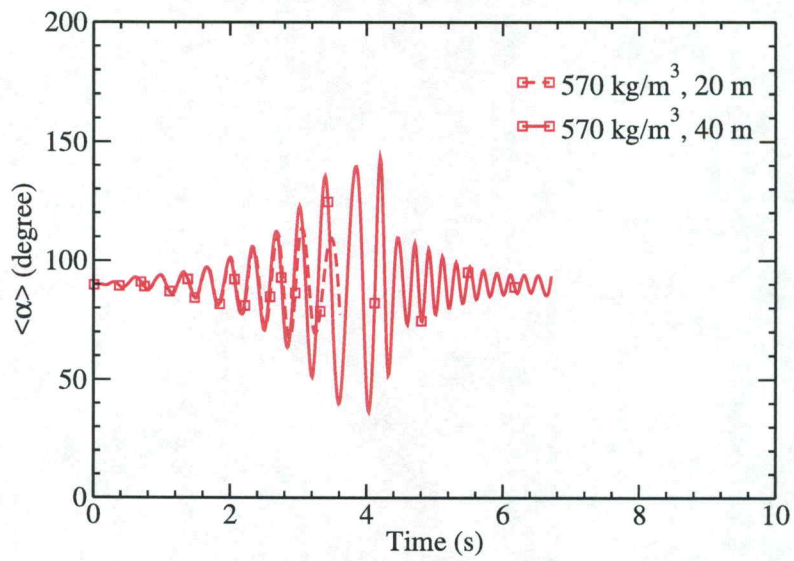
(b)

Figure 5.12: Time evolution of the incidence angle for firebrands released from two distinct elevations of 20 and 40 m for initial densities of 230 and 570 kg/m³.
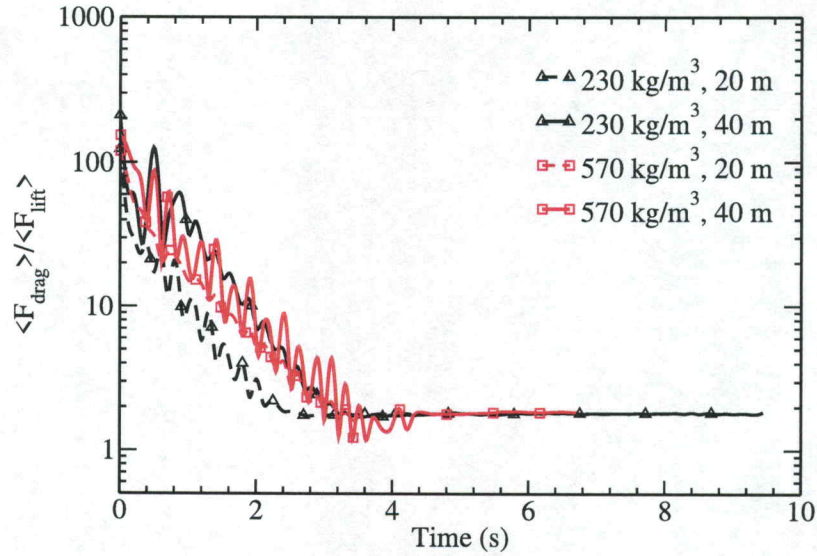
Figure 5.13: Temporal evolution of the ratio of the magnitude of drag and lift force of the firebrand released from two distinct elevations of 20 and 40 m for initial densities of (a) 230 and (b) 570 kg/m^3.

ure 5.14. Here, the streamwise and the vertical components of the firebrand turbulent heat flux are shown. At all times, it is observed that the firebrand turbulent heat flux is negatively correlated, and this behavior is mainly attributed to the decrease in the firebrand temperature as time progresses. In figure 5.14(a), as time progresses, the process of pyrolysis becomes insignificant and the firebrand density remains nearly constant. The fluctuations in the temperature of the firebrand also decreases as the firebrand cools down. In addition, since the firebrands attain velocities close to that of the background fluid, the fluctuations in the streamwise component of the firebrand's velocity decreases. Hence, only at initial times, the streamwise component of the turbulent heat flux is higher in magnitude whereas in a relatively short time
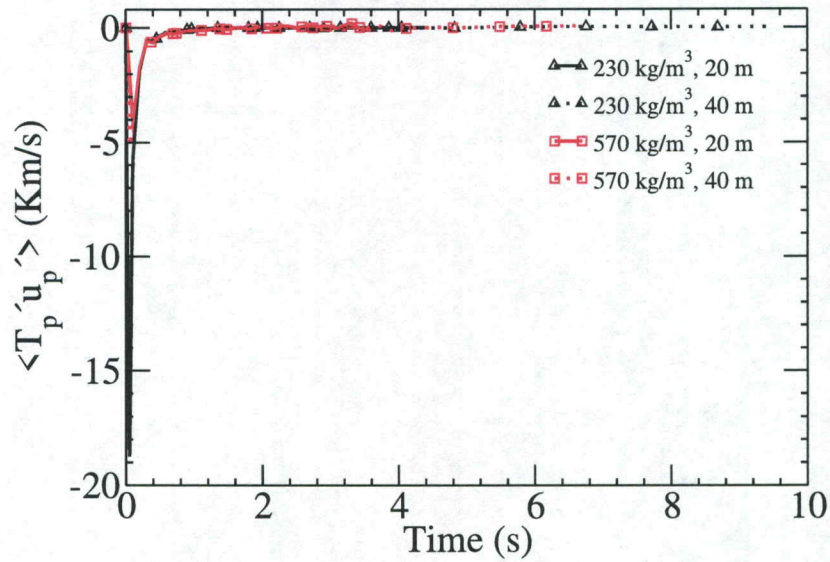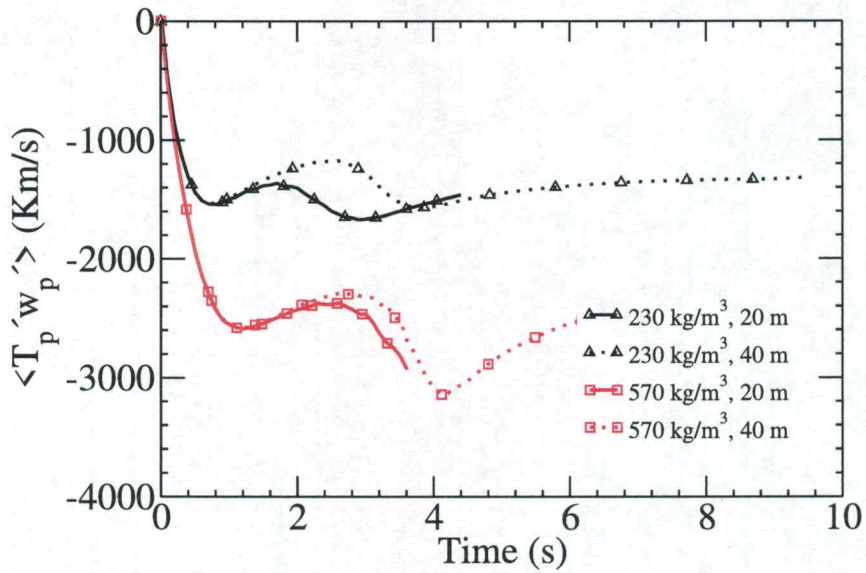
Figure 5.14: Temporal evolution of the mean firebrand turbulent heat flux showing the (a) streamwise and (b) wall-normal components of firebrands released from two distinct elevations for initial densities of 230 and 570 kg/m^3

scale (after completion of the pyrolysis process), there exists no correlation in the streamwise component and the turbulent heat flux tends to zero. However, in the wall normal direction, the magnitude of vertical velocity increases as the firebrand accelerates and attains terminal velocity. Hence, the temporal variation of the turbulent heat flux in this component closely resembles that of the mean vertical velocity of the firebrand. Also, the wall normal component of the turbulent heat flux is observed to be dominant as compared to the streamwise component.

One of the challenges in wildland fires, and especially in wildland-urban interface fires, is a measure of accumulation of firebrands. In order to quantify this, we look at both the mass and energy accumulation from a statistical viewpoint. In figure 5.15 the mass per unit area of the landed firebrands is shown for firebrands released from two different heights and density of 230 kg/m^3 and 570 kg/m^3. Here, $G_h(\mathbf{x})$ also satisfies the normalization property such that $\int G_h(\mathbf{x})d\mathbf{x} = 1$. Here, the mass per unit surface area, $m_{p,\text{ground}}(x, y)$ is calculated via kernel density function, as shown in the equation below:

$$m_{p,\text{ground}}(x, y) = \sum_{p=1}^{N} m_p(x, y) G_h(x - x_p, y - y_p), \tag{5.4}$$

where,

$$G_h(x, y) = \frac{1}{h^2} K\left(\frac{x}{h}, \frac{y}{h}\right) \tag{5.5}$$

where $K(x, y)$ is a bivariate kernel, which is set to a standard normal distribution and h is the bandwidth parameter. N is the number of landed firebrands. The PDF

112

indicates the total mass of the firebrands depositing in a given area. The higher the accumulation in a given area, the higher is the probability of creation of spot fires. In figure 5.15, the innermost contour line represents the maximum mass of firebrands being deposited at the given location. Since the burning firebrands lose mass during flight, they travel further than their non-burning counterparts. Here, for instance, the maximum number of firebrands being deposited for the case of burning firebrands with a density of 230 kg/m^3 is found at 95 m whereas, the non-burning firebrands land close to 5 m prior in the streamwise direction for both the release heights of 20 m and 40 m. A similar behavior is also observed for the higher density firebrands. Firebrands released from the 40 m height are observed to travel approximately twice the distance of that released from a lower elevation. For all the cases, the ground deposition pattern of the firebrands is stretched over a distance of 15 m in the streamwise direction.

The energy per unit surface area of the deposited firebrands is also shown as a function of the spanwise and streamwise direction in figure 5.16. The energy per unit surface area, $e_{p,\text{ground}}(x, y)$ calculated via kernel density function, as shown in the equation below:

$$e_{p,\text{ground}}(x, y) = \sum_{p=1}^{N} c_p m_p(x, y) T_p(x, y) G_h(x - x_p, y - y_p) \qquad (5.6)$$

The energy density indicates the thermal content of the ground deposited fire-brands at the time of landing (kJ). It is observed that the firebrands with an initial density of 570 kg/m^3 have higher energy (greater by an order of magnitude) as com-

pared to the firebrands with a lower initial density. This is because, the firebrands with an initial density of 570 kg/m^3 retain more energy (with temperatures of 450 K) at the time of deposition. This indicates a higher probability of occurrence of spot fires with higher density firebrands as they are less likely to cool and reach ambient temperatures.

In figure 5.17, the variation of the average temperature ($T_{p,\text{ground}}$) of the landed firebrands is shown. Here, the average temperature of the firebrands is calculated using the following equation:

$$T_{p,\text{ground}} = \frac{\sum_{p=1}^{N} c_p m_p(x,y) T_p(x,y) G_h(x - x_p, y - y_p)}{\sum_{p=1}^{N} c_p m_p(x,y) G_h(x - x_p, y - y_p)} \tag{5.7}$$

In all the cases, the firebrands being deposited at an upstream location in the streamwise direction retain more thermal energy. The firebrands travelling longer distances cool further before deposition. While the firebrands with an initial density of 230 kg/m^3 have near ambient temperature at the time of deposition, it is observed that the firebrands with an initial density of 570 kg/m^3 released from a height of 20 m have temperatures close to 430 K at the time of landing. The maximum variation in the average temperature of the ground deposited firebrands is observed for the case shown in figure 5.17 (c), where, the temperature of the ground deposited firebrands varies by almost 30 K in the streamwise direction.
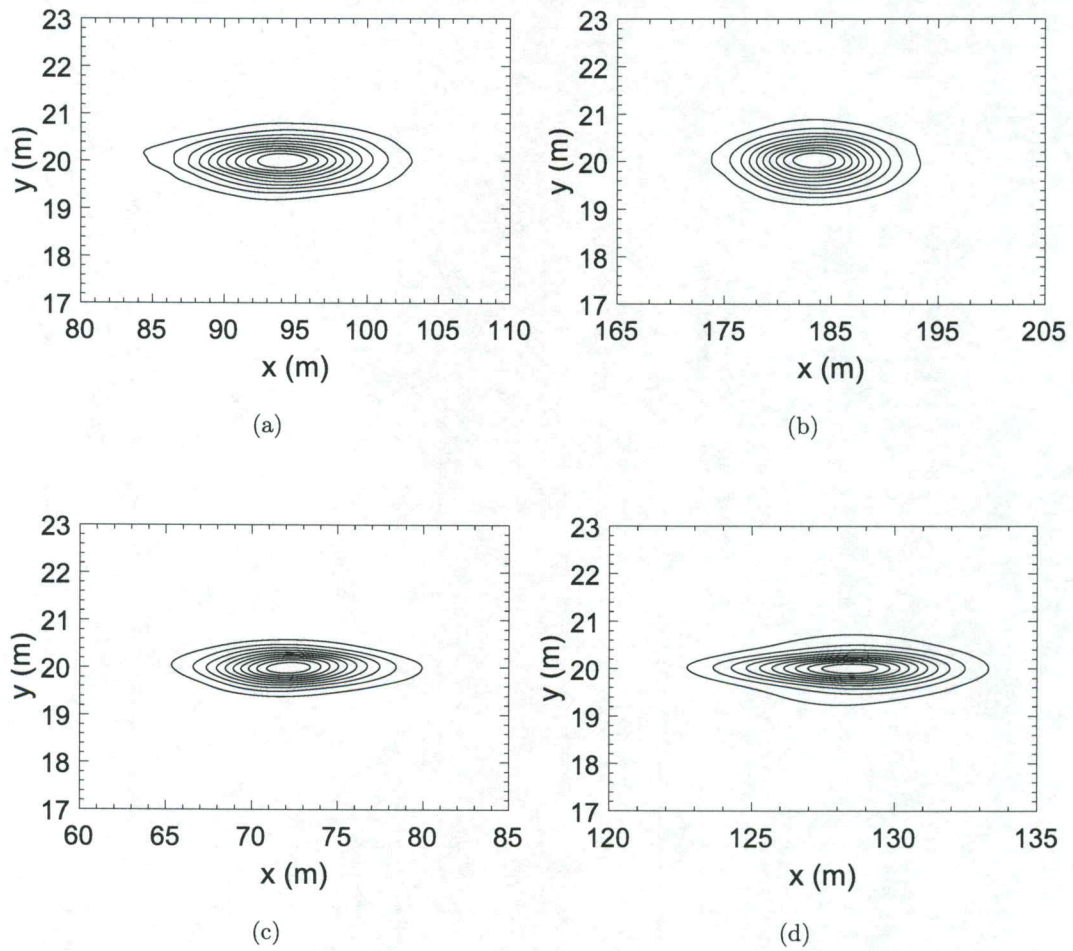
Figure 5.15: Contour plots of mass per unit area of the deposited firebrands for the release height = 20 m (left column) and 40 m (right column) for $\rho_p = 230$ kg/m^3 (top row) and 570 kg/m^3 (bottom row). For the top row, the innermost contour line has a maximum value of 1.5 kg/m^2 and the outermost has a minimum value of 0.2 kg/m^2. For the bottom row, the maximum and minimum values are 0.24 kg/m^2 and 0.02 kg/m^2 respectively.
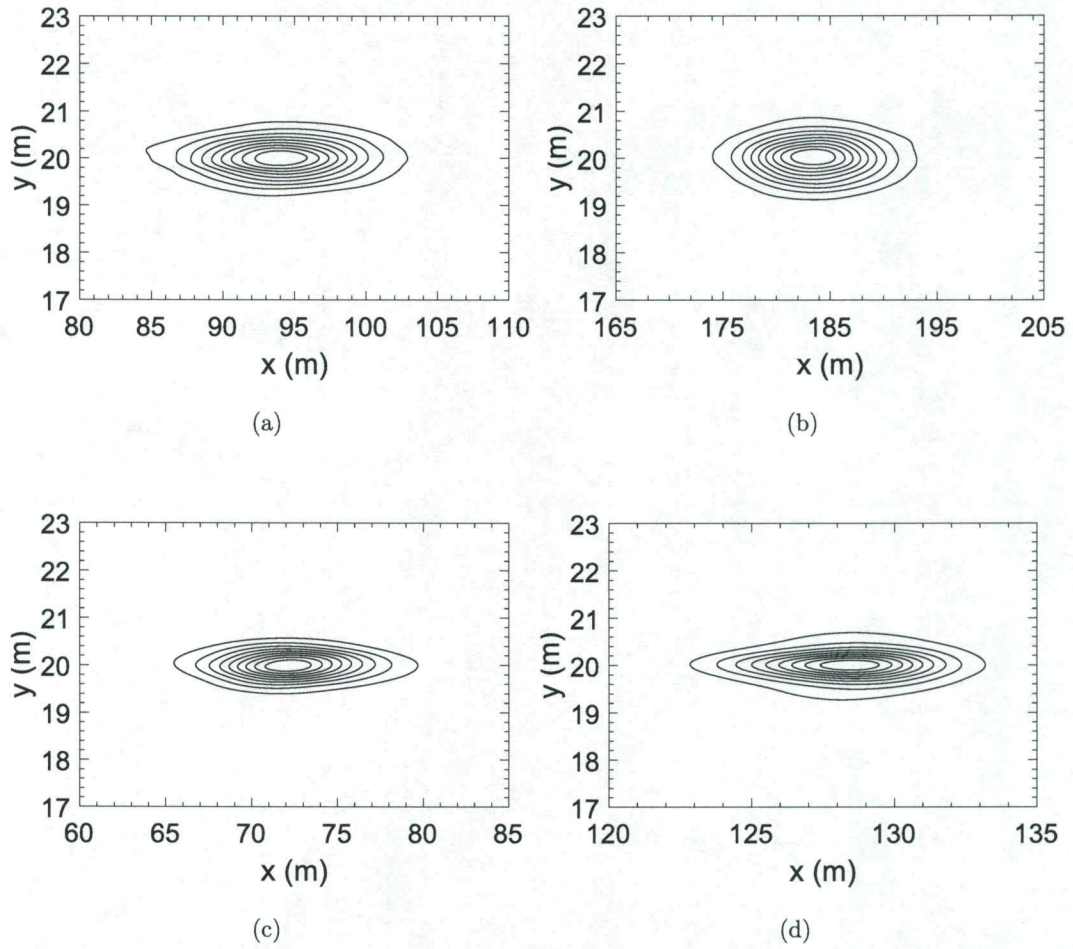
Figure 5.16: Contour plots of energy per unit area of the deposited firebrands for the release height = 20 m (left column) and 40 m (right column) for $\rho_\mathrm{p} = 230$ kg/m^3 (top row) and 570 kg/m^3 (bottom row). For the top row, the innermost contour line has a maximum value of 700 kJ/m^2 and the outermost has a minimum value of 100 kJ/m^2. For the bottom row, the maximum and minimum values are 90 kJ/m^2 and 10 kJ/m^2 respectively.

116
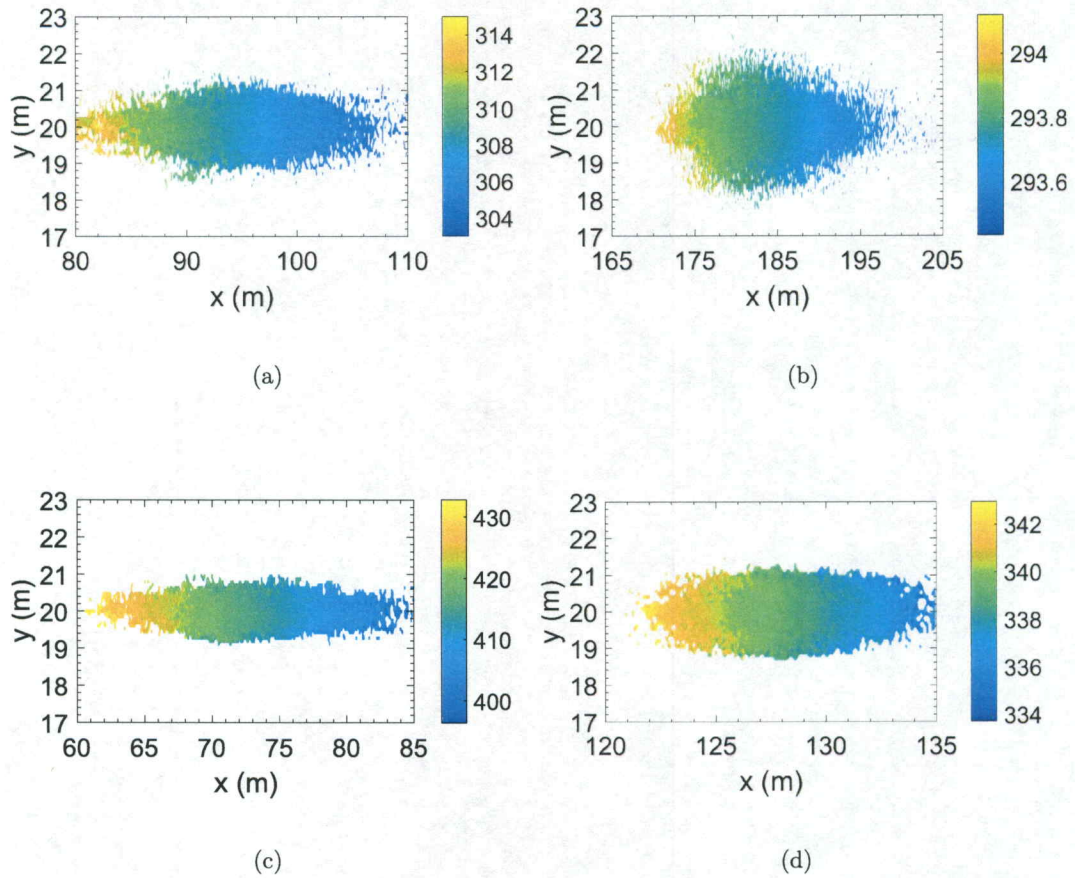
Figure 5.17: Average temperature of the ground deposited firebrands for release height = 20 m (left column) and 40 m (right column) for ρ_p = 230 kg/m^3 (top row) and 570 kg/m^3 (bottom row).

5.4 Chapter Summary

The effects of burning on cylindrical firebrands released in a TBL is discussed in this chapter. The firebrand burning model was based on the thermally thin assumption where firebrands were assumed to burn owing to the pyrolysis and char oxidation processes. Firebrands also exchanged heat with the surroundings by con-

117

vection and radiation mechanisms. The firebrand burning model, devoid of the effects of the ambient turbulent flow, was validated against the experiments of Muraszew [73] for different species of firebrands and wind conditions. It was found that for all the species, the computed fractional loss was reasonably close to that of the experimental measurements. Specifically, for the Ponderosa Pine species, the computed data was found to lie within 20 % of the experimental measurements.

Next, the effects of burning for the case of firebrands released in a TBL was investigated. Here, the trajectories of firebrands and their ground deposition pattern was studied for firebrand densities of 570 and 230 kg/m^3. Statistical analysis was carried out to determine the thermal and dynamical behavior of the flying firebrands released from heights of 20 and 40 m. The burning firebrands underwent reduction in mass and travelled for a longer distance (approximately 10 m ahead) in the streamwise direction as compared to the non-burning firebrands. It was also noted that, similar to the non-burning case, in the streamwise direction, the burning firebrands rapidly attained the streamwise velocity of the background air in a few seconds. For both the release heights, the firebrands with a lower initial density of 230 kg/m^3 were found to cool rapidly and reach ambient temperatures at the time of deposition. Due to rapid cooling, these firebrands also underwent a lower reduction in density during flight as compared to the firebrands with an initial density of 570 kg/m^3. The temperature of the firebrand was found to be mainly influenced by the processes of convective and radiative modes of cooling. Since the process of convection is largely a function of the relative velocity of the firebrand, the firebrand cooled at a much higher rate at early times due to high relative velocity. Compared to the convective heat loss

component, the radiative heat loss component was an order of magnitude lesser for all the cases. Since the firebrands with an initial density of 230 kg/m^3 cooled rapidly, the convective and the radiative heat loss components were near zero at the time of deposition. To understand the role of the background air turbulence on the dynamical and thermal behavior of firebrands, second order statistics were also analyzed. It was found that the trends of dispersion and diffusion of firebrands were similar to the cases of non-burning firebrands. Here, as time progressed, the firebrands encountered more turbulent regions and hence the variances and covariances of position and velocity increased. Furthermore, to gain an insight into the areas prone to the occurrence of spot fires, the ground deposition pattern of the landed firebrands was also studied. Here, the mass and energy per unit area of the landed firebrands was quantified and the average temperature of the landed firebrands was predicted. It was observed that the firebrands with an initial density of 570 kg/m^3 possessed higher energy by an order of magnitude greater than the firebrands with an initial density of 230 kg/m^3. This was observed because, the firebrands with an initial density of 570 kg/m^3 retained more energy (with average temperatures of 450 K) at the time of deposition. This behavior indicated a greater chance of occurrence of spot fires with higher density firebrands as they are less likely to cool and reach ambient temperatures at the time of deposition.

CHAPTER 6

CONCLUSIONS

6.0.1 Summary and Conclusions

In the current work, to better understand the mechanism of spotting phenomena, computational investigations were performed on live fuel ignitions and the propagation of firebrands in a turbulent boundary layer. First, the simulations on live fuel ignitions were performed using WFDS to improve the understanding of the ignitability condition of recipient fuels as pertinent to the landing stage in the spotting mechanism. These simulations were mainly guided by the experiments of McAllister et al. [65]. The experiments of McAllister et al. [65] comprised of burning live Douglas-fir needles in the Forced Ignition and Flame Spread Test Apparatus. To replicate the experimental work, simulations were performed to study the ignition characteristics of live Douglas-fir needles. A particle-based approach was used to model the burning of the Douglas-fir needles wherein the particles were assumed thermally thin. The effects of two distinct states of fuel moisture, viz., bound and free state was included in the Arrhenius-type FMC evaporation model. The predicted ignition time was found to lie well within the uncertainty of the experimental data. For all FMC, by including the effects of both bound and free water in the moisture evaporation model,

better prediction in the mass loss rates was obtained as compared the cases which included the effects of free water only. In consistent with experimental observations, the evaporation of moisture was observed at elevated temperatures ($> 100°C$) well after ignition of the fuel sample. For instance, free water was found to evaporate at temperatures close to boiling point of water whereas, bound water evaporated at temperatures close to $200°C$. For all FMC, significant amount of bound water was present at the time of ignition.

Next, the dispersion and deposition of firebrands in a turbulent boundary layer was investigated for the intermediate spotting range. The firebrands are mainly carried by the turbulent wind into regions devoid of any fire activity for the intermediate spotting range. To study the dynamical and thermal behavior of firebrands, a Lagrangian particle tracking module which solves for the three dimensional translation, rotation and burning of cylindrical firebrands was included within the framework of WFDS. Since the air turbulence plays an important role in dispersing the firebrands and influencing their landing locations, the dispersion and deposition of firebrands was studied in a turbulent boundary layer. The recycling technique of Lund et al. [54], as described in detail in Chapter 2 was used to generate the turbulent boundary layer. The statistics of the turbulent boundary layer was also validated against data available in literature. Once the turbulent boundary layer reached a statistically stationary state, firebrands were released continuously from a given point. Several simulations were performed by varying the initial density and release height of the firebrands. Furthermore, two distinct set of simulations were performed by considering cases with burning and non-burning firebrands. The current work was limited

121

to cylindrical firebrands, as these were observed to be commonly occurring [56, 57]. The physical properties of the firebrands were obtained from a previous experimental work [56]. The motion of the firebrands were tracked from the time they were released to the time of deposition. It was observed that, although the firebrands were released with zero initial velocities, regardless of their initial density and release height, they rapidly accelerated and attained free stream velocities in a short time. The lighter firebrands with a density of 70 kg/m^3 released from a higher elevation were found to travel the longest distance in the streamwise direction. The dispersion and diffusivity of firebrands was also studied to analyze the extent of spatial distribution of the firebrands. For all density cases, firebrands released outside the turbulent boundary layer were observed to have zero dispersion and diffusivity as the turbulent fluctuations were lacking. Whereas firebrands released within the boundary layer, from a height of 20 m, showed significant dispersion and diffusivity at early times due to the inherent turbulence in the flow field. For all the cases, the pattern of the ground deposited firebrands closely resembled an ellipse, exhibiting symmetry in the span-wise direction. Normalized statistics pertaining to the co-ordinates of the ground deposited firebrands was also analyzed. The streamwise variance of the deposited firebrands was found to be substantially large as compared to the spanwise variance. The calculated skewness and kurtosis was found to be higher in the cases of firebrands released from the height of 40 m.

Next, the effects of thermal degradation was also accounted with the firebrand dynamical model and statistical analysis was carried to study the motion of burning firebrands released in a turbulent boundary a layer. Here, the thermally thin assump-

tion was used to model the burning behavior of firebrands. Firebrands were assumed to thermally degrade and lose mass due to pyrolysis and char oxidation processes. The firebrands also exchanged heat with the ambient by convection and radiation mechanism. The thermal degradation model was first validated with a previous experimental work [73] for various firebrand species. The simulated fractional loss was found to be reasonably close to that of the experiments. For the Ponderosa Pine species, the simulated data was found to lie within 20 % of the experimental measurements. Few of the simulated data pertaining to the Englemann Spruce and Western Larch species are observed to deviate significantly from the experimental data. The discrepancies between the experimental and numerical results are attributed to experimental uncertainties and the non-availability of precise thermokinetic parameters for these species. After validation, the firebrand dynamics and burning behavior was studied for the case of firebrands released in a turbulent boundary layer. Firebrands with densities of 570 and 230 kg/m^3 were released from distinct points located within and above the boundary layer. It was observed that, regardless of the release heights, the firebrands with higher density cooled less rapidly and underwent a greater reduction in mass at the time of deposition. Whereas the lower density firebrands cooled rapidly and attained near ambient temperatures at the time of deposition. Since the firebrands are in motion, it was observed that the firebrands cooled mainly due to convection. The radiative heat loss component was an order of magnitude lesser than the convective heat loss component. The ground deposition pattern of the landed firebrands was also studied via kernel density estimation. While the deposition pattern of burning firebrands was similar to that observed in the case of non-burning firebrands, the

123

mass and energy per unit area of the ground deposited firebrands was quantified. The higher density firebrands were found to deposit with a mass per unit area equal to 1.5 kg/m^2 with an associated energy per unit area equal to 700 kJ/m^2, indicating the possibility of creation of spot fires in these regions. The average temperature of the deposited firebrands was also predicted and it was observed that firebrands with a density of 570 kg/m^3, showed a maximum variation, close to 30 K in the streamwise direction.

APPENDICES

APPENDIX A

TURBULENT INFLOW BOUNDARY CONDITION

A.1 Recycling Method

In the current section, the methodology used to specify the inflow conditions to generate the turbulent boundary layer used in Chapter 4 and Chapter 5 is described in detail. Often, the generation of a turbulent boundary layer requires a lengthy developmental section, starting from a laminar inflow and transitioning into a turbulent boundary layer at downstream locations. Including the developmental section is computationally expensive requiring additional computational resources and time. To reduce the dependency on such a developmental section and generate a turbulent boundary layer at the inlet, the recycling technique based on the work of Lund et al. [54] is used in the current work. The overall approach of the recycling method proposed by Lund et al. [54] is to estimate the instantaneous velocity at the inlet boundary based on the solution at a downstream location. Specifically, the instantaneous velocity field from a plane close to the exit of the domain (also referred as a recycling plane) is rescaled and reintroduced as an inlet boundary condition. The schematic of the computational domain showing locations of the inlet and the recycling plane are illustrated in Figure A.1. Here, the velocities at the recycling plane

126

are first decomposed into a mean and fluctuating part. Appropriate scaling laws are applied to each component and then recycled at the inlet. In the rest of the section, details pertaining to the recycling methodology is provided.

According to this method, the mean velocity field at the inlet of the domain is first initialized using the Spalding law. The Spalding law, as expressed below, satisfies the canonical turbulent boundary layer profile and is a single formula, which correlates the dimensionless velocity to the dimensionless wall normal distance, spanning the entire turbulent boundary layer height:

$$z^+ = u^+ + 0.1108 \left[e^{0.4u^+} - 1 - 0.4u^+ - \frac{(0.4u^+)^2}{2!} - \frac{(0.4u^+)^3}{3!} - \frac{(0.4u^+)^4}{4!} \right], \quad \text{(A.1)}$$

where,

$$z^+ = zu_\tau/\nu \quad \text{(A.2)}$$

$$u^+ = \bar{u}/u_\tau. \quad \text{(A.3)}$$

In the above equations, u_τ is the friction velocity calculated in terms of the wall shear stress τ_w as, $u_\tau = \tau_w/\rho$ and $\bar{u}$ is the velocity component averaged over time and space in the spanwise direction. To specify the inlet velocity u, u^+ is evaluated in terms of the wall normal component, z^+. Hence, to determine u as a function of z, a look-up table is first created to store values of z^+ as a function of u^+ using Equation A.1. Then, for a given z, corresponding to the grid location in the wall normal direction, the non-dimensional z^+ is determined using Equation A.2. From

the look-up table created using the Spalding law, the corresponding u^+ and hence u are evaluated. It is noted that a linear interpolation is performed if necessary (to evaluate u) when the precise value of z^+ is not found in the look-up table.

At the inlet, along with the Spalding law, random fluctuations with 10% turbulent intensity are also superimposed. Here, the synthetic eddy method [68], which is a built in feature in WFDS, is used to introduce the random fluctuations. Such a flow develops to yield a realistic turbulent boundary layer at downstream locations in the domain. Once a statistically stationary state is attained, a recycling plane is chosen at a location 80% downstream of the domain (shown in Figure A.1) to rescale and reintroduce velocity components at the inlet.

(a)

Figure A.1: Schematic diagram of the inlet boundary condition calculated via recycling technique

At the recycling plane, the streamwise velocity component in the inner and outer layer of the boundary layer are decomposed into a mean, $\bar{u}_i$ and its fluctuating part,

u_i''. Here, the mean velocities are averaged over both, time and space in the spanwise direction. Since the mean velocity profile satisfies scale similarity within the boundary layer, a scaling factor based on the friction velocity is used to rescale the mean and fluctuating components. To apply the recycling procedure, the turbulent boundary layer is furthermore divided into inner and outer regions. In the inner region where viscous effects are predominant, the law of the wall is used to relate the velocity components at the recycling plane to that at the inlet plane. Accordingly in the inner region, the law of the wall is given as:

$$u^+ = z^+.$$ (A.4)

Applying the above relation at both the inlet plane and recycling plane, we have,

$$u_{\text{inlet}}^+ = z_{\text{inlet}}^+$$ (A.5)

$$u_{\text{recyc}}^+ = z_{\text{recyc}}^+.$$ (A.6)

For a given z^+, at the inlet and recycling planes, i.e. for $z_{\text{inlet}}^+ = z_{\text{recyc}}^+$, we have $u_{\text{inlet}}^+ (z^+) = u_{\text{recyc}}^+ (z^+)$. Furthermore, using the relation given in eq. (A.3), the dimensional form of the equation at a given z^+ is expressed as:

$$\frac{\bar{u}_{\text{inlet}}^{\text{inner}} (z^+)}{(u_\tau)_{\text{inlet}}} = \frac{\bar{u}_{\text{recyc}}^{\text{inner}} (z^+)}{(u_\tau)_{\text{recyc}}}$$ (A.7)

Rearranging the above equation, we have:

$$\bar{u}_{\text{inlet}}^{\text{inner}}\left(z^+\right) = \frac{\left(u_\tau\right)_{\text{inlet}}}{\left(u_\tau\right)_{\text{recyc}}}\bar{u}_{\text{recyc}}^{\text{inner}}\left(z^+\right) \tag{A.8}$$

and

$$\bar{u}_{\text{inlet}}^{\text{inner}}\left(z^+\right) = \gamma\bar{u}_{\text{recyc}}^{\text{inner}}\left(z^+\right). \tag{A.9}$$

Here, γ is the scaling factor defined as the ratio of the friction velocity measured at the recycle plane and the friction velocity measured at the inlet plane. Similarly, away from the wall, in the outer region, the law of the wake [17] is used. Accordingly, the law of the wake is given as:

$$U_\infty - \bar{u}^{\text{outer}}\left(\eta\right) = u_\tau f_1\left(\eta\right) \tag{A.10}$$

Here, η is the normalized coordinate in the outer region given as $\eta = z/\delta$ and U_∞ is the freestream velocity. Since, the law of the wake is applied throughout the outer region of the turbulent boundary layer which encompasses the buffer, logarithmic and the wake region, the functionality $f_1\left(\eta\right)$ is not explicitly known in Equation A.10. Applying the law of the wake at the inlet and recycle planes, the mean velocity component at the inlet plane can be expressed in terms of that at the recycle plane for a given η as:

$$\bar{u}_{\text{inlet}}^{\text{outer}}\left(\eta\right) = \gamma\bar{u}_{\text{recyc}}^{\text{outer}}\left(\eta\right) + (1 - \gamma)U_\infty \tag{A.11}$$

Also, in the inner and outer regions, the mean vertical velocity component is assumed to scale respectively as:

$$\bar{v}^{\text{inner}} = U_\infty f_2 \left(z^+\right) \tag{A.12}$$

$$\bar{v}^{\text{outer}} = U_\infty f_3 \left(z^+\right). \tag{A.13}$$

Here, the functions f_2, f_3 and the functions f_4, f_5 which appear in the next paragraph are not known explicitly. Similar to the approach described above, on applying the scaling laws at both the planes, we have,

$$\bar{v}^{\text{inner}}_{\text{inlet}} \left(z^+\right) = \bar{v}^{\text{inner}}_{\text{recyc}} \left(z^+\right) \tag{A.14}$$

and

$$\bar{v}^{\text{outer}}_{\text{inlet}} \left(\eta\right) = \bar{v}^{\text{outer}}_{\text{recyc}} \left(\eta\right). \tag{A.15}$$

Since the mean of the spanwise velocity $\bar{v}$ is zero, no scaling law is applied. Furthermore, the scaling for the fluctuating components of velocity for the inner and outer region is shown below:

$$(u_i')^{\text{inner}} \left(x, y, z^+, t\right) = u_\tau f_4(x, y, z^+, t) \tag{A.16}$$

131

and

$$(u_i')^{\text{outer}}(x, y, \eta, t) = u_\tau f_5(x, y, \eta, t). \tag{A.17}$$

Applying these laws at the inlet and recycle plane and following the methodology described above, the vertical velocity components at the inlet for both inner and outer regions are expressed in terms of that at the recycle plane as:

$$u_{i,\text{inlet}}'^{,\text{inner}}\left(y, z^+, t\right) = \gamma u_{i,\text{recyc}}'^{,\text{inner}}\left(y, z^+, t\right) \quad \text{and}$$

$$u_{i,\text{inlet}}'^{,\text{inner}}\left(y, \eta, t\right) = \gamma u_{i,\text{recyc}}'^{,\text{inner}}\left(y, \eta, t\right). \tag{A.18}$$

Using, Equations A.9, A.11, A.14 and A.18, a composite profile for the instantaneous velocity at the inlet, encompassing both the inner and outer regions is expressed as:

$$u_{i,\text{inlet}}\left(y, z, t\right) = \left[\bar{u}_{i,\text{inlet}}(z) + u_{i,\text{inlet}}''(y, z, t)\right]^{\text{inner}}\left[1 - W(\eta_{\text{inlet}})\right] +$$

$$\left[\bar{u}_{i,\text{inlet}}(z) + u_{i,\text{inlet}}''(y, z, t)\right]^{\text{outer}}\left[1 - W(\eta_{\text{inlet}})\right], \tag{A.19}$$

where

$$W(\eta) = 0.5 \left[\frac{1 + \tanh\left[\frac{\alpha(\eta - b)}{(1 - 2b)\eta + b}\right]}{\tanh(\alpha)}\right] \tag{A.20}$$

is the weighting function which takes into account the transition from inner to outer layer. The parameters α and b are set to 4 and 0.2, respectively [54]. These values are chosen such that the weighting function is zero at $\eta = 0$ and unity at $\eta = b$. Hence,

at the inner region of the boundary layer, the term $[1 - W(\eta_{\text{inlet}})]$ has more weight and at the outer region of the boundary layer, $W(\eta_{\text{inlet}})$ has more weight.

A.2 Additional figures

In this section, additional figures pertaining to the turbulent boundary layer ($\text{Re}_\theta = 10^6$) in which the firebrands are released are shown. Details concerning the properties of the turbulent boundary layer are discussed in Chapter 4. Here, the three dimensional representation of the isosurface of the Q-criterion, and the vorticity magnitude, Figure A.2 of the turbulent boundary layer are shown on a slice plane at $y=20$ m after the boundary layer attains a statistically stationary state.

Also illustrated in this section are the scatter plots (Figure A.3 and Figure A.4) pertaining to the dispersion of firebrands for the non-burning case with firebrand density of 230 kg/m^3 released from elevations of 20 and 40 m. These plots show the scatter of all firebrands considered in the simulations from the time of release to deposition. While the two-dimensional probability density function of the ground deposited firebrands has been discussed in detail in Chapter 4, for the sake of completeness, the associated three-dimensional representation is also illustrated in Figure A.5.
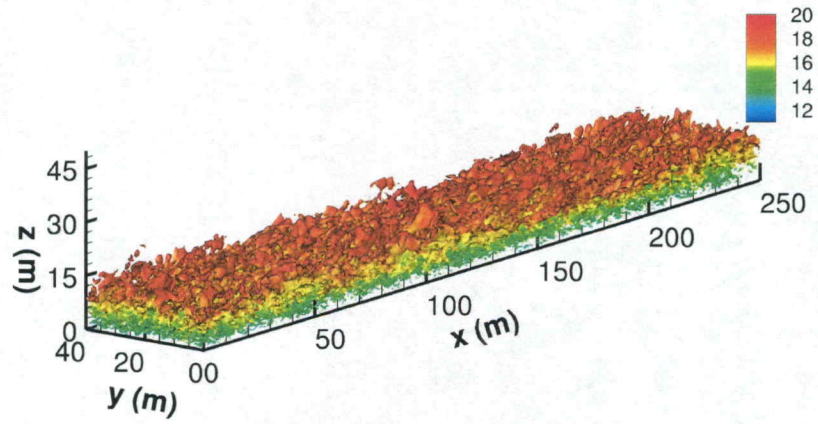
(a)
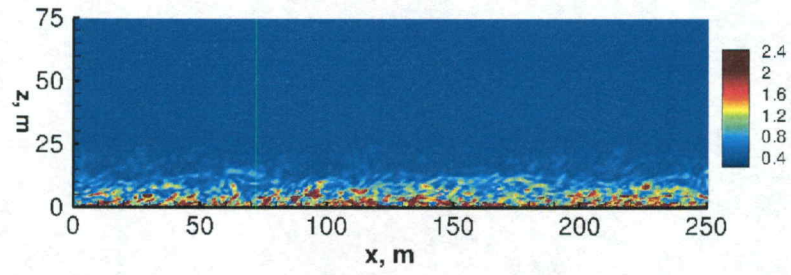
(b)

Figure A.2: (a) Isosurface of Q-criterion and (b) slice plane showing the vorticity magnitude at y=20 m.
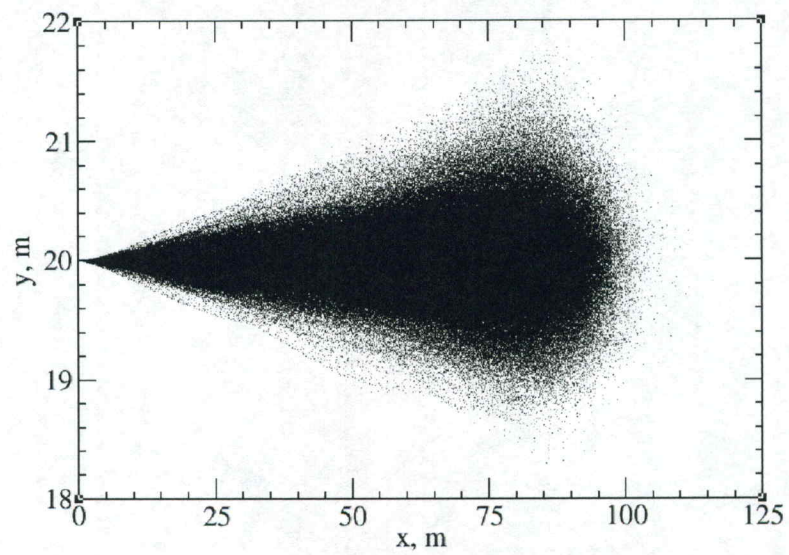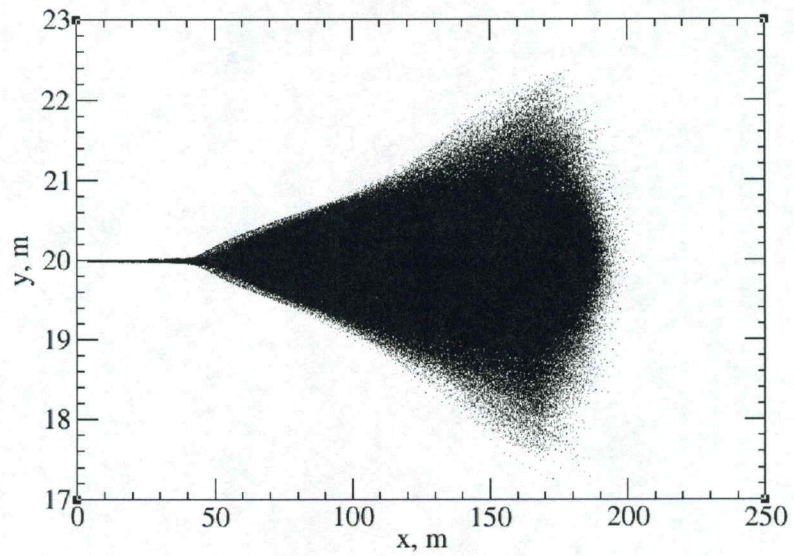
Figure A.3: Scatter plot of firebrand paths in the xy plane for firebrands of density 230 kg/m³ released from height (a) 20 m and (b) 40 m.

135
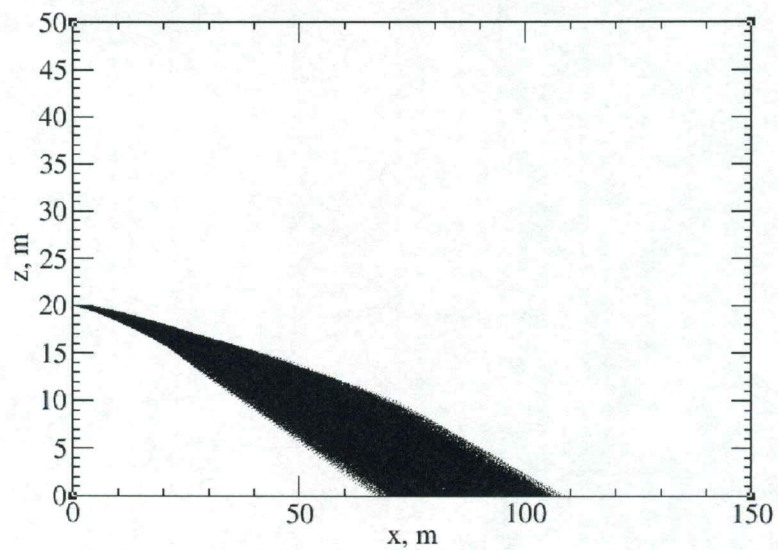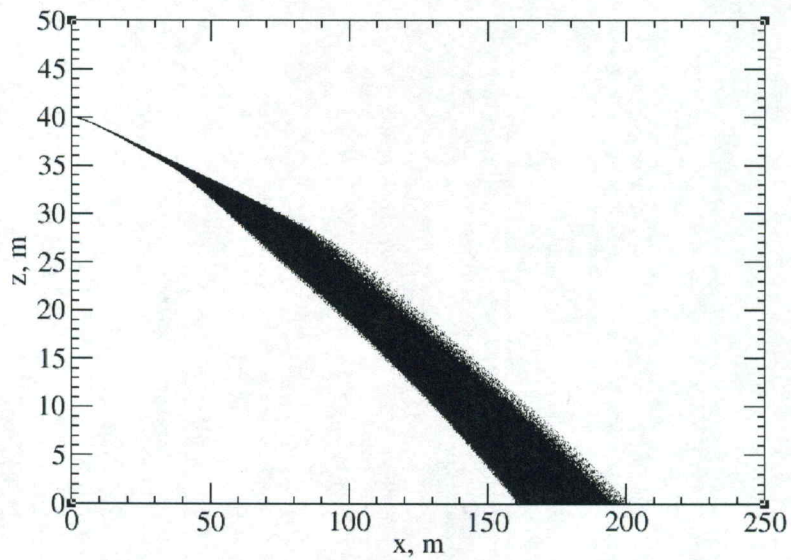
Figure A.4: Scatter plot of firebrand paths in the xz plane for firebrands of density 230 kg/m^3 released from height (a) 20 m and (b) 40 m.
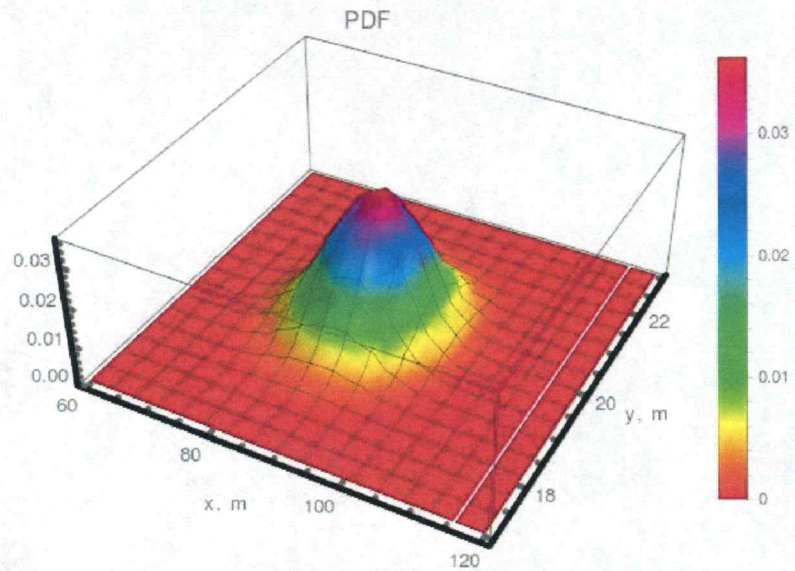
(a)
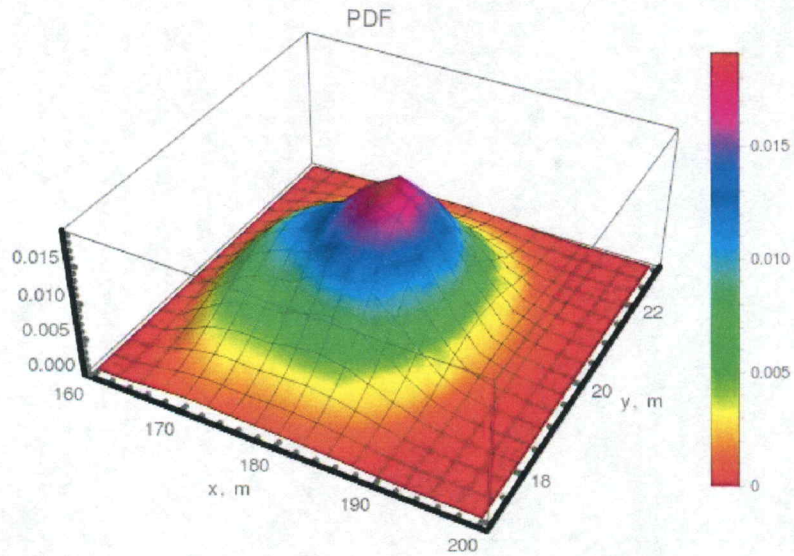
(b)

Figure A.5: Three dimensional representation of the probability density function of deposited firebrands of density 230 kg/m^3 released from height (a) 20 m and (b) 40 m.

REFERENCES

[1] FA Albini. Transport of firebrands by line thermals. *Combustion Science and Technology*, 32(5-6):277–288, 1983.

[2] Frank A Albini. Spot fire distance from burning trees. General Technical Report INT-56, Intermountain Forest and Range Experiment Station, Missoula,MT, 1979.

[3] Frank A Albini. *Thermochemical properties of flame gases from fine wildland fuels*, volume 243. Intermountain Forest and Range Experiment Station, Forest Service, U.S. Department of Agriculture, 1980.

[4] Niels Andela, DC Morton, Louis Giglio, Yang Chen, GR van der Werf, PS Kasibhatla, RS DeFries, GJ Collatz, S Hantson, Silvia Kloster, et al. A human-driven decline in global burned area. *Science*, 356(6345):1356–1362, 2017.

[5] Ralph A Anthenien, D Tse Stephen, and A Carlos Fernandez-Pello. On the trajectories of embers initially elevated or lofted by small scale ground fire plumes in high winds. *Fire Safety Journal*, 41(5):349–363, 2006.

[6] Vincenzo Armenio and Virgilio Fiorotto. The importance of the forces acting on particles in turbulent flows. *Physics of Fluids*, 13(8):2437–2440, 2001.

[7] Arvind Atreya and Mahmood Abu-Zaid. Effect of environmental variables on piloted ignition. *Fire Safety Science*, 3:177–186, 1991.

[8] Vytenis Babrauskas. *Ignition handbook*. Fire Science Publishers, Issaquah, WA, 2003.

[9] Julien Berthaut-Gerentes and Didier Delaunay. LES: Unsteady atmospheric turbulent layer inlet. a precursor method application and its quality check. *Computation*, 3(2):262–273, 2015.

[10] Winfred Harold Blackmarr and William B Flanner. Seasonal and diurnal variation in moisture content of six species of pocosin shrubs. Research Paper SE-33, Southeastern Forest Experiment Station, Forest Service, U.S. Department of Agriculture, 1968.

[11] Claus W Böning. Characteristics of particle dispersion in the north atlantic: an alternative interpretation of sofar float results. *Deep Sea Research Part A. Oceanographic Research Papers*, 35(8):1379–1385, 1988.

[12] David MJS Bowman, Jennifer K Balch, Paulo Artaxo, William J Bond, Jean M Carlson, Mark A Cochrane, Carla M DAntonio, Ruth S DeFries, John C Doyle, Sandy P Harrison, et al. Fire in the earth system. *science*, 324(5926):481–484, 2009.

[13] Kenneth M Bryden, Kenneth W Ragland, and Christopher J Rutland. Modeling thermally thick pyrolysis of wood. *Biomass and Bioenergy*, 22(1):41–53, 2002.

[14] National Interagency Fire Center. Fire Statistics: 2017. `https://www.nifc.gov/fireInfo/fireInfo_statistics.html`, 2018. [Online; accessed 04-04-2018].

[15] Wai-Chun R Chan, Marcia Kelbon, and Barbara B Krieger. Modelling and experimental verification of physical and chemical processes during pyrolysis of a large biomass particle. *Fuel*, 64(11):1505–1513, 1985.

[16] SW Churchill and M Bernstein. A correlating equation for forced convection from gases and liquids to a circular cylinder in crossflow. *Journal of Heat Transfer*, 99(2):300–306, 1977.

[17] Donald Coles. The law of the wake in the turbulent boundary layer. *Journal of Fluid Mechanics*, 1(2):191–226, 1956.

[18] Clayton T Crowe, John D Schwarzkopf, Martin Sommerfeld, and Yutaka Tsuji. *Multiphase flows with droplets and particles*. CRC press, 2011.

[19] MG Cruz, AL Sullivan, JS Gould, NC Sims, AJ Bannister, JJ Hollis, and RJ Hurley. Anatomy of a catastrophic wildfire: the black saturday kilmore east fire in victoria, australia. *Forest Ecology and Management*, 284:269–285, 2012.

[20] GT Csanady. Turbulent diffusion of heavy particles in the atmosphere. *Journal of the Atmospheric Sciences*, 20(3):201–208, 1963.

[21] Ambarish Dahale, Selina Ferguson, Babak Shotorban, and Shankar Mahalingam. Effects of distribution of bulk density and moisture content on shrub fires. *International Journal of Wildland Fire*, 22 (5):625–641, 2013.

[22] David B De Graaff and John K Eaton. Reynolds-number scaling of the flat-plate turbulent boundary layer. *Journal of Fluid Mechanics*, 422:319–346, 2000.

[23] James W Deardorff. Stratocumulus-capped mixed layers derived from a three-dimensional model. *Boundary-Layer Meteorology*, 18(4):495–527, 1980.

[24] AP Dimitrakopoulos and Kyriakos K Papaioannou. Flammability assessment of mediterranean forest fuels. *Fire Technology*, 37(2):143–152, 2001.

[25] J Dreisbach and K Hill. Verification & validation of selected fire models for nuclear power plant applications-volume 7: Fire dynamics simulator. *NUREG-1824*, 2007.

[26] S. C. Ferguson, A. Dahale, B. Shotorban, S. Mahalingam, and D. R. Weise. The role of moisture on combustion of pyrolysis gases in wildland fires. *Combustion Science and Technology*, 185:435–453, 2013.

[27] A Carlos Fernandez-Pello. Wildland fire spot ignition by sparks and firebrands. *Fire Safety Journal*, 91:2–10, 2017.

[28] Mark A Finney, Jack D Cohen, Sara S McAllister, and W Matt Jolly. On the need for a theory of wildland fire spread. *International Journal of Wildland Fire*, 22(1):25–36, 2013.

[29] Thomas H Fletcher, Brent M Pickett, Steven G Smith, Gregory S Spittle, Megan M Woodhouse, Elizabeth Haake, and David R Weise. Effects of moisture on ignition behavior of moist california chaparral and utah leaves. *Combustion Science and Technology*, 179(6):1183–1203, 2007.

[30] Wallace L Fons. Influence of forest cover on wind velocity. *Journal of Forestry*, 38(6):481–486, 1940.

[31] GI Fryer and EA Johnson. Reconstructing fire behaviour and effects in a sub-alpine forest. *Journal of Applied Ecology*, pages 1063–1072, 1988.

[32] Jonathan R Gallacher. *The Influence of Season, Heating Mode and Slope Angle on Wildland Fire Behavior*. PhD thesis, Brigham Young University-Provo, 2016.

[33] Herbert Goldstein. *Classical mechanics*. Pearson Education India, 2011.

[34] A. M. Grishin. Mathematical Modelling of Forest Fires and New Methods of Fighting Them. Publishing House of Tomsk State University, Tomsk, Russia, 1997.

[35] SR Hanna, S Tehranian, B Carissimo, RW Macdonald, and R Lohner. Comparisons of model simulations with observations of mean flow and turbulence within simple obstacle arrays. *Atmospheric Environment*, 36(32):5067–5079, 2002.

[36] Keisuke Himoto and Takeyoshi Tanaka. Transport of disk-shaped firebrands in a turbulent boundary layer. *Fire Safety Science*, 8:433–444, 2005.

[37] Sighard F Hoerner. *Fluid-dynamic drag: practical information on aerodynamic drag and hydrodynamic resistance*. Hoerner Fluid Dynamics, 1965.

[38] Hong Huang, Ryozo Ooka, Shinsuke Kato, and Yoshihiko Hayashi. A numerical study of firebrands scattering in urban fire based on cfd and firebrands aerodynamics measurements. *Journal of Fire Sciences*, 25(4):355–378, 2007.

[39] M Inoue and DI Pullin. Large-eddy simulation of the zero-pressure-gradient turbulent boundary layer up to $Re_\theta = O(10^{12})$. *Journal of Fluid Mechanics*, 686:507–533, 2011.

[40] Donald A Jameson. *Diurnal and seasonal fluctuations in moisture content of pinyon and juniper*, volume 67. Rocky Mountain Forest and Range Experiment Station, Forest Service, U.S. Department of Agriculture, 1966.

[41] Marc Janssens. *Fundamental thermophysical characteristics of wood and their role in enclosure fire growth*. PhD thesis, Ghent University, 1991.

[42] W Matt Jolly, Russell A Parsons, Ann M Hadlow, Greg M Cohn, Sara S McAllister, John B Popp, Robert M Hubbard, and Jose F Negron. Relationships between moisture, chemistry, and ignition of pinus contorta needles during the early stages of mountain pine beetle attack. *Forest Ecology and Management*, 269:52–59, 2012.

[43] W. Matt Jolly, Ann M. Hadlow, and Kathleen Huguet. De-coupling seasonal changes in water content and dry matter to predict live conifer foliar moisture content. *International Journal of Wildland Fire*, 23(4):480, 2014.

[44] D Kaftori, G Hetsroni, and S Banerjee. Particle behavior in the turbulent boundary layer. ii. velocity and distribution profiles. *Physics of Fluids*, 7(5):1107–1121, 1995.

[45] Jagadish Chandran Kaimal and John J Finnigan. *Atmospheric boundary layer flows: their structure and measurement*. Oxford University Press, 1994.

[46] GI Kelbaliyev. Drag coefficients of variously shaped solid particles, drops, and bubbles. *Theoretical Foundations of Chemical Engineering*, 45(3):248–266, 2011.

[47] Joseph Buckner Killebrew. *The Grasses of Tennessee: Including Cereals and Forage Plants*. American Company, 1878.

[48] Eunmo Koo, Patrick J Pagni, David R Weise, and John P Woycheese. Firebrands and spotting ignition in large-scale fires. *International Journal of Wildland Fire*, 19(7):818–843, 2010.

[49] Eunmo Koo, Rodman R Linn, Patrick J Pagni, and Carleton B Edminster. Modelling firebrand transport in wildfires using HIGRAD/FIRETEC. *International Journal of Wildland Fire*, 21(4):396–417, 2012.

[50] Theodore T Kozlowski and J Johanna Clausen. Changes in moisture contents and dry weights of buds and leaves of forest trees. *Botanical Gazette*, pages 20–26, 1965.

[51] Gary J Kunkel and Ivan Marusic. Study of the near-wall-turbulent region of the high-reynolds-number boundary layer using an atmospheric flow. *Journal of Fluid Mechanics*, 548:375–402, 2006.

[52] CHA Little. Seasonal changes in carbohydrate and moisture content in needles of balsam fir (*abies balsamea*). *Canadian Journal of Botany*, 48(11):2021–2028, 1970.

[53] R Harry Luke, Alan Grant McArthur, et al. *Bushfires in Australia*. Australian Government Publishing Service for CSIRO., 1978.

[54] Thomas S Lund, Xiaohua Wu, and Kyle D Squires. Generation of turbulent inflow data for spatially-developing boundary layer simulations. *Journal of Computational Physics*, 140(2):233–258, 1998.

[55] S Mahalingam, BJ Cantwell, and JH Ferziger. Full numerical simulation of coflowing, axisymmetric jet diffusion flames. *Physics of Fluids A: Fluid Dynamics*, 2(5):720–728, 1990.

[56] Samuel L Manzello, Alexander Maranghides, and William E Mell. Firebrand generation from burning vegetation. *International Journal of Wildland Fire*, 16 (4):458–462, 2007.

[57] Samuel L Manzello, Thomas G Cleary, John R Shields, Alexander Maranghides, William Mell, and Jiann C Yang. Experimental investigation of firebrands: generation and ignition of fuel beds. *Fire Safety Journal*, 43(3):226–233, 2008.

[58] Samuel L Manzello, Yoshihiko Hayashi, Takefumi Yoneki, and Yu Yamamoto. Firebrand attack on ceramic tile roofing assemblies. In *Proceedings, 2009 Fire and Materials Conference. London: Interscience Communications Limited*, 2009.

[59] Samuel L Manzello, Seul-Hyun Park, Sayaka Suzuki, John R Shields, and Yoshihiko Hayashi. Experimental investigation of structure vulnerabilities to firebrand showers. *Fire Safety Journal*, 46(8):568–578, 2011.

[60] Alexander Maranghides and William Mell. A case study of a community affected by the Witch and Guejito wildland fires. *Fire technology*, 47(2):379–420, 2011.

[61] EK Marchildon, A Clamen, and WH Gauvin. Drag and oscillatory motion of freely falling cylindrical particles. *The Canadian Journal of Chemical Engineering*, 42(4):178–182, 1964.

[62] Kanti V Mardia. Measures of multivariate skewness and kurtosis with applications. *Biometrika*, 57(3):519–530, 1970.

[63] Kanti V Mardia. Applications of some measures of multivariate skewness and kurtosis in testing normality and robustness studies. *Sankhyā: The Indian Journal of Statistics, Series B*, pages 115–128, 1974.

[64] MR Maxey. The gravitational settling of aerosol particles in homogeneous turbulence and random flow fields. *Journal of Fluid Mechanics*, 174:441–465, 1987.

[65] S. McAllister, I. Grenfell, A. Hadlow, W.M. Jolly, M. Finney, and J. Cohen. Piloted ignition of live forest fuels. *Fire Safety Journal*, 51:133–142, 2012.

[66] Randall McDermott, Kevin McGrattan, and Simo Hostikka. Fire dynamics simulator (version 5) technical reference guide. *NIST Special Publication*, 1018: 5, 2008.

[67] Kevin McGrattan, Simo Hostikka, Randall McDermott, Jason Floyd, Craig Weinschenk, and Kristopher Overholt. Fire dynamics simulator technical reference guide volume 1: mathematical model. *NIST special publication*, 1018(1): 175, 2013.

[68] Kevin B McGrattan, Howard R Baum, Ronald G Rehm, Anthony Hamins, Glenn P Forney, JE Floyd, and S Hostikka. *Fire dynamics simulator–Technical reference guide*. National Institute of Standards and Technology, Building and Fire Research Laboratory, 2000.

[69] William Mell, Alexander Maranghides, Randall McDermott, and Samuel L. Manzello. Numerical simulation and experiments of burning douglas fir trees. *Combustion and Flame*, 156(10):2023–2041, 2009.

[70] B Moghtaderi and DF Fletcher. Flaming combustion characteristics of wood-based materials. *Fire Safety Science*, 3:209–220, 1988.

[71] D Morvan and JL Dupuy. Modeling the propagation of a wildfire through a mediterranean shrub using a multiphase formulation. *Combustion and flame*, 138(3):199–210, 2004.

[72] MFR Mulcahy. Kinetics of combustion of pulverized fuel: a review of theory and experiment. *Rev. Pure and Appl. Chem.*, 19:81–108, 1969.

[73] A Muraszew, WC Kuby, and JB Fedele. *Firebrand investigation*. Aerospace Corporation, 1975.

[74] Ralph M Nelson. *Water relations of forest fuels*. Academic Press: San Francisco, CA, USA, 2001.

[75] ABC news. Wildfires rage on untamed in Greece, Portugal and Corsica. `http://abcnews.go.com/amp/Travel/wireStory/french-summer-wildfires-ravage-2000-hectares-land-49190000`, 2017. [Online; accessed 04-04-2018].

[76] Derrick O Njobuenwu and Michael Fairweather. Simulation of inertial fibre orientation in turbulent flow. *Physics of Fluids*, 28(6):063307, 2016.

[77] California Department of Forestry and Fire Protection (http://calfire.ca.gov/fireprotection/downloads/redsheet/Fuels.pdf). Live fuels, 2004.

[78] Luis A Oliveira, António G Lopes, Bantwal R Baliga, Miguel Almeida, and Domingos X Viegas. Numerical prediction of size, mass, temperature and trajectory of cylindrical wind-driven firebrands. *International Journal of Wildland Fire*, 23(5):698–708, 2014.

[79] I. Orlanski. A simple boundary condition for unbounded hyperbolic flows. *Journal of Computational Physics*, 21(3):251–269, 1976.

[80] Kristopher J Overholt, Craig G Weinschenk, and Daniel Madrzykowski. *Simulation of a Fire in a Hillside Residential Structure-San Francisco, CA*. US Department of Commerce, National Institute of Standards and Technology, 2014.

[81] Patrick J Pagni. Causes of the 20 october 1991 oakland hills conflagration. *Fire Safety Journal*, 21(4):331–339, 1993.

[82] G Pellizzaro, P Duce, A Ventura, and P Zara. Seasonal variations of live moisture content and ignitability in shrubs of the mediterranean basin. *International Journal of Wildland Fire*, 16(5):633–641, 2007.

[83] José CF Pereira, José Pereira, André LA Leite, and Duarte Albuquerque. Calculation of spotting particles maximum distance in idealised forest fire scenarios. *Journal of Combustion*, 2015, 2015.

[84] Charles W Philpot. *Diurnal fluctuation in moisture content of ponderosa pine and whiteleaf manzanita leaves*. Research Note PSW-67, Pacific Southwest Forest and Range Experiment Station, Forest Service, U.S. Department of Agriculture, 1965.

[85] B. M. Pickett, C. Isackson, R. Wunder, T. H. Fletcher, B. W. Butler, and D. R. Weise. Experimental measurements during combustion of moist individual foliage samples. *International Journal of Wildland Fire*, 19:153–162, 2010.

[86] Stephen B Pope. Ten questions concerning the large-eddy simulation of turbulent flows. *New journal of Physics*, 6(1):35, 2004.

[87] B Porterie, JL Consalvi, A Kaiss, and JC Loraud. Predicting wildland fire behavior and emissions using a fine-scale physical model. *Numerical Heat Transfer, Part A: Applications*, 47(6):571–591, 2005.

[88] William H Press. *The art of scientific computing*. Cambridge University Press, 1992.

[89] Dallan R Prince. *Measurement and modeling of fire behavior in leaves and sparse shrubs*. PhD thesis, Brigham Young University-Provo, 2014.

[90] Dallan R Prince and Thomas H Fletcher. A combined experimental and theoretical study of the combustion of live vs. dead leaves. In *8th US National Combustion Meeting of the Combustion Institute, Park City, UT*, 2013.

[91] Man Mohan Rai and Parviz Moin. Direct numerical simulation of transition and turbulence in a spatially evolving boundary layer. *Journal of Computational Physics*, 109(2):169–192, 1993.

[92] Gisel Reyes, Sandra Brown, Jonathan Chapman, and Ariel E Lugo. Wood densities of tropical tree species. *Gen. Tech. Rep. SO-88. New Orleans, LA: U.S. Department of Agriculture, Forest Service, Southern Forest Experiment Station. 15 p.*, 88, 1992.

[93] CB Rogers and JK Eaton. The effect of small particles on fluid turbulence in a flat-plate, turbulent boundary layer in air. *Physics of Fluids A: Fluid Dynamics*, 3(5):928–937, 1991.

[94] R. J. Ross. Wood handbook. General Technical Report FPLGTR190, Forest Products Laboratory, United States Department of Agriculture Forest Service, 2010.

[95] R.C. Rothermel. A mathematical model for predicting fire spread in wildland fuels. Research Paper INT-115, U.S. Department of Agriculture, Intermountain Forest and Range Experiment Station, Ogden, UT, 1972.

[96] N Sardoy, JL Consalvi, A Kaiss, AC Fernandez-Pello, and B Porterie. Numerical study of ground-level distribution of firebrands generated by line fires. *Combustion and Flame*, 154(3):478–488, 2008.

[97] Nicolas Sardoy, Jean-Louis Consalvi, Bernard Porterie, and A Carlos Fernandez-Pello. Modeling transport and combustion of firebrands from burning trees. *Combustion and Flame*, 150(3):151–169, 2007.

[98] Babak Shotorban and Farzad Mashayek. Modeling subgrid-scale effects on particles by approximate deconvolution. *Physics of Fluids*, 17(8):081701, 2005.

[99] Babak Shotorban and Farzad Mashayek. A stochastic model for particle motion in large-eddy simulation. *Journal of Turbulence*, (7):N18, 2006.

[100] D. L. Simms and M. Law. The ignition of wet and dry wood by radiation. *Combustion and Flame*, 11(5):377–388, 1967.

[101] Steven G Smith. Effects of moisture on combustion characteristics of live california chaparral and utah foliage. Master's thesis, Brigham Young University-Provo, 2005.

[102] William H Snyder and JL Lumley. Some measurements of particle velocity autocorrelation functions in a turbulent flow. *Journal of Fluid Mechanics*, 48 (1):41–71, 1971.

[103] Philippe R Spalart. Direct simulation of a turbulent boundary layer up to $Re_\theta=$ 1410. *Journal of Fluid Mechanics*, 187:61–98, 1988.

[104] DB Spalding. A single formula for the law of the wall. *Journal of Applied Mechanics*, 28(3):455–458, 1961.

[105] D Tse Stephen and A Carlos Fernandez-Pello. On the flight paths of metal particles and embers generated by power lines in high windsa potential source of wildland fires. *Fire Safety Journal*, 30(4):333–356, 1998.

[106] Sayaka Suzuki and Samuel L Manzello. Characteristics of firebrands collected from actual urban fires. *Fire Technology*, pages 1–14.

[107] C Sánchez Tarifa, P Pérez del Notario, and F García Moreno. On the flight paths and lifetimes of burning particles of wood. In *Symposium (international) on combustion*, volume 10, pages 1021–1037. Elsevier, 1965.

[108] Geoffrey I Taylor. Diffusion by continuous movements. *Proceedings of the London Mathematical Society*, 2(1):196–212, 1922.

[109] William Thurston, Jeffrey D Kepert, Kevin J Tory, and Robert JB Fawcett. The contribution of turbulent plume dynamics to long-range spotting. *International Journal of Wildland Fire*, 26(4):317–330, 2017.

[110] Ali Tohidi and Nigel B Kaye. Stochastic modeling of firebrand shower scenarios. *Fire Safety Journal*, 91:91–102, 2017.

[111] Ali Tohidi and Nigel Berkeley Kaye. Comprehensive wind tunnel experiments of lofting and downwind transport of non-combusting rod-like model firebrands during firebrand shower scenarios. *Fire Safety Journal*, 90:95–111, 2017.

[112] CE Van Wagner. Seasonal variation in moisture content of eastern canadian tree foliage and the possible effect on crown fires. Forestry Branch Canada, 1967.

[113] Xiaoyun Wang, Charles Fleischmann, and Michael Spearpoint. Assessing the influence of fuel geometrical shape on fire dynamics simulator (fds) predictions for a large-scale heavy goods vehicle tunnel fire experiment. *Case Studies in Fire Safety*, 5:34–41, 2016.

[114] David R Weise, Robert H White, Frank C Beall, and Matt Etlinger. Use of the cone calorimeter to detect seasonal differences in selected combustion characteristics of ornamental vegetation. *International Journal of Wildland Fire*, 14(3):321–338, 2005.

[115] David R. Weise, XiangYang Zhou, Shankar Mahalingam, and Joey Chong. Marginal fire spread in live fuel beds-horizontal fuels. Fort Collins, CO: Forest Service Research Data Archive, 2015.

[116] H Werner and H Wengle. Large-eddy simulation of turbulent flow over and around a cube in a plate channel. In *Turbulent Shear Flows 8*, pages 155–168. Springer, 1993.

[117] RA Wilson and ML Brown. Variation in char density on laboratory fuels [free-burning wood fuels, pinus ponderosa, betula]. General Technical Report INT-236, Research Note INT-U.S. Department of Agriculture, Ogden, UT, 1977.

[118] Xiaohua Wu and Parviz Moin. Direct numerical simulation of turbulence in a nominally zero-pressure-gradient flat-plate boundary layer. *Journal of Fluid Mechanics*, 630:5–41, 2009.

[119] Gavriil Xanthopoulos and Ronald H Wakimoto. A time to ignition-temperature-moisture relationship for branches of three western conifers. *Canadian Journal of Forest Research*, 23(2):253–258, 1993.

[120] Haiping Yang, Rong Yan, Hanping Chen, Dong Ho Lee, and Chuguang Zheng. Characteristics of hemicellulose, cellulose and lignin pyrolysis. *Fuel*, 86(12-13): 1781–1788, 2007.

[121] BL Yashwanth, J Gallacher, B Shotorban, S Mahalingam, TH Fletcher, and DR Weise. Experimental and numerical investigation of the effect of heating modes and moisture content on pyrolysis and ignition of live fuels. In *Proceedings of the 9th US National Meeting, Central States Section of the Combustion Institute, Cincinnati, OH*, 2015.

[122] BL Yashwanth, B Shotorban, S Mahalingam, CW Lautenberger, and DR Weise. A numerical investigation of the influence of radiation and moisture content on pyrolysis and ignition of a leaf-like fuel element. *Combustion and Flame*, 163: 301–316, 2016.

[123] Chungen Yin, Lasse Rosendahl, Søren Knudsen Kær, and Henrik Sørensen. Modelling the motion of cylindrical particles in a nonuniform flow. *Chemical Engineering Science*, 58(15):3489–3498, 2003.

[124] Chungen Yin, Lasse Rosendahl, Søren Knudsen Kær, and Henrik Sørensen. Corrigendum to modelling the motion of cylindrical particles in a nonuniform flow[chem. eng. sci. 58 (2003) 3489–3498]. *Chemical Engineering Science*, 66 (1):117, 2011.